UNIVERSITA' DEGLI STUDI DI PADOVA
Department of Civil, Environmental and Architectural Engineering
Curriculum: Materials, structures, complex systems and architecture

Computational modelling of cell biomechanics

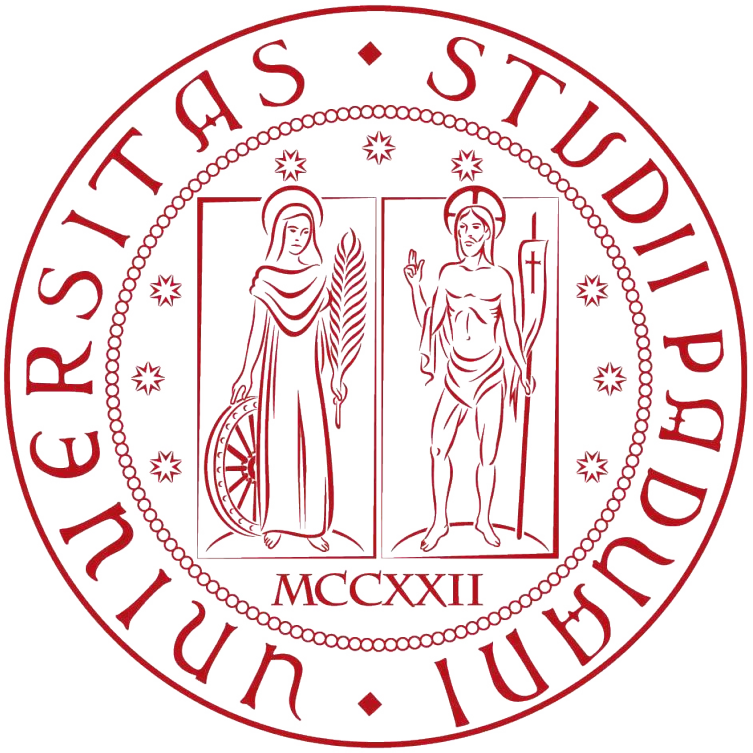

COORDINATOR: Prof. Massimiliano Ferronato
SUPERVISOR: Prof. Valentina Salomoni
CO-SUPERVISOR: Prof. Emanuele Luigi Carniel

PhD STUDENT: Alessandro Arduino

Academic Year 2023/2024

Acknowledgments

I want to thank all my professors and colleagues who helped me in shaping this work and who lent me their insights and expertise in order to create a qualitative and comprehensive work. In particular, I'd like to thank Prof. Valentina Salomoni for being my supervisor, Prof. Emanuele Luigi Carniel for being my co-supervisor, and Prof. Carmelo Majorana and Massimiliano Ferronato for their role as PhD course coordinators. I'd like to thank Dr Alice Berardo and Sofia Pettenuzzo for being an active part of my research process. Thanks to Sean for his help in identifying some of the issues with the FE models. A special thank you for the great support and opportunity given to me by Dr Eoin McEvoy. A final thank you to my family and friends who supported me in this incredible journey.

I dedicate this work to the loving memory of Annalisa and my father.

Abstract

The understanding of the human body mechanobiology has greatly increased over the years leading to better health outcomes in many medical fields. The powerful tools provided by methods such as finite element analysis have been proven effective in investigating, diagnosing and curing pathologies while also providing a framework which is cheap, reproducible and customisable. The field of cellular biomechanics can greatly benefit from these tools thanks to their ability to be adapted to the investigator's needs thus allowing testing setups which would not be possible otherwise and that would more closely reproduce the in vivo conditions of interest. For these reasons, this dissertation presents relevant advancements in the type and complexity of finite element models for the investigation of both healthy and pathological cells with a focus on cancerous cells. The first chapters of this work focus on providing a good understanding of the cell physiology. The focus is placed on the most mechanically relevant subcomponents of the cell both in a healthy and pathological state. Starting from this base, the work explores the current state of the art in terms of numerical models applied to cell biomechanics. The following chapters present the original contributions of the author. The purely mechanical models presented use the concepts of tensegrity and bendo-tensegrity to create models which can reproduce the mechanical response of a cell undergoing micropipette aspiration or atomic force indentation while increasing the level of accuracy and complexity achieved by the classical homogeneous models present in the literature. The capabilities of these models are compared to data from the literature in order to validate their ability to reproduce in-vitro tests. Another class of models is presented in this work: biomechanical models based on ion trafficking and mechanical responses to osmotic imbalances. The biomechanical models developed for this work show the potential of finite element models in bridging our understanding of cell physiology and cell biomechanics. These models have shown great potential in describing the response of the cell to both physical conditions (such as osmotic pressure fields) and mechanical stresses. Taken together, these two classes of models can greatly contribute to our understanding of the complex life of cells both from a biological and mechanical standpoint thus allowing us to take a first step in bridging these two fields.

Abstract

Gli avanzamenti nella comprensione degli aspetti meccano-biologici legati alla fisiologia del corpo umano stanno contribuendo a notevoli avanzamenti nel campo medico. Strumenti inerenti alla meccanica computazionale, quali le tecniche di analisi agli elementi finiti, si sono dimostrati efficaci nell'affiancare il personale medico in processi quali la diagnostica e la cura di particolari patologie, nonché alla comprensione dei meccanismi alla loro origine ed evoluzione. Inoltre, tali metodologie definiscono una procedura in grado di fornire risultati riproducibili ed adattabili alle specifiche esigenze di ricerca. La biomeccanica cellulare, in particolare, può beneficiare di tali metodologie in quanto capace di rappresentare situazioni sperimentalmente non accessibili con gli strumenti attualmente disponibili, o di riprodurre scenari diversi con rapidità e precisione senza dover ricorrere ad interventi altrimenti invasivi. Per questi motivi, le attività del Dottorato di Ricerca si sono focalizzate nella realizzazione di modelli computazionali in grado di rappresentare cellule sane e malate (con attenzione particolare alle cellule tumorali) in diversi contesti ed a diversi gradi di complessità. I primi capitoli di questa tesi mirano a fornire una descrizione dettagliata dei principali aspetti fisiologici della cellula. Maggiore attenzione è stata rivolta alle sottocomponenti cellulari più rilevanti dal punto di vista meccanico sia nel caso di cellule sane che di cellule malate. Partendo da questi aspetti, la tesi procede con una descrizione dello stato dell'arte dei modelli computazionali impiegati nel campo della biomeccanica cellulare. I capitoli successivi presentano invece i contributi originali dell'autore. I modelli continuo-tensegrali e continuo-bendo-tensegrali sviluppati si sono dimostrati capaci di interpretare con precisione la risposta di una cellula a diversi stimoli meccanici, quali quelli dovuti ad aspirazione tramite micropipetta o all'indentazione tramite microscopio a forza atomica, dimostrandosi un avanzamento rispetto ai classici modelli omogeneizzati presenti in letteratura. I risultati ottenuti dall'impiego di questi modelli sono stati confrontati con dati sperimentali ottenuti da altri articoli scientifici per poterne valutare la capacità di riprodurre esperimenti in-vitro. In questo lavoro viene presentata anche un'altra tipologia di modelli computazionali basata sulla valutazione del traffico di ioni attraverso la membrana cellulare e la risposta della cellula a squilibri nella pressione osmotica percepiti. I modelli biomeccanici proposti, invece, dimostrano il potenziale delle analisi ad elementi finiti nell'unire aspetti biologici e meccanici in modelli in grado di simulare la risposta delle cellule a stimoli meccanici e a condizioni fisiologiche quali la variazione della pressione osmotica. Questi due tipi di modelli possono costituire un primo passo nell'espandere la nostra conoscenza della meccanica e della biologia delle cellule tenendo conto di quanto queste due realtà siano strettamente collegate.

Contents

List of Figures

List of Tables

Introduction

Neoplasms are common conditions in which a group of cells grow and subdivide uncontrollably as a result of the accumulation of genetic alterations of the DNA of the affected cells. The resulting mass (referred to as a tumour) can be either benign or malignant (or cancerous). While benign tumours may grow to significant sizes, they tend to stay localized and do not invade nearby tissues or spread to other organs. Malign tumours, on the other hand, can spread to different regions of the body, sometimes by means of the blood and lymph systems. It is estimated that the average American man has a 40% chance to develop a malign tumour in their lifetime and it is the cause of death for nearly 20% of the American population. Similar percentages can be found in many other developed countries.

Although many works have been published on the topic, there are still many unknowns when dealing whit tumour cells, especially from a mechanical standpoint. Tumours have been thoroughly studied from a chemical and pharmacological point of view but only in the last decades serious efforts have been made to describe their mechanical properties. The main obstacles in understanding and describing tumour mechanics can be found in its intrinsic inter and intra-tumour variability which is the fact that the same tumour cells present different mechanical responses in different people and even inside the same mass. Furthermore, experiments at the micro and nanoscale still present degrees of uncertainty due to the accuracy and resolution at such a scale. Moreover, these problems are accentuated when trying to sense and analyze the mechanical responses of tumour masses and their cells in-vivo. For these reasons, FE models of cells belonging to a tumour mass could greatly benefit research and understanding of this group of pathologies.

Of course, understanding tumour mechanics is no simple task and mechanical models on their own are not expected to provide final solutions to the problem but in order to truly understand how to deal with these diseases a more comprehensive approach is needed, taking both the biochemical and mechanical aspects together.

The aim of this work is to introduce new possibilities and paradigms to the modelling of cells and especially tumour cells while also keeping in consideration some of the main aspects of the anatomical and physiological aspects of tumours such as cell growth.

Objectives

This PhD thesis focuses on the development and validation of finite element models of healthy and tumour cells. Due to the complexity of cell biological and mechanical response to external stimuli, this goal has been subdivided into two main approaches:

- Development of purely mechanical models of the cell and its subcomponents;
- Creation of biomechanical models able to introduce the effects of osmotic challenges and cell biomass synthesis.

On the mechanical side, the main goal is to identify, develop and validate a series of finite element models able to capture the response of a cell undergoing micropipette aspiration and atomic force microscope indentation tests. The models developed are aimed at inquiring about the effect of introducing different levels of complexity both in the model discretization and the mechanical behaviour of its components with a particular focus on the cytoskeleton. The theoretical framework for this type of models is reported in chapters 4 and 6 while the experimental results can be found in chapters 5 and 6.

The biological models to be developed, on the other hand, aim at creating tools able to predict the volumetric response of a cell due to changes in the osmotic pressure present outside the cell and the synthesis of biomass during the cell cycle. These models are to be built taking into consideration all the major players in the ion fluxes through the cell membrane. The theoretical aspects of these models can be found in chapter 7 while the results of the simulations performed with these models can be found in chapter 8.

Obtaining such results can bring remarkable tools which can be used to deepen our understanding of cell biomechanics and how its behaviour can change due to pathological changes.

1 Biological aspects of the cell

The biological aspects of the cell presented in this chapter are taken from the Scitable e-book *Essentials of Cell Biology*(O'Connor, Adams, & Fairman, 2010). Whenever information is taken from other sources an adequate citation will be placed.

In order to understand the mechanical characteristics of a living cell it is undoubtedly necessary to overview some of the main aspects of cell biology. Reliable mathematical models of the change in volume of the cell(Jiang & Sun, 2013; McEvoy et al., 2020) and even ones that rely on passive mechanical models(L. Wang & Chen, 2019) take into account the cell anatomy and physiology in order to better represent this complex structure.

1.1 Anatomy and physiology of the healthy cell

Eukaryotic cells (or eukaryotes) are complex units and the most important component of most tissues and organs of living multicellular organisms. They represent the fundamental units of a body and they can differ greatly from one another in terms of functions, size, shape and so on. Because of this, the analysis of cell biology should be carried out for each type of cell individually. As the scope of this work is centred around the chondrocytes, all the aspects discussed will be true for this cell type and although most of these characteristics can be said to be true for other types of cells, not all of them are shared by all cells. A specific description of chondrocytes' physiology is presented in chapter 3.

Figure 1.1 gives a clear example of a typical human cell and its many complex components. Although all elements of the cell may seem big with respect to the whole cell size, it is important to notice that most images of cells are in fact not to scale. This is due to the fact that some components (such as ribosomes) would be too small to be depicted while being able to also appreciate other components.

As we are interested in describing the mechanical aspects of the cell, it is possible to omit a detailed explanation of each of the elements that compose this wonderful structure and focus only on the ones that, directly or indirectly, impact the cell's biomechanical behaviour.

The main structure that regulates the mechanical response of the cell is the cytoskeleton. This structure is able to provide the cell with its shape and the capability of action such as anchorage and even motion. The cytoskeleton is composed of three types of fibrous proteins: microtubules, actin filaments and intermediate filaments.

Microtubules are the biggest of the three with a radius of approximately 25 nm. They are made of subunits of tubulin and they constantly change their length by adding or removing units in response to external and internal stimuli. The microtubules are

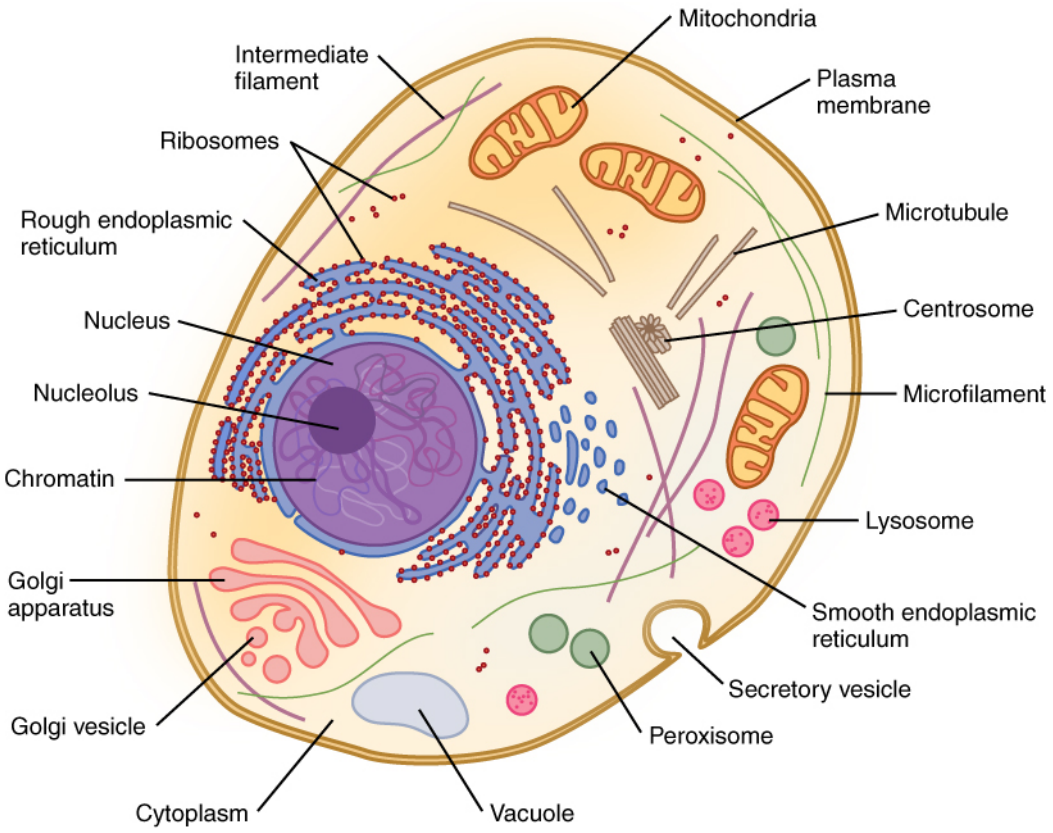

Figure 1.1: Example of the structure of a typical human cell and its components.

oriented in a somewhat radial organization, spreading from a central structure called the centrosome which is located near the nucleus of the cell. These fibres are mostly responsible for giving shape to the cell and contributing to its capability of passively sustaining external stresses but they also provide organization to the orientation and distribution of organelles inside the cell.

The actin filaments (also referred to as microfilaments) are the most abundant components of the cytoskeleton. They are made of subsequent units of actin leading to the formation of long fibre several nanometers long despite the small radius (approximately 7 nm). These fibres can polymerize and depolymerize leading to different lengths. It is worth noting that while the process of polymerization does not need the use of ATP, the usage of this energy source can greatly change the rate at which this process happens(GM., 2000). The actin filaments organize themselves in a complex network mostly located under the plasma membrane and linked to it via specific binding proteins. This structure contributes to the shape of the cell and gives the membrane its characteristics mechanical behaviour. A peculiar characteristic of the actin fibres is their capability of contracting by means of the motor protein myosin. Although this behaviour is the same encountered in muscle fibres, the cell actin-myosin complex is more sparse and not as well organized(GM., 2000). Nevertheless, this structure creates

an active component of the cytoskeleton by means of which the cell is able to actively change its mechanical response and perform complex tasks such as motion.

Finally, we have intermediate filaments. These fibres are arranged in a ropelike structure and act as a support to the microtubules by enhancing their strength and supporting their fragile structures. For this reason, they can be usually found in the same locations and arrangement as the microtubules. It is worth mentioning that while microtubules and microfilaments are common to all cells, some specific intermediate filaments can be found only in certain cells such as muscle cells and neurons.

In figure 1.2 it is possible to appreciate the complex structure of the cytoskeleton where the microtubules sprout from a central location near the cell nucleus and the actin filaments are spread near the cell membrane.

Aside from the cytoskeleton, the cytosol plays another key role in the mechanical behaviour of the cell. As stated earlier, the subcomponents of the cell (nucleus aside) are in fact very small. For this reason, the cell is mainly composed of water and solutes.

This composition makes it so the cell behaves differently depending on the rate of deformation performed on it[1]. Although the cell is usually depicted as a balloon full of water, it is actually able to change its water and solute content in response to changes in the external conditions(Jiang & Sun, 2013).

The cell membrane has many proteins embedded, some of which act as active or passive channels for the flow of water and solutes. Some of these channels are sensitive to the stress of the membrane (which is very much connected to the stress of the actin cortical network as explained earlier) and allow the passage of any solute with water without specificity. Active pumps, on the other hand, activate when solutes have to be transferred against the water gradient thus leading to an energy-consuming and ion-specific flow.

Because of this ability to change its volume, this aspect of the cell has to be taken into consideration in some applications in order to reach a more reliable model. It is worth mentioning that when the rate of deformation is relatively fast, the effects of pumps and leaks can be ignored. These are only some of the ways in which the cell is able to change its internal ion and water composition, voltage-sensitive channels and leak gates are also present in the cell but will not be used in the models presented in this work.

In figure 1.3 it is possible to appreciate a depiction of this kind of proteins.

The cell goes through many changes depending on what phase of the cell cycle it is experiencing. Usually, a cell has 5 distinct phases during the cycle: three gap phases (G_0, G_1 and G_2), a synthesis phase (S) and a mitosis phase (M). During the G_1 phase the cell goes through a series of internal checks in order to ensure that it is ready to move to the S phase during which the cell synthesizes the material necessary for the

[1]Details on the viscoelastic behaviour are left for chapter 2

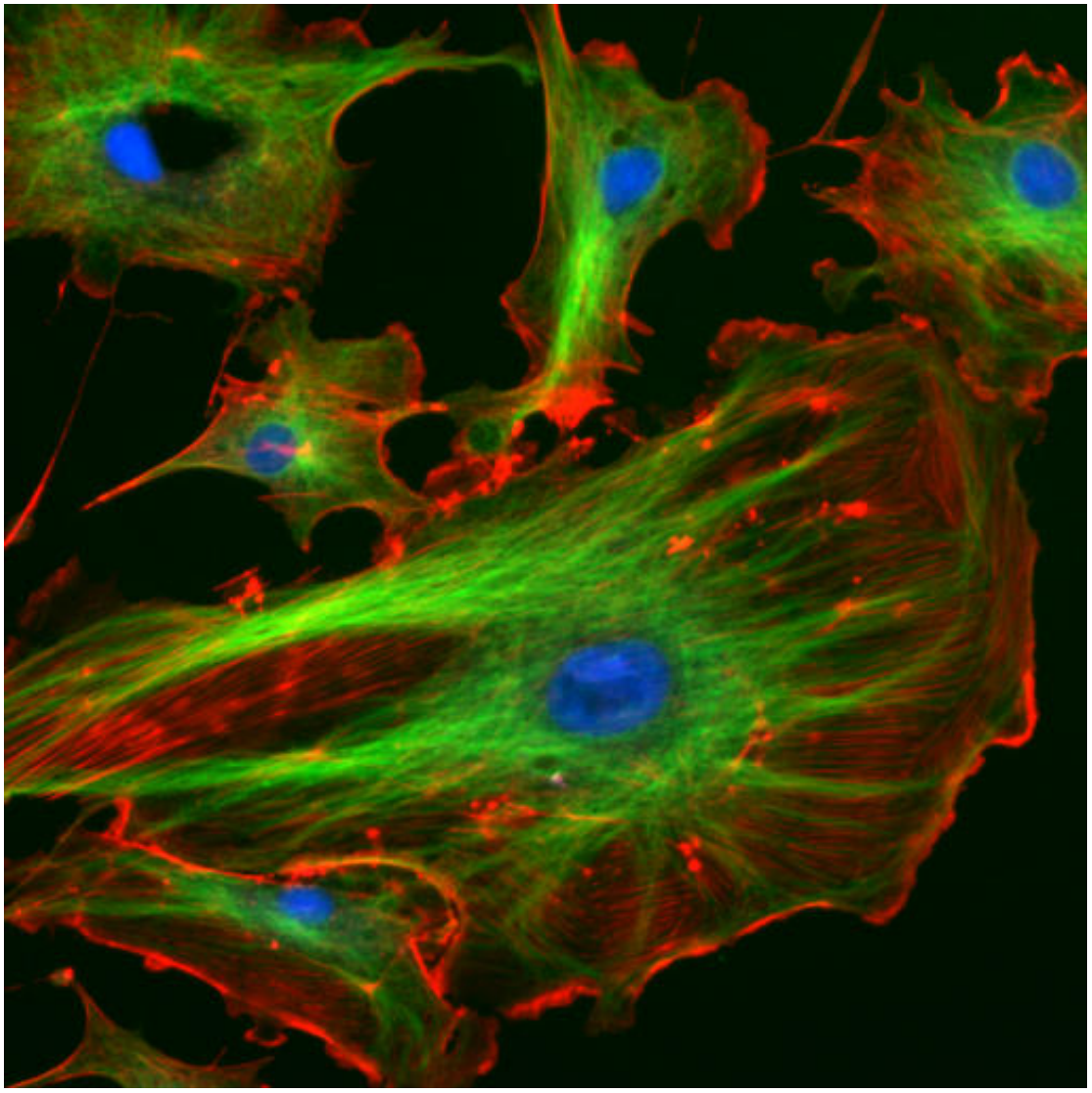

Figure 1.2: Image of a cell where the main structures of the cytoskeleton are made visible using different fluorescent dyes. The nucleus is stained blue while the actin network is in red and the microtubules appear in green.

mitosis. After the required material is produced (and DNA has been duplicated) the cell goes into the G_2 phase during which the cell controls to be perfectly ready for mitosis. If all the checks go through without problems, the cell goes through mitosis and divides into two identical cells. If at any point of the phase G_1 the cell registers a signal adverse to the mitosis, the cell goes into a resting state G_0. Some cells like neurons and muscle cells never exit this cycle for the entire life of an individual or only do so in special cases.

Of course, some cells do not follow this scheme perfectly as some cells (like staminal cells) have the ability to change their phenotype thus leading to different types of cells.

In this work, we focus on cells in their resting phases G_0 and G_1. This restriction makes the arrangement of a model more feasible but is also convenient as most cell lives most

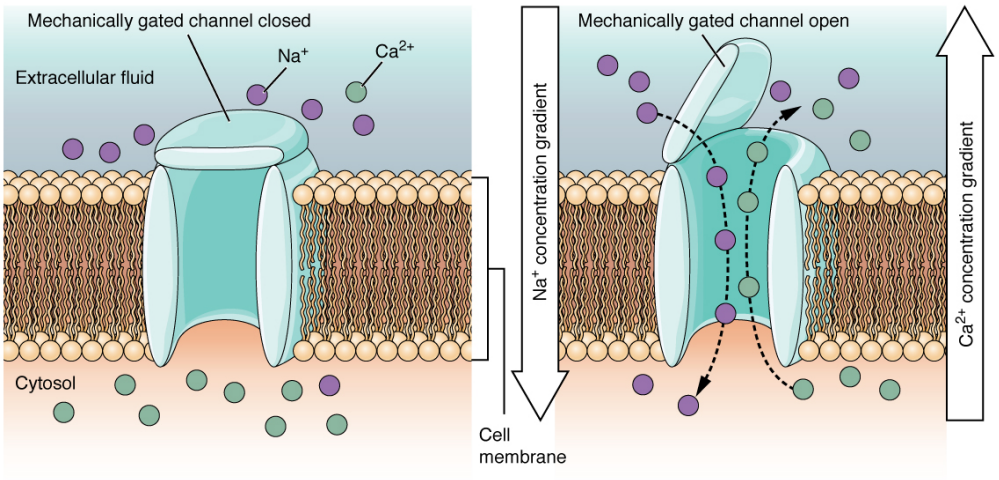

(a) Schematic representation of a mechano-sensitive channel.

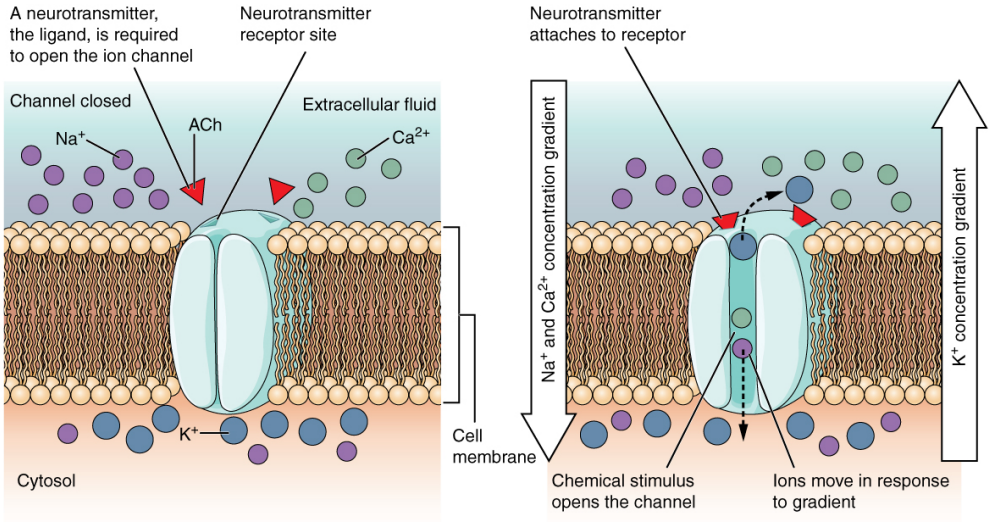

(b) Schematic representation of an active pump.

Figure 1.3: Some depictions of mechano-sensitive channels and active pumps of the cell membrane. These are only some of the possible transmembrane proteins that act as channels or pumps.

of their life in these phases.

Aside from the signals required for the cell to change phase during its life cycle, there are other types of control signals performed by the organism and cell itself to control how well the cell is performing its phenotypical behaviour. Some of these checks may end up signalling that the cell is no more of use to the organism. When the cell produces faulty proteins or simply does not work as intended, the cell receives signals to go into apoptosis which is the process by which a cell dies in order to be replaced by correctly functioning cells. As the organism ages or is exposed to some carcinogenic chemicals and pollutants the number of faulty cells grows significantly and the process of replacement

becomes more and more difficult.

1.2 Differences with a tumour cell

When genetic errors accumulate in a cell or a cluster of cells the organism tries to correct the faulty cells and signal them to go into apoptosis. Sometimes cells become resistant to this signal and thus become tumour cells.

Tumour cells lose the ability to read the signals from other cells or the organism and grow uncontrollably. When cell growth remains localized and doesn't develop symptoms or invade surrounding tissues, the resulting mass of cells is referred to as a benign tumour. On the other hand, when the cells start to break through the limits of their original tissue and spread to other regions of the body they are referred to as a malign or cancerous tumour. The process by which tumour cells migrate to other tissues is called metastasising and the resulting new colony of foreign cells is referred to as metastasis.

The Cancer Genome Atlas[2] project was created to better understand how these mutations occur and how do they lead to tumour cells. In their finds, they showed that most cells have between two to six mutations when they start the process of oncogenesis(Kandoth et al., 2013). Although tumour cells have on average 60 mutated genes, only a few of them are usually related to oncogenesis and cancerous processes. In most tumour cells the genes that regulate cellular activity, apoptosis and cellular division are mutated. This fact ends up making tumour cells more active than their healthy counterpart as well as more prone to uncontrolled division by means of being extremely susceptible to growth signals.

One mutation worth exploring is the code for the production of the p53 protein. This protein is responsible for checking the correctness of the DNA and its replication. If protein p53 does not signal the presence of transcription errors, the cell might not receive the needed signal to go into apoptosis. Such cell, over time, will accumulate mutated genes that can give rise to a tumour cell.

As tumour cells arise from the accumulation of mutated genes, the process of oncogenesis doesn't happen in a straight and fast process but until enough mutations are accumulated the cell might not behave abnormally thus not giving signals that could lead to an early diagnosis.

Taking all that has been said into consideration it is clear that tumour cells come with a great variety. One of the obstacles to studying this class of disease is in fact the intra-tumour and inter-tumour variability which is how tumours can be very different between individuals and even in the same organism.

Of course, tumours deriving from different organs or individuals have distinct character-

[2]Information regarding the TCGA and the related publications can be retrieved at `https://www.cancer.gov/about-nci/organization/ccg/research/structural-genomics/tcga/publications`

istics but even inside the same organism, the same tumour can give rise to cells behaving significantly differently. The process of mutation can be seen from a microevolutionary perspective: as a group of cells in a tumour develop a new advantageous mutation they can become predominant. This process might not produce a single new strand of the tumour and the original and new tumour can co-exist. Furthermore, if we consider metastasis, different populations in different body regions can evolve different traits with respect to the primary tumour(Stoecklein & Klein, 2010).

2 Cell biomechanics

The fact that the human body responds to mechanical forces is well-known: athletes stress their muscle fibres which adapt in response to exercise by building better muscles. Some changes are so relevant that can still be found in mummies and ancient human remains giving us insights into the lives of ancient humans. It's evident how mechanical actions can have an impact on the overall body but that is true even at a cellular level. Mechanical stimuli play an important role in many cellular activities. The mechanotransduction of such stimuli, which is the ability of the cell to sense and transform mechanical signals, is in fact a major regulator of cell activity. Anchorage-dependent cells, for example, are known to be able to change their behaviour depending on the stiffness of their substrate on which they adhere(Discher, Janmey, & Wang, 2005); the cell is able to contract the fibres composing the cytoskeleton thus causing this stimulus to be transferred to its surroundings via anchorage proteins such as cadherin and integrins. The entity of the perceived stiffness can cause the cell to reorganize its internal cytoskeletal structure.

Non-adherent cells, on the other hand, do sense their surroundings and can change their path during cell motility following a gradient in stiffness by a process called durotaxis(Discher et al., 2005). The mechanical signal sensed by the cell when attached to a substrate can influence the cell's behaviour: fibroblasts, for example, can modulate their production of actin-binding protein filaments by force-induced gene expression. This effect can even be coordinated between neighbouring fibroblasts that can attach to one another to sense their surrounding environment together and modulate their gene expression accordingly(Janmey & McCulloch, 2007).
As hinted earlier, the proteins by which the cell links to their surrounding are mainly directly linked to the cytoskeleton. By means of this connection, the cell is able to transfer the mechanical impulses it receives at a certain location to a completely different one through this network(N. Wang, Butler, & E., 1993). Furthermore, the structure of the cytoskeleton is able to reorganize when subjected to mechanical stress by either an internal remodelling(Smith, Deng, Fredberg, & Maksym, 2003) or by changing the arrangement and number of adhesion points on the surface of the cell by enrolling proteins like vinculin and talin which are essential components of the focal adhesion point structure(N. Wang et al., 1993; Janmey & McCulloch, 2007).

Figure 2.1 shows the schematic representation of the complex that is able to connect the external structures surrounding the cell to the nucleus at its core via the focal adhesion complex and the cytoskeletal structure.

From what has been discussed so far, it is clear that the nucleus itself plays a key role in response to such external stimuli. In order to exert such a biochemical response, the mechanical signals have to be sensed, transferred and interpreted by the cell nucleus and all of this process is done via specialized proteins. Defects in the production or

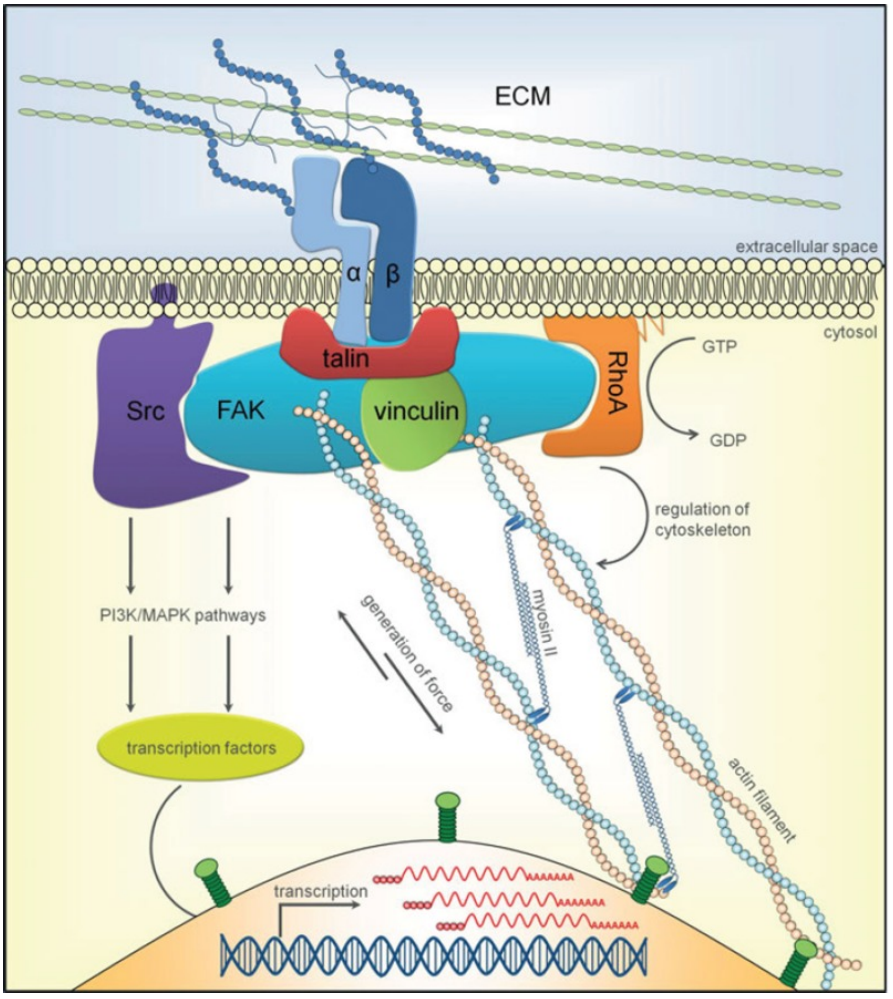

Figure 2.1: Schematic representation of a focal adhesion point. It is possible to appreciate the structure that links the ECM (or eventually other cells) through the linking proteins and to the nucleus of the cell via the cytoskeleton. By means of this transfer, some gene expression is regulated causing the reorganization of the cell's overall focal adhesion points.

functionality of such proteins have been shown to be linked with many diseases such as muscle dystrophy(Fedorchak, Kaminski, & Lammerding, 2014).
Even more complex responses can be achieved by mechanotransduction of external forces. Cells have been shown to be able to differentiate or de-differentiate according to the external environment as well as to go into apoptosis or proliferate(Vogel & Sheetz, 2006). All these aspects make the creation of accurate models of the cell quite difficult to develop. Even more when dealing with how different cell types show very specific mechanical behaviours.

The exceptional advancement in cell investigations of the last decades provided us with instruments that lead to the ability to test and evaluate the mechanical response of cells such as the Atomic Force Microscope (AFM) and the Micropipette Aspiration (MA).

Thanks to this tool we are able to measure the mechanical parameters of cells to build quantitatively viable models(Janmey & McCulloch, 2007). Although a general model encompassing all the different aspects described here would be a strenuous effort, one could focus on the ones perceived as the most relevant ones.

2.1 Mechanical aspects of cell subcomponents

In the following are presented the subcomponents of the cell that are relevant for its mechanical behaviour. Although cells are able to remodel and adjust their mechanical response, the components here described are taken as passive mechanical elements. This provides some limitations to the applicability of the models presented but the assumption of a passive mechanical behaviour is usually enough for simple and fast mechanical tests as the ones reported in this work and in the literature. A more active model will be presented in further chapters introducing the fluid flow of the water content of the cell as well as the flux of ions that regulate the volume and internal pressure of the cell. There are 4 major players when trying to describe the mechanical behaviour of the cell: the cytoplasm, the cytoskeleton, the plasma membrane and the cell nucleus. Each of these subcomponents interacts with one another to express the overall mechanical response of the cell.

2.1.1 Cytoplasm

The cytoplasm is the main component of the cell from a volume perspective. There is no clear definition of what is considered or not part of the cytoplasm. According to the National Cancer Institute and the National Human Genome Institute, the cytoplasm is limited to the liquid phase and its smaller solutes while in other works(Goodman, 2007) it is described as composed of everything outside the nucleus and within the plasma membrane. In this work, the cytoplasm is assumed to be all the components inside the cell membrane except for the cytoskeleton and nucleus. The ambiguity over the definition of the cytoplasm is not a concern for mechanical models of the cell. It is in fact commonly assumed that the organelles present in the cytoplasm do not provide a significant influence on the cell's mechanical response. The reason for separating the behaviour of the cytoplasm from that of the cytoskeleton is important as these two subcomponents will be treated and modelled separately when addressing the FEM models discussed in Chapter 4.

The cytoplasm exhibits a viscoelastic behaviour similar to that of water(Luby-Phelps, 1994). This is no surprise if we observe that most of it is indeed water and the remaining components (as explained earlier) float inside this liquid without providing significant mechanical contributions. Furthermore, the fact that such liquid phase is contained in a finite volume and surrounded by the plasma membrane, makes it so that the cytoplasm is often described as either a linear elastic(McGarry, Prendergast, et al., 2004) or viscoelastic(Guilak, Tedrow, & Burgkart, 2000) incompressible solid.

The mechanical behaviour of the cytoplasm is the most important one for the overall stiffness of the cell: although some works distinguish between the cytoplasm and other cellular subcomponents(Hu et al., 2017; Ren et al., 2020; Kwapiszewska et al., 2020), other researchers assign its mechanical properties to the entirety of the cell thus leading to a homogeneous solid structure with either viscoelastic(Guilak et al., 2000; E. M. Darling, Zauscher, Block, & Guilak, 2007) mechanical properties or other models such as biphasic mechanical one(Shin & Athanasiou, 1999; Guilak & Mow, 2000).

Thus, it is no surprise that different works registered different mechanical parameters when describing the mechanical behaviour of the cytoplasm and that the values used to describe it in this work might differ from them due to this.
As said, the cytoplasm is usually described as a solid or at most as a gel-like structure confined inside the plasma membrane. To the knowledge of the author, the vast majority of works describe the cell's cytoplasm (or the entire cell if treated as a homogeneous structure) as an incompressible body. This assumption is fair as long as the timescale is smaller than several minutes(McEvoy et al., 2020). Most works on cell biomechanics focus on ranges of about ~ 10 seconds making the assumption of incompressibility fair in certain scenarios.

The cytoplasm, on the other hand, is able to change its volume by means of channels and pumps like the ones described in the previous chapter. Because of this, the assumption of incompressibility should not be taken lightly but should rather be used with caution.

2.1.2 Cytoskeleton

The cytoskeleton is a complex structure made of three protein filaments: the actin filaments, the microtubules and the intermediate filaments. These proteins arrange themselves in a complex network which is vital to many mechanical processes such as motion, cell shape, cell division, adhesion and more(Hohmann & Dehghani, 2019). Hereafter, the role of each of these subcomponents is described in detail to capture the complexity and importance of this structure to the overall mechanical response.

The actin filaments are present in the cell in two possible states: as free monomers called globular actin (or G-actin) or as long polymeric chains called filamentous actin (or F-actin). Actin is the most active of the three components of the cytoskeleton and it is known to be able to greatly change its structural organization over a timeframe of just some minutes(Hohmann & Dehghani, 2019).
When actin polymerizes to form longer chains, it creates two ends usually referred to as the positive (+) end and the minus (-) end. Once the two ends are clearly defined, the actin polymerizes at different speeds along these two ends leading to faster nucleation on the + end while it slows down the accumulation of more G-actin on the minus end. This imbalance can reach stages in which the minus end is inhibited from causing more nucleation or even to a state of depolymerization(Pollard, Blanchoin, & Mullins, 2000). Many causes can modulate the speed and direction of this reshaping process. One

process is the synthesis of proteins like formins and profilin which are known to be able to modulate the polymerization process leading to greater control of how much of the G-actin is reorganized as F-actin(Kovar, Harris, Mahaffy, Higgs, & Pollard, 2006).
Actin fibres can be linked to one another to form more complex systems. Many proteins interact and bind actin filaments together to form bundles or cross-linked networks. Because of this linking the actin network can have very different mechanical responses depending on the type of structure formed and each of these networks serves a specific function whether it is related to motility, contraction or shape preservation(Hohmann & Dehghani, 2019). Most of the binding proteins act in a passive manner simply linking different filaments together and for different amounts of time. It is in fact worth remembering that the cytoskeleton is a continuously evolving structure that reacts to external and internal stimuli by reorganizing its network. One of these proteins has an active behaviour which gives the actin network a peculiar behaviour: myosin. Similarly to what happens in muscles, the myosin can bind to two actin filaments and cause a sliding movement between the two thus enabling contraction of the overall filament bundle or network. This in turn gives the actin network an active role in the modulation of the mechanical response of the cell(Hohmann & Dehghani, 2019).
Various actin structures can be found in different cells and each addresses a different and specific function such as motion, endocytosis, invasion or absorption(Kadzik, Homa, & Kovar, 2020). While not all these structures are present in all cells, the most common structures are the cortical network located in close proximity to the plasma membrane and the stress fibres that span the cell's length.
The stress fibres are large bundles of actin filaments that are attached directly or indirectly to the focal adhesion points on the cell membrane. These fibres are important for the presence of myosin in their structure giving them a central role in cell contractility. A specific network of stress fibres located near the nucleus is called the nucleus cap. This structure envelopes the nucleus and is thought to be one of the systems that transfer mechanical signals to the nucleus itself and regulate its shape(Khatau et al., 2009).
The actin cortex is 3D web located next to the plasma membrane. This structure is critical for the initial response of the cell to external stimuli while it is not so relevant for prolonged stresses as the actin network reshapes and modulates its arrangement(Hohmann & Dehghani, 2019). Furthermore, the contractility of this structure is what makes cells preserve their shape as the myosin activity in this region is connected to the absence of blebs, protrusion and other abnormal structures linked with motility(Kasza et al., 2007).
In figure 2.2 it is possible to appreciate a detail of the complexity of the actin network and to observe how actin fibres are more densely organized near the plasma membrane to form the actin cortex as well as some stress fibres directed toward the inner portion of the cell.

Microtubules are formed by two different heterodimers (α-tubulin and β-tubulin) which link together and form their typical hollow tube shape. Similarly to actin filaments,

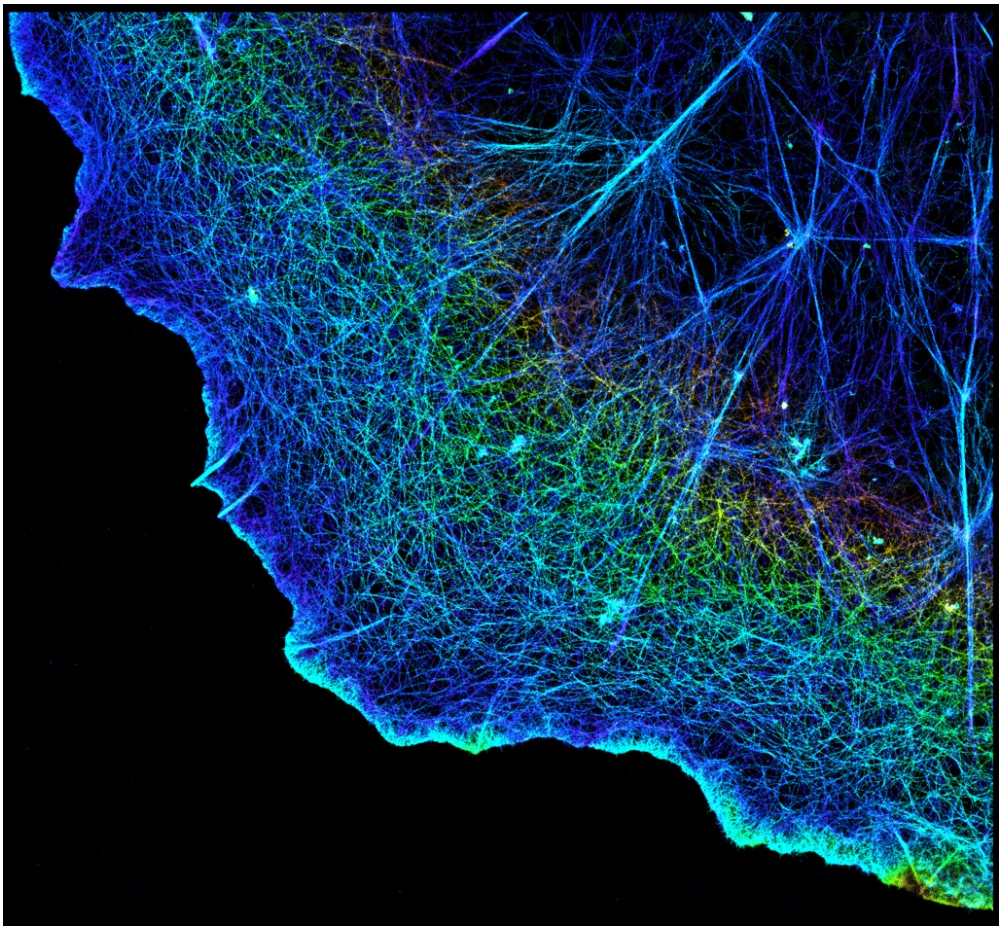

Figure 2.2: Actin filaments network in proximity to the plasma membrane. Imaged using stochastic optical reconstruction microscopy. The actin fibres are dyed with Alexa Fluor 647-phalloidin.

microtubules present a - end and a + end. The - end is associated to a central nucleation point called the microtubule organization centre (MTOC) from which they grow radially toward the cell membrane(Hohmann & Dehghani, 2019).
The single microtubule goes through cycles of growth and shrinkage but its structure can also collapse in an event called catastrophe during which the microtubule quickly depolymerizes. The polymerization and depolymerization processes are mainly regulated by guanosine triphosphate (GTP). This compound binds to the tubulin heterodimers and stabilizes them when forming long chains. The GTP-bound tubulin is especially present at the + end forming a GTP cap that further boosts the polymerization process. After some time, the GTP may hydrolyse and turn into guanosine diphosphate (GDP) causing instability in the microtubule chain. When enough GTP-bound dimers are converted into GDP-bound and especially if this happens at the + end of the microtubule, the structure collapses and depolymerizes quickly in a process called catastrophe(Dimitrov et al., 2008). The catastrophe doesn't always lead to a complete depolymerization of the entire microtubule. If enough GTP-bound tubulins are still present in the microtubule, a

new GTP cap can be formed and then the rescue process can initiate and the microtubule starts growing again chaining further GTP-bound tubulin(Dimitrov et al., 2008).
It is clear that the structure of the microtubule network is very dynamic. The polymerization and depolymerization processes are so rapid that the entire structure is referred to as dynamically unstable. The time scale for this process is reported to be on a scale of minutes and sometimes even seconds(Desai & Mitchison, 1997). Aside from GTP, other compounds can interact with the microtubule either at its + end or along its structure. These proteins can either stabilize or destabilize the microtubule structure and thus can regulate its polymerization process(Hohmann & Dehghani, 2019).

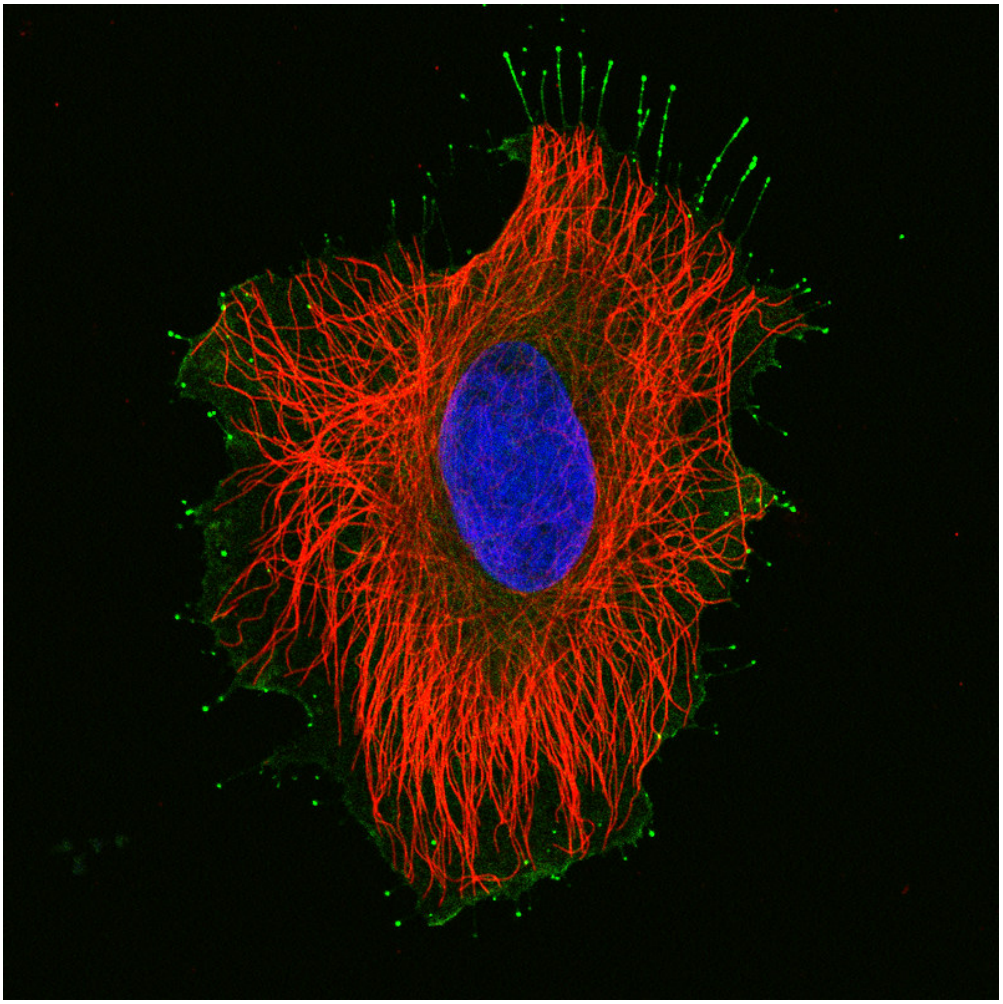

Figure 2.3: Microtubule filaments (red) radiating from the MTOC toward the cell membrane.

In figure 2.3 it is possible to appreciate the radial structure of the microtubules (in red) sprouting from a common region located near the cell nucleus. This is the typical shape of the microtubules network but it is not the only possible one: neurons and intestinal cells, for example, show multiple MTOCs and their microtubules are organized in long strains arranged in a somewhat parallel pattern(Sanchez & Feldman, 2017).

The network of microtubules is used by motor proteins to transfer materials of all sorts (such as membrane components, intermediate filaments and other molecules) either towards the + end or the - end depending on the type of motor protein(Hohmann & Dehghani, 2019). On the mechanical side, microtubules are in general resistant to compression and have some role in the cell's shape although their role is now being disputed by the fact that compressive stresses can cause catastrophes.

The last class of protein filaments that are part of the cytoskeleton are the intermediate filaments. These fibres are actually a large group of proteins that are usually grouped into 5 different classes. While the first 4 classes relate to filaments present in the cytoplasm, the fifth class is composed of intermediate filaments located near the nucleus of the cell(Hohmann & Dehghani, 2019).
Although many different proteins are classified as intermediate filaments, their structure is fairly similar to one another: two monomers of the same protein are coiled to each other to form a dimer. Two dimers link together to form a tetramer and the union of 8 tetramer makes up a unit of the intermediate filament(Hohmann & Dehghani, 2019).
Differently from other protein filaments, the intermediate filaments polymerization process does not appear to be regulated by other cofactors. Nevertheless, other physical quantities, like temperature, are able to modulate the rate at which certain types of intermediate filaments polymerize(Herrmann, Kreplak, & Aebi, 2004).

Intermediate filaments are organized in dense meshes mostly located near the nucleus but they can also be found near the actin cortex and in adhesion complexes. This network is capable of anchoring organelles and thus it has a major role in the spatial organization of the cell. Furthermore, the intermediate filaments are believed to act as mechanical buffers for the cell(Hohmann & Dehghani, 2019). Another characteristic of this network is its ability to link the so-called cytoplasmic cytoskeleton to the nuclear envelope. This feature allows the intermediate filaments to play a significant role in transferring signals from the cytoskeleton to the nucleus for mechanotransduction(Hohmann & Dehghani, 2019). One note has to be made to the use of intermediate filaments in in-silico models. Although they are instrumental in transferring mechanical stresses to the nucleus, most models do not include them as sometimes a simple direct attachment of these proteins to the nucleus can be sufficient to represent the mechanical transfer of stresses and stretches.

2.1.3 Plasma membrane

The cell membrane is a complex structure that surrounds the cell determining its volume and shape. Being the frontier of the cell, the membrane is involved in all types of interactions with the outside world whether their origin is biochemical, mechanical or any other sort. To this day, the model that has been found to better encompass all the most relevant aspects of this structure is the Fluid Mosaic Model (FMM) by Singer and Nicolson(Singer & Nicolson, 1972). Although the model might seem dated,

many updates have been made to it over the years(Nicolson & de Mattos, 2023). The FMM describes the plasma membrane as a phospholipid bilayer matrix where membrane proteins are located. These proteins can be either integral (or transmembrane) or they can be located only on one side of the structure giving the membrane an asymmetric layout. Furthermore, it is possible to define specific domains of the plasma membrane based on the type of proteins located in specific regions and the consequentially altered physical properties. These regions solve specific and important functions for the cell such as interacting with the environment or sensing external stimuli(Nicolson & de Mattos, 2023).

In figure 2.4 it is possible to observe a simple representation of the FMM of the cell membrane.

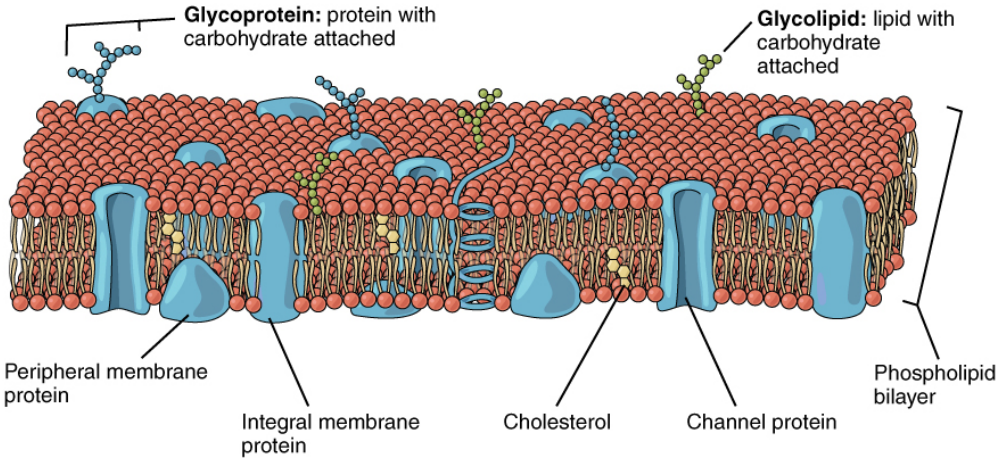

Figure 2.4: Representation of the FMM of the plasma membrane. The proteins present in this structure can span the entire thickness of the membrane (channels and integral proteins) or be located on only one side of the structure (peripheral proteins).

From a mechanical standpoint, the most important aspects of the plasma membrane are its ability to regulate the traffic of solutes and to host the anchorage sites for the actin cortex. The behaviour of the actin cortex has already been discussed in the previous section and will not be repeated here.

On itself, the membrane is shown to act as an inelastic film as it is able to expand by only 2-3% from its resting configuration before undergoing rupture(Apodaca, 2002). In most cases, cells' membranes display "membrane reservoirs" in the form of microvilli and folds that make the cell able to expand without reaching the failure point for the membrane too soon.

Concerning the regulation of the traffic of molecules throughout the membrane, this aspect is known to be modulated by both environmental stresses (such as osmotic stress) and mechanical stimuli(Apodaca, 2002). In the literature are present some mathematical models that partially capture the intricate systems involved in this equilibrium and one

of the most noteworthy is the Jiang-Sun model(Jiang & Sun, 2013). This model takes into account both the passive and active channels/pumps to create a comprehensive description of the coupling between the osmotic pressure, the hydrostatic pressure and the flow of both water and solutes throughout the cell membrane. Furthermore, the model is able to capture the connection between the mechanical stress on the actin cortex and fluid flow thus accounting for the mechanosensitive channels described in Chapter 1.

The cell membrane is also able to modulate its tension by regulating the process of endo/exocytosis. When the plasma membrane is tensed due to external stimuli, the cell is able to downregulate exocytosis and upregulate endocytosis thus providing a net increase in the available membrane and finally reducing the cortical stress(Apodaca, 2002).

2.1.4 Nucleus

The nucleus is one of the biggest subcomponents in human cells and stores the information required for its physiological functions. It is composed of an external membrane called the nuclear envelope which differs from the plasma membrane being made of two layers. Similarly to the plasma membrane, the nuclear envelope presents many proteins on its surface some of which are transmembrane proteins forming selective pores for the passage of molecules such as mRNA(O'Connor et al., 2010). Inside the nuclear envelope are stored the 46 chromosomes that make up the genetic code of a specific person. Chromosomes are stored inside the nucleus in an apparently disorganized but compact arrangement in the form of chromatin. Chromatin strings are linked to the internal part of the nuclear envelope by means of a family of intermediate filaments present only in the nucleus of the cell called laminins(Davidson, 2000). The nucleus is directly connected to the endoplasmatic reticulum, a structure rich in ribosomes where protein synthesis occurs(Davidson, 2000).

As described earlier, the nucleus is directly connected to the cytoskeleton in many ways. Actin filaments, microtubules and intermediate filaments bind to a series of proteins called nesprin located on the nuclear envelope(Song, Soto, Chen, Yang, & Li, 2020). Because of this structure, external mechanical stimuli are directly transferred to the nuclear envelope which changes shape together with the cell. Nuclear deformations translate into stretching and displacement of the chromatin present in the nucleus exposing certain sites and hiding others and thus modulating gene expression(Song et al., 2020).

Figure 2.5 depicts a schematic representation of a typical cell nucleus together with the endoplasmatic reticulum.

When the external stimuli cease, the nucleus is rapidly restored to its former shape and size by the cytoskeleton(Song et al., 2020). Some studies have shown how the

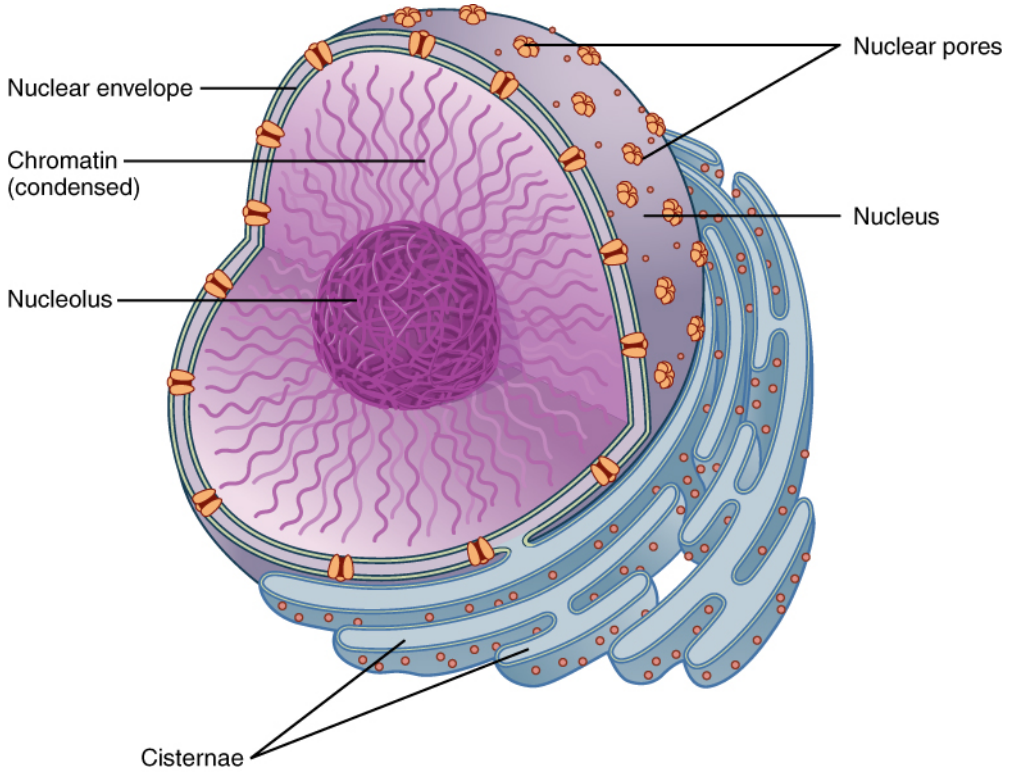

Figure 2.5: Schematic representation of the cell Nucleus. It is possible to appreciate the double bilayer membrane constituting the nuclear envelope with its nuclear pores, and the endoplasmatic reticulum with ribosomes embedded on its surface. Inside the nucleus, genetic information is stored in the form of chromatin linked to the internal nuclear envelope by means of the nuclear lamina.

connection between the stiffness of the nucleus and the connection of the chromatin to the nuclear envelope highlighting how chromatin itself plays a role in determining the nucleus' mechanical response(Schreiner, Koo, Zhao, Mochrie, & King, 2015).

The nucleus appears to be significantly stiffer than the rest of the cell although there is no consensus on a quantitative ratio between these two quantities. Some works report the nucleus being 10 times stiffer than the cytoplasm(Caille, Thoumine, Tardy, & Meister, 2002) while others attest that 1.1-1.4 is a more reasonable value(Ofek, Natoli, & Athanasiou, 2009). This discrepancy can be attributed to the different strategies used in isolating cell nuclei and the methodology used to assess the stiffness as well as the type of cell used in the study. In this work, a ratio of about 4 is used since it was the most commonly found in the literature concerning chondrocytes.

The aspects described in this chapter are generally true for most cells in the human body and can be taken as a solid ground on which it is possible to build a better understanding of specific cell types.

2.2 Tumour cells' biomechanics

When a cell moves from its healthy state to a tumour and later cancer state, the cells' response to mechanical stimuli changes. As explained in chapter 1, cancer cells can spread to different regions from the primary tumour forming a new colony of tumour cells that will give rise to metastasis. In order to do that the cell first needs to detach itself from the surrounding ECM and to move through it to invade the surrounding tissue. Being able to move through the ECM doesn't allow a cell to actually migrate very far from the primary tumour. On the other hand, if the cell is able to enter the bloodstream via a process called intravasation, it can use the blood vessel to reach very far and unexpected regions of the body. Again, in a process called extravasation, the cell can exit the bloodstream and anchor itself into a new tissue where it can give rise to a new cancer colony which, over time, will develop into a fully-fledged metastasis. It is worth noting that in most cases the new colony is developed by a cohort of cells rather than just from a single cancer cell(Alibert, Goud, & Manneville, 2017). A representation of this process is depicted in figure 2.6.

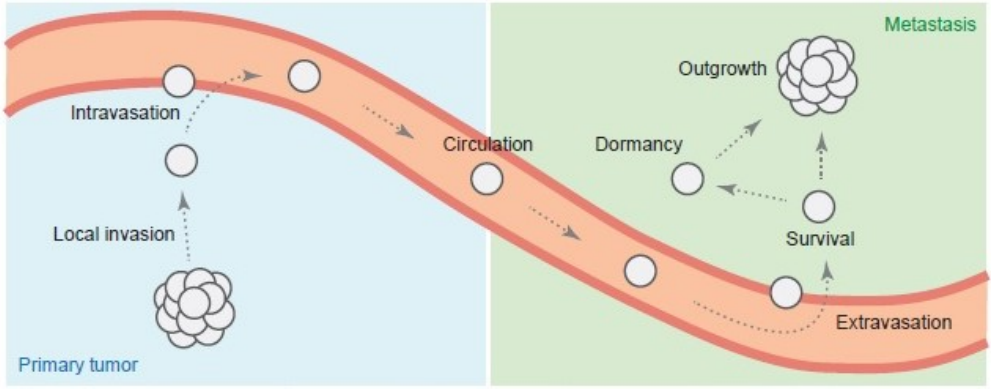

Figure 2.6: Representation of the journey of a cancer cell from the primary tumour region to the metastatic one where a secondary tumour is developed.

It is clear that in order to do this the cell has to be more compliant and thus able to flow and squeeze through narrow regions such as the space between the endothelial cells paving the blood vessels. Moreover, recent findings suggest that mechanical alterations of the cell's mechanical response and of the ECM are in fact necessary to turn a cell from a cancer precursor to an actual cancer(Panciera et al., 2020).

In the following, a brief description of the main changes observed in cancer cells' sub-components is presented posing specific attention to the elements previously described for the healthy cell.

2.2.1 Extracellular matrix

Most people are familiar with the easiest type of self-screening against most types of cancers: palpation in search of previously unnoticed nodules. What people are educated

to do is to look for a stiff region in an otherwise homogeneous tissue. This would have you assume that cancer cells are in fact stiffer and less compliant with respect to healthy cells but the opposite has been extensively reported to be true(Guilak, 2000; E. M. Darling et al., 2007; Huang, Kamm, & Lee, 2004; Alibert et al., 2017). The apparent stiffness of a cancer mass is actually due to the change in the extracellular matrix (ECM) protein concentration, material deposition and increased matrix crosslinking(Butcher, Alliston, & Weaver, 2009; Mohammadi & Sahai, 2018).

As the tumour develops it will absorb most of the nutrients in the area leading to hypoxia. Furthermore, the presence of the tumour typically leads to an upregulation of the Transforming Growth Factor-β (TGF-β) a growth factor responsible, among other things, for the regulation of ECM's proteins production and remodelling(Mohammadi & Sahai, 2018). Although growth factors and proteins that regulate the degradation of the ECM are also upregulated, the effect of TGF-β and other factors win over the latter thus causing a more densely populated and stiffer matrix. Matrix deposition is not the only factor that plays a role in changing the mechanical properties of the ECM surrounding a tumour, the increased cross-linking due to the aforementioned factors also plays a role in creating a stiffer ECM. Furthermore, a highly crosslinked ECM leads to higher apparent stiffness when the tumour grows in the area causing greater levels of ECM stretching(Mohammadi & Sahai, 2018). It has been found that both luminal differentiated cells and luminal progenitor cells (progenitors of some types of prostate and mammary tumours) adequately altered to express oncogenic traits weren't able to self-renew and give rise to cancer colonies when the stiffness of the substrate in which they were placed was not stiff enough(Panciera et al., 2020). Taking this into account it is possible to observe that if a stiffer ECM leads to the transition to an active or more malignant state in cells, the resulting proliferation creates a feedback loop where the increase in cells' number causes an increase in ECM stiffness(Mohammadi & Sahai, 2018). Furthermore, it has been found that an increase in ECM stiffness is linked to an increase in migratory behaviour in cancer cells. This migration is usually not mediated by cellular attachment to the matrix but rather from the contractility of the actomyosin complex present in the cytoskeleton(Mohammadi & Sahai, 2018). It is worth noting that the stiffness gradient due to the inhomogeneity of the dysregulated ECM can guide cells' migration via a process called durotaxis. The reduced adhesion of cells to the ECM is usually seen in cell-cell interaction thus increasing the likelihood of the detachment of a single cell or a small of group of cells from the primary tumour(Alibert et al., 2017). Since the stiffness of the ECM has been found to be fundamental for cancer activation and development, one might conclude that when a cohort of cells migrate to a different environment, it will not be able to develop a metastatic site. The reasons why cancer cells can create active colonies in different regions are linked to the fact that the tumour needs a stiff environment to first develop cancer-like gene expression but once this process has been completed the cell will be able to thrive in any new region and over time will slowly stiffen any other environment in which it will set(Mohammadi & Sahai,

2018). The process by which cells transition to a migratory and invasive phenotype is referred to as endothelial-mesenchymal transition (EMT)(Alibert et al., 2017). As hinted in chapter 1, the new colony can develop very different traits if compared to the primary tumour. This process of altered evolution between the two tumours starts already when a cell migrates to a new region. The act of detaching and migrating includes in itself a different gene expression but the act of squeezing the cell nucleus through the narrow gaps of the dense tumoral ECM can lead to DNA damages that can alter its genetic structure thus leading to new mutations.

2.2.2 Actin

Investigations on the mechanical changes in cancer cells' mechanobiology have shown that the EMT process leads to a change in the mechanical architecture and behaviour of the cell, especially of the cytoskeleton. For example, it has been found that the relative amounts of G-actin and F-actin in the cell are different between healthy and tumour cells although the direction of this imbalance seems to be dependent on the cell type(Alibert et al., 2017). This imbalance can cause a different response of the cell to external mechanical stimuli. For example, in the work of Panciera et al. (Panciera et al., 2020) the authors were able to show how the F-actin network of tumour and healthy cells react similarly to a physiologically stiff ECM but that the F-actin network of the tumour cell was able to contract and react to this environment significantly more than the one of the healthy cells. This fact highlights how tumour cells are sensitive to a wider range of mechanical stimuli compared to healthy cells thus altering the physiological mechanotransduction process. Furthermore, the authors found that reducing the ECM stiffness in-vivo did indeed lead to no tumour formation. Interestingly, the organization of the actin network itself seems to be disrupted by the transition to malignant states. This reduced internal organization could explain why cancer cells act as if they were softer as they lack a properly functioning structure which is fundamental for the mechanical response of the cell. Furthermore, the magnitudes and type of mechanical in cancer cells seem to be significantly similar to the one of healthy cells in which the actin network was chemically disrupted(Alibert et al., 2017). This increase in mechanotransduction experienced by cancer cells exposed to a stiffer ECM might be linked to the increased contractile and traction forces generated by cancer cells(Alibert et al., 2017).

2.2.3 Microtubules

While the actin network seems to be highly affected by the transition from healthy to tumour cells, the microtubules seem to remain relatively unchanged both in their structure and organization. For example, breast cancer cells have been observed to have a slightly altered and less complex organization when seeded onto adhesive microplates, but the dissimilarities were reported to be very small(Alibert et al., 2017).

2.2.4 Interemediate filaments

Concerning intermediate filaments, the type of filaments that get upregulated and the ones that get downregulated seems to be highly dependent on the cell type. Most cancer cells will upregulate keratins while other proteins such as vimentin are only expressed in cancer cells with high metastatic potential. The most interesting fact concerning intermediate filaments is that their increase in quantity does not necessarily correspond to an increase in cells' stiffness. It has been observed that the organization of intermediate filaments' organization in the perinuclear region seems to be altered in cancer cells thus providing a reduced stiffness to the nuclear region(Alibert et al., 2017).

2.2.5 Nucleus

The nucleus itself is significantly altered in tumour cells. For example, the volume occupied is usually appreciably larger compared to healthy cells while the shape becomes more irregular. Furthermore, the production of the proteins that compose the nuclear envelope is altered leading to a more compliant nucleus prone to rupture. These aspects are instrumental for cell migration since the compliance of this subcomponent is crucial for the cell to be able to squeeze through the narrow gaps of a crowded ECM(Alibert et al., 2017). Finally, the plasma membrane is also affected by changes to a higher metastatic potential. The membrane has been observed to become softer and thus better allowing cancer cells to flow through the ECM(Alibert et al., 2017).

2.2.6 Tumour specificity

If what has been said so far regarding tumour cells' biomechanics holds true for most cancer cells, it is important to keep in mind that cancer cells can act very differently from each other. For example, cancer cells from a type of murine breast cancer appear to show a decrease in cell contractility and in migration velocity linked to an increase in metastatic potential(Alibert et al., 2017). Furthermore, although most studies agree that cancer cells are in general softer than their healthy counterparts, some works have found increased stiffness in specific cancer cells(G. Zhang, Long, Wu, & Yu, 2002).

3 Chondrocytes

As previously stated, this work focuses on the mechanical behaviour of healthy and tumour chondrocytes. A description of the cartilage physiology and mechanical behaviour are presented in this chapter and taken from a literature review article published earlier this year (Pettenuzzo et al., 2023).

Among the vast variability of cell types, chondrocytes present remarkable properties and capabilities. They are the architectural basis of cartilage, a tissue in charge of load bearing, shock absorption and the lubrication of joints throughout the body; they also form the first temporary template for the skeleton during human growth (Belluzzi et al., 2023). Chondrocytes are surrounded by the pericellular matrix (PCM) and the two together are referred to as the chondron. This term was first coined by Benninghoff et al. in 1925 to identify a structural unit including the chondrocyte and the surrounding microenvironment in hyaline cartilage (Benninghoff, 1925). The PCM is considered to be a buffer for physical forces between the chondrocyte and the extracellular matrix (ECM) (Guilak et al., 2006). If chondrocytes are subjected to abnormal mechanical stimuli (e.g., excessive loading, joint trauma or malalignment), their metabolism balance becomes altered, causing matrix loss and tissue degeneration, which can lead to osteoarthritis (OA) (Griffin & Guilak, 2005; Grodzinsky, Levenston, Jin, & Frank, 2000). Indeed, mechanical stimuli have been recognised among the key factors in the initiation and progression of OA (Morgenroth, Gellhorn, & Suri, 2012). In this scenario, chondrocyte mechanical properties have become of primary interest to create reliable computational models (Arduino et al., 2022), as well as to better understand the interaction with the PCM and ECM, especially due to the limited ability of articular cartilage (AC) to self-repair (Masson & Krawetz, 2020) and the lack of available clinical treatments to completely repair the tissue. Due to the increasing importance of chondrocyte biomechanics and their correlation with OA, it is important to have a clear understanding of the experimental procedures and the mechanical models used for these cells. Furthermore, it is necessary to be attentive to those procedures/variables that could have affected the obtained results, such as the isolation procedure used to obtain both chondrocytes and chondrons, the protocol for storing the samples, the type of mechanical tests performed on the samples and the mathematical models adopted to evaluate the results of the experiments performed.

3.1 Physiology of the chondrocyte

Chondrocytes are the only cell type present in the AC and represent 1–5% of cartilage tissue.

They originate from mesenchymal stem cells (derived from embryonic cells specific to the mesenchyme) and, in adult cartilage, are quiescent, fully differentiated cells that receive nutrients via diffusion from the articular surface. They are characterised by

the presence of the primary cilium, a short microtubule-rich appendage, which seems to play an important role as a mechanosensor (S. R. McGlashan, Jensen, & Poole, 2006; Ruhlen & Marberry, 2014). In general, cell adhesion molecules, cytoskeletal elements, matrix protein receptors, integrins, the primary cilium and mechanically activated ion channels are recognised as the mechanosensory players responsible for the chondrocyte's mechanical behaviour (Gilbert & Blain, 2018). Regarding mechanically gated ion channels, Piezo-type mechanosensitive ion channel component 1 (Piezo 1), Piezo-type mechanosensitive ion channel component 2 (Piezo 2) and the transient receptor potential vanilloid 4 (TRPV4) are of particular interest in regulating calcium influx in chondrocytes (M. Zhang, Meng, Wang, Chen, & Zhang, 2022). These channels are mechanical sensors present in different cell types and they seem to be involved in different diseases (H. Liu et al., 2022; Emmi et al., 2022; Savadipour et al., 2023).

Chondrocytes are responsible for the synthesis and degradation of the ECM (Bhosale & Richardson, 2008). The ECM is particularly enriched with collagen II and proteoglycans (PGs) forming networks containing hyaluronic acid (HA), glycosaminoglycans (GAGs), chondroitin sulphate, fibres, laminin and fibronectin. Thus, chondrocytes modulate the enzymatic breakdown of the ECM maintaining a balance between anabolic and catabolic ECM processes. When the balance is disrupted in favour of ECM catabolism, progressive AC degeneration occurs which could lead to OA (Goldring & Marcu, 2009). Chondrocyte physiology and control of matrix turnover are influenced by several environmental factors such as soluble mediators (e.g., growth factors and cytokines) and external tissue damage (Akkiraju & Nohe, 2015).

The ECM can be divided into the PCM, territorial matrix (TM) and interterritorial matrix (ITM), which differ in matrix composition and organisation (T. L. Vincent, McClurg, & Troeberg, 2022). The PCM represents a specialised thin layer of the ECM with a thickness of 2–4 μm and it is located around the chondrocyte. It is composed of aggrecan, HA, GAGs, and a particularly high concentration of type VI collagen, which is exclusively present in the PCM, and low or no type II collagen. The PCM plays a crucial role in the metabolic activity and mechanical properties of chondrocytes as it is involved in AC homeostasis, and in protecting chondrocytes from external stresses (Allen & Mao, 2004; Guilak & Mow, 2000; Wilusz, Zauscher, & Guilak, 2013; Hing, Sherwin, Ross, & Poole, 2002; Peters et al., 2011). Indeed, the PCM acts as a protective barrier for cells, enabling them to retain the width/volume of the chondrocyte during compression and allowing the translation of the mechanical stimuli to the cells (Ateshian, Chahine, Basalo, & Hung, 2004). The PCM is surrounded by the TM containing type II, IX and XI collagens. The ITM is the largest region and it is composed of a fibrillar collagen network formed by type II collagen fibrils containing type XI collagen within the fibril and type IX collagen on the fibril surface with the non-collagen domain exposed, allowing the interaction with other matrix components. The orientation of ITM collagen fibrils is different depending on the AC zone (Goldring & Marcu, 2009; A. R. Poole et al., 2001; Sophia Fox, Bedi, & Rodeo, 2009). In this regard, the AC can be divided into

three zones: the superficial zone, the middle zone and the deep zone. The superficial zone is characterised by thin collagen fibrils running parallel to the articular surface. In the middle zone, there is no particular orientation of the collagen fibrils, while they are perpendicularly oriented to the articular surface in the deep zone (Sophia Fox et al., 2009).

3.1.1 Osteoarthritic cartilage

Osteoarthritis (OA) is the most common form of arthritis; it is considered a leading cause of disability among older adults and a major public health concern (Kassebaum et al., 2016). The knee is the joint most frequently affected by OA followed by the hand and hip (Long et al., 2022; Favero et al., 2022). Historically, OA was considered a disease involving only the AC. During the last few years, the concept of OA has changed to one of it as a multifactorial whole joint disease involving not only cartilage but also meniscal degeneration, subchondral bone remodelling, inflammation and fibrosis of both the infrapatellar fat pad and synovial membrane (Belluzzi et al., 2023; Belluzzi, Stocco, et al., 2019; Belluzzi et al., 2017; Sanchez-Lopez, Coras, Torres, Lane, & Guma, 2022; Englund, Guermazi, & Lohmander, 2009; Battistelli et al., 2019; Donell, 2019; Favero et al., 2019; Martel-Pelletier et al., 2016; Fontanella et al., 2022).

OA changes determine the alteration of the biomechanical behaviour of different joint tissues (Belluzzi et al., 2023; Englund et al., 2009; Fontanella et al., 2022). Among the articular tissues, the AC plays a fundamental role in withstanding mechanical stress as it provides load-bearing surfaces along with low friction and wear resistance, and gliding properties (Belluzzi et al., 2023; K. R. Vincent, Conrad, Fregly, & Vincent, 2012; Temple-Wong et al., 2009). Furthermore, the AC allows the support and redistribution of the compressive, tensile and shear forces originating during joint articulation (Statham, Jones, Jennings, & Fermor, 2022; Englund, 2023; Olivotto et al., 2022). Several risk factors are associated with OA including age, sex, obesity, ethnicity, genetics and previous history of injury or joint trauma such as meniscal damage (Englund, 2023; Olivotto et al., 2022; Palazzo, Nguyen, Lefevre-Colau, Rannou, & Poiraudeau, 2016). Among the different risk factors associated with OA development, ageing plays a significant role and it should be noted that joint ageing and OA are not the same but ageing changes can facilitate the development of OA (Loeser, 2017). During ageing, the AC becomes thinner with a slightly brown appearance due to advanced glycation end-products that modify the biomechanical behaviour of the tissue (Loeser, 2017). OA development and progression are also supported by chronic low-grade local and systemic inflammation through the release of inflammatory molecules affecting chondrocytes' structural and metabolic activities (D. Chen et al., 2017). Due to OA onset and development, the AC undergoes structural remodelling driven by many factors including mechanical stresses (wear and tear due to an increase in the superficial roughness (Berardo & Pugno, 2020)), genetic predisposition and low-grade inflammation (Belluzzi et al., 2017; Xiao, Su, Hou, Chen, & Lin, 2018; Loeser, Goldring, Scanzello, & Goldring,

2012; Torzilli & Allen, 2022).

The main cellular events underlying OA cartilage destruction are ECM fibrillation and degradation secondary to mechanical breakdown and the up-regulation of matrix-degrading enzymes triggering a proinflammatory cascade, collagen denaturation (especially type II collagen) and the loss of PGs resulting in a softer ECM (Torzilli & Allen, 2022; C. Liu et al., 2018; Goldring, 2012). Moreover, inflammatory cytokines and other molecules released by the synovial membrane stimulated by damage-associated molecular patterns determine the instauration of a vicious cycle, which leads to cartilage degeneration (Belluzzi, Olivotto, et al., 2019).

Chondrocytes acquire a hypertrophy-like phenotype determining an altered matrix production coupled with an increase of matrix-degrading enzymes' expression (i.e., metalloproteinases (Singh, Marcu, Goldring, & Otero, 2019)). In early OA, there is an attempt to regenerate/repair the matrix by increasing the synthetic activity (increased ratio of collagen/aggrecan (Maldonado, Nam, et al., 2013; Lorenzo, Bayliss, & Heinegård, 2004)). However, this process induces PG leakage and type II collagen degradation in the cartilage superficial zone with an increase in water content determining a reduction in ECM tensile strength (Martínez-Moreno, Jiménez, Gálvez-Martín, Rus, & Marchal, 2019). As OA progresses, chondrocytes appear to be organised in clusters. At late stages of OA, there is a decrease in chondrocyte density because of chondrocytes' death. Interestingly, only a few cells show evidence of classical apoptosis, while the majority undergo apoptosis in a non-classical manner (expansion of the rough endoplasmic reticulum and Golgi apparatus, frequent autophagic vacuoles, extrusion of cellular material into the extracellular space and final disintegration of cell remnants) called "chondroptosis" (Roach, Aigner, & Kouri, 2004; Salucci, Falcieri, & Battistelli, 2022). An increased number of chondrocytes display a senescence-associated phenotype (Loeser, 2013). The primary cilia change their orientation only in superficial cartilage. While they are found to be perpendicular to the AC surfacer in normal healthy AC, In OA cartilage they are oriented toward the center of abnormal cell clusters (Yuan & Yang, 2016). Moreover, there is an increase in cilia length and in the overall percentage of ciliated chondrocytes furthering the impaired signalling in OA cartilage (S. McGlashan, Cluett, Jensen, & Poole, 2008).

It has been shown that Piezo1/TRPV4 communicate with each other (Piezo1 activation inhibits subsequent TRPV4 activation and vice versa), which seems to be altered in OA chondrocytes altering metalloproteinases, collagen and interleukin gene expression (Steinecker-Frohnwieser et al., 2023).

An OA PCM structure appears disrupted with an altered composition determining changes in the mechanical function as well (Guilak, Nims, Dicks, Wu, & Meulenbelt, 2018). Interestingly, chondrocyte proliferation and cluster formation seem to be preceded by early changes in the collagen and proteoglycan distribution of the PCM in the chondron that appears to be enlarged and loosely organised(C. A. Poole, Matsuoka,

& Schofield, 1991; G. Lee, Paul, Slabaugh, & Kelley, 2000). In particular, there is an up-regulation of type VI collagen showing zone-dependent expression (G. Lee et al., 2000).

3.2 Experimental Methods for cells

A brief introduction to the various methods used to evaluate the mechanical aspects of cells is here reported. Further details are left for chapter 5 with a focus on atomic force microscopy and micropipette aspiration.

Chondrocytes embedded in the ECM are constantly exposed to mechanical loading, and cartilage mechanobiology is modulated by their mechanical signals. For this reason, the quantification of chondrocytes' mechanical properties can lead to a better understanding of cartilage biomechanics and mechanobiology, along with the identification of the main factors involved in their alteration (C. Chen, Tambe, Deng, & Yang, 2013). The mechanical properties of chondrocytes have been quantified using several measurement methods in conjunction with theoretical models. The most commonly used methods to evaluate single-cell mechanical properties are atomic force microscopy (AFM), micropipette aspiration (MPA), cytoindentation and micromanipulation techniques, described below.

3.2.1 Atomic Force Microscopy

The AFM is one of the most commonly applied techniques for material characterisation at the micro and nanoscale, to extract local mechanical properties of a material or to describe its microstructures and texture. The common setup is formed by a flexible cantilever beam with a tip that can have different shapes and sizes.

As a matter of fact, indenting a different region of a cell or using different experimental setups (e.g., changing the tip speed or shape) can lead to significantly different results. The deflection of the cantilever beam, which represents cell deformation, is measured by a laser. AFM has become quite popular for cell mechanical testing as it combines three-dimensional imaging at the nanoscale with the nanoindentation of cells and allows measurements of various cell regions, such as its surface, its subcomponents or the whole cell (Florea, Jakorinne, Lammi, Davidescu, & Korhonen, 2014). When referring to chondrocytes, Darling et al. report a mean constant displacement of about 1 ± 0.3 μm which is applied to the cell using a microscopic cantilever tip made of glass or silicon nitride, usually designed ad hoc. The force applied to the cell is determined by multiplying the cantilever stiffness (the known quantity) by its deflection. Then, from the force-displacement data, it is possible to determine the mechanical parameters of chondrocytes such as the elastic modulus.

3.2.2 Micropipette Aspiration

MPA is a versatile and widely used technique for determining the mechanical properties of living cells (Jones et al., 1999). This is usually performed by applying a negative suction pressure by means of a pressure control system directly connected to a micropipette (diameter ranging from less than one micron to tens of microns (González-Bermúdez, Guinea, & Plaza, 2019)). The micropipette is positioned close to the cell surface and the negative pressure acts as an attractive force deforming the cell shape. By maintaining constant and stable pressure on the cell, it is possible to perform creep tests in which the cell relaxes inside the micropipette for a certain time. The aspiration length of the cell, inside the micropipette chamber, is recorded during the experiment until the equilibrium is reached. The micropipette technique has been used by different authors in order to investigate the elastic and viscoelastic mechanical properties of chondrocyte subcomponents (Guilak et al., 2000; Ohashi, Hagiwara, Bader, & Knight, 2006) or to compare results obtained from different experimental methods (E. Darling, Zauscher, & Guilak, 2006).

3.2.3 Cytoindentation and Micromanipulation

Cytoindentation is a technique first developed for displacement-controlled indentation tests on single cells (Shin & Athanasiou, 1999). Over the years, it has been modified in order to perform creep indentation experiments on adherent cells (Koay, Shieh, & Athanasiou, 2003; Leipzig & Athanasiou, 2005). This technique is widely used to perform compression tests on chondrocytes, as they are anchorage-dependent cells that usually experience compressive forces in vivo (Koay et al., 2003). The experimental setup usually consists of a 5 μm diameter glass or tungsten flat probe that indents cells, which are attached to a glass substrate. The creep test is performed by applying a constant stress to the chondrocytes and measuring the obtained cell deformation. Different probe diameters are used, leading to a modified cytoindentation apparatus, also called the unconfined creep compression tool (Leipzig & Athanasiou, 2005; Shieh & Athanasiou, 2006; Ofek, Wiltz, & Athanasiou, 2009). While in cytoindentation the tip probe is smaller than the tested cell, in the modified apparatus the flat tip has a diameter bigger than the cell (e.g., about 50 μm) (Leipzig & Athanasiou, 2005; Shieh & Athanasiou, 2006). Similarly to the latter, micromanipulation is a technique used to evaluate the mechanical behaviour of a suspended chondrocyte by compressing the single cell between two parallel surfaces, such as the flat end of a glass probe and the bottom of a glass chamber containing cells immersed in a culture medium (B. V. Nguyen et al., 2009, 2010).

3.3 Mechanical role of chondrocyte and PCM subcomponents

Analysing the role of the subcomponents of the cell and the chondron in the mechanical response can elucidate more details on how the cell and its surrounding can react to external stimuli. The changes in physiological behaviour are usually linked to a concurrent change in the mechanical pathways involved in the mechanotransduction of external stimuli. For this reason, here are presented the main contributions of the subcomponents to the mechanical response of chondrocytes and chondrons.

3.3.1 Chondrocyte's subcomponents

Usually, cells are modelled as solid homogeneous materials in order to simplify their behaviour, thus losing the role of different subcomponents such as the nucleus, cytoskeleton and organelles. For this reason, some studies investigated this aspect, which highlighted important insights such as the fundamental structural role of the cytoskeleton in cells' behaviour (Trickey, Lee, & Guilak, 2000; Trickey, Vail, & Guilak, 2004). By comparing cells after a few hours (usually 2 h) and 2–3 days in culture, it was shown that the first ones were stiffer than the others. This can be due to the structural alterations of the cell's cytoskeleton, which occur leaving the cells in culture for a longer period (Florea et al., 2014; T. D. Nguyen & Gu, 2014; E. M. Darling et al., 2007). Since the cytoskeleton is composed of microfilaments, intermediate filaments and microtubules, several studies also investigated their contribution, by adding a specific disruptive agent for each cytoskeleton component, before the mechanical test. Different testing methods have been adopted, e.g., MPA, modified cytoindentation and micromanipulation (Ohashi et al., 2006; Ofek, Wiltz, & Athanasiou, 2009). Thanks to the unconfined compression testing method, achieved via modified cytoindentation, it was observed that each cytoskeletal component contributes differentially to the compressive properties of single chondrocytes. More precisely, actin microfilaments contribute to bulk cell compressive stiffness. Indeed, it was demonstrated that its disruption led to a decrease in the cell's compressive modulus (from 1.63 $\pm$ 0.31 kPa for a cell with a functional cytoskeleton to 1.01 $\pm$ 0.10 kPa for a cell without actin microfilaments). Instead, intermediate filaments play an important role in cellular compressibility and microtubules contribute to the incompressible nature of cells. Due to the disruption of the microtubules inside the cell, the Poisson's ratio changed, from a value of 0.49 for an intact cell to 0.36 for a chondrocyte without the microtubules (Ofek, Wiltz, & Athanasiou, 2009). Williantarra et al. showed that the substrate stiffness affected centriole positioning, cell morphology, actin architecture and primary cilium length in murine chondrocytes (Williantarra, Leung, Choi, Chhana, & McGlashan, 2022). Importantly, it has been shown that the depletion of primary cilia in murine tibial cartilage impacts the mechanical stiffness. In particular, the cartilage of these mice had lower instantaneous and equilibrium moduli (approximately half of those observed for wild-type cartilage) (Irianto, Ramaswamy,

Serra, & Knight, 2014). Moreover, the mechanical properties of the chondrocyte nucleus have been investigated. Highly significant differences were found between the properties of single chondrocytes and those of isolated nuclei (Guilak et al., 2000). MPA tests showed that the mechanical properties of chondrocytes' nuclei are different from those of the cytoplasm and they are stiffer and more viscous than intact cells. Regarding calcium channels, TRPV4-mediated Ca2+ signalling played a central role in the response of chondrocytes to low (physiological) levels of strain (3% and 8% of strain), while Piezo channels played a central role in the response of chondrocytes to high strain (traumatic) levels (18% of strain) (Du et al., 2020).

3.3.2 PCM and ECM subcomponents

Regarding the chondron, Wilusz et al. (Wilusz & Guilak, 2014) used different enzymes to digest specific GAGs and PGs (i.e., aggrecan, dermatan sulphate/chondroitin sulphate and hyaluronan) in cryosections of porcine cartilage in order to investigate their impact on the biomechanical behaviour of the ECM and PCM. They observed that, regardless of the digestive technique, only the ECM's elastic moduli were reduced. Elastase has been shown to degrade both PCM and ECM and thus could cause a decrease in their elastic moduli. However, the authors demonstrated that PCM was not as affected as ECM was thanks to its resistance to other enzymes during digestion.

As described earlier, the ECM and PCM are composed of different molecules, which contribute to their biochemical and mechanical properties. In the ECM, the main component is type II collagen, which makes up to 90–95% of the cartilage collagen. This type of collagen is mainly produced by the chondrocyte and is organised in complex scaffolds able to sustain the mechanical forces that the AC is usually subjected to. Two other important components of the ECM of the AC are type XI and type IX collagen. The former represents 3% of adult AC, while it forms up to 10% of fetal cartilage. This type of collagen is the first one to be synthesised by stem cells differentiating into a chondrocyte and it is usually found close to this cells' surfaces. This arrangement leads to the belief that type XI collagen plays a role as a mediator between the PCM and the chondrocyte by interacting with PGs present in the cartilage (Alcaide-Ruggiero, Molina-Hernández, Granados, & Domínguez, 2021). Type IX collagen on the other hand contributes to only 1–5% of the total collagen in adults and it is believed to stabilise the organisation of fibrils and proteoglycans thanks to its lateral association with both collagen type XI and type II. Furthermore, a reduction in the quantities of type IX collagen present in the cartilage is linked to different pathological states. It is believed that a reduction in the amount of this type of collagen could contribute to the development of osteoarthritis (Alcaide-Ruggiero et al., 2021). Another important type of collagen present in articular cartilage is type VI collagen. This type of collagen is present in most tissues of the human body but in articular cartilage, it can only be located in the PCM. The ability of this type of collagen to interact with many of the constituents of the ECM hints at its role in anchoring the chondrocyte to the PCM and

the spatial organisation of the ECM relative to that of the PCM (Alcaide-Ruggiero et al., 2021). Some studies have highlighted how a deficiency of type VI collagen leads to an accelerated development of OA, thus further reinforcing the link between the organisation of its network to the mechanotransduction processes of chondrocytes.

3.4 Experimental results

The chondrocytes considered for the experimental tests were primary cells that were isolated from human and animal cartilage. The main method used for cell harvesting appears to be the enzymatic digestion of cartilage with pronase (Guilak et al., 2000), collagenases (Florea et al., 2014, 2017; Koay et al., 2003; Leipzig & Athanasiou, 2005; Shieh & Athanasiou, 2006; Wozniak, Kawazoe, Tateishi, & Chen, 2009) or both enzymes (E. Darling et al., 2006; E. M. Darling et al., 2008; Jones et al., 1999; Guilak et al., 2000; Ohashi et al., 2006; B. V. Nguyen et al., 2010; Trickey et al., 2000; Bader, Ohashi, Knight, Lee, & Sato, 2002; Trickey et al., 2004; Trickey, Baaijens, Laursen, Alexopoulos, & Guilak, 2006). The incubation time of digestion ranged between 1 and 16 h at 37 °C.

Most reported tests were performed at room temperature keeping cells immersed in phosphate-buffered saline (PBS) in order to prevent sample dehydration.

3.4.1 Influence of site and depth

An important factor to be considered in the mechanical properties of chondrocytes and chondrons is the cartilage zone in which cells are embedded. Wilusz et al. (Wilusz et al., 2013) tested the region between 0.2 and 0.4 mm from the articular surface (which corresponds to the middle–upper deep zone) through AFM indentation. They produced 5 mm thick slices of cartilage samples from femoral condyles, sectioned perpendicular to the articular surface, by adopting a cryostat microtome, in order to evaluate the mechanical properties of the ECM and PCM in situ at different depths. Moreover, with reference to chondrocytes, many studies were conducted testing cells harvested from the surface, middle and deep zone of cartilage (E. Darling et al., 2006; Shieh & Athanasiou, 2006; Guilak, Ratcliffe, & Mow, 1995). Indeed, these authors agreed that superficial cells have significantly higher moduli and apparent viscosity than middle/deep ones do. This variation was supposed to be influenced by different loading histories experienced by cells in each zone (Shieh & Athanasiou, 2006). Moreover, it was shown that cells differ not only in mechanical behaviour but also in size, volume and shape depending on the zone. A summary of chondrocytes' mechanical parameters obtained within the analysed studies is reported in table 1.

Mechanical Test	Origin	Reference	Cartilage Depth	Material Model	Parameters
AFM	Human	(E. M. Darling et al., 2008)	Full thickness	Linear elastic	$E = 1.4 \pm 1.1$
				Viscoelastic	$E_0 = 0.914 \pm 0.967$ $E_\infty = 0.45 \pm 0.44$ $\mu = 4.5 \pm 3.74$

AFM	Human	(T. D. Nguyen & Gu, 2014)	N/A	Viscohyperelastic	$C_1 = 0.669 \pm 0.365$ $D_1 = 4.06 \pm 2.4(\times 10^{-3})$ $g_1 = 0.6 \pm 0.14$ $k_1 = 99.76 \pm 0.08(\times 10^{-2})$ $\tau_1 = 0.082 \pm 0.002$
AFM	Animal	(E. Darling et al., 2006)	Superficial	Linear elastic	$E = 1.27 \pm 0.61$
				Viscoelastic	$E_0 = 0.55 \pm 0.23$ $E_\infty = 0.31 \pm 0.15$ $\mu = 1.15 \pm 0.66$
			Middle/deep	Linear elastic	$E = 0.61 \pm 0.34$
				Viscoelastic	$E_0 = 0.29 \pm 0.14$ $E_\infty = 0.17 \pm 0.09$ $\mu = 0.61 \pm 0.69$
AFM	Animal	(Florea et al., 2014)	Full thickness	Linear Elastic	$E = 10 \pm 4.1$
AFM	Animal	(Florea et al., 2017)	Full thickness	Porohyperelastic	$E = 23.9$ $k = 0.08 \times 10^{-16}$
				Viscohyperelastic	$E = 11.9$ $g_1 = 0.55$ $\tau_1 = 6$
				Poroviscohyperelastic	$E = 10.9$ $k = 0.66 \times 10^{-16}$ $g_1 = 0.55$ $\tau_1 = 15$
MPA	Human	(Jones et al., 1999)	Full thickness	Linear elastic	$E = 0.65 \pm 0.63$
MPA	Human	(Trickey et al., 2000)	Full thickness	Viscoelastic	$E_0 = 0.41 \pm 0.17$ $E_\infty = 0.24 \pm 0.11$ $\mu = 3.0 \pm 1.80$
MPA	Human	(Trickey et al., 2004)	N/A	Viscoelastic	$E_0 = 0.45 \pm 0.2$ $E_\infty = 0.2 \pm 0.1$ $\mu = 7.8 \pm 8$
MPA	Animal	(Guilak et al., 2000)	N/A	Viscoelastic	$E_0 = 0.43 \pm 0.07$ $E_\infty = 0.18 \pm 0.05$ $\mu = 2.5 \pm 1.80$
MPA	Animal	(E. Darling et al., 2006)	Middle/deep	Viscoelastic	$E_0 = 0.45 \pm 0.14$ $E_\infty = 0.14 \pm 0.05$ $\mu = 2.57 \pm 1.83$
MPA	Animal	(Ohashi et al., 2006)	Full thickness	Linear elastic	$E = 0.97 \pm 0.45$
Cytoindentation	Animal	(Koay et al., 2003)	Full thickness	Linear elastic	$E = 1.10 \pm 0.48$
				Viscoelastic	$E_0 = 8.0 \pm 4.41$ $E_\infty = 1.09 \pm 0.54$ $\mu = 1.50 \pm 0.92$
Cytoindentation	Animal	(Leipzig & Athanasiou, 2005)	Middle/deep	Linear elastic	$E = 2.55 \pm 0.85$
				Viscoelastic	$E_0 = 2.47 \pm 0.85$ $E_\infty = 1.48 \pm 0.35$ $\mu = 1.92 \pm 1.80$
				Biphasic	$H_A = 2.58 \pm 0.87$ $k = 2.57 \times 10^{-12}$
			Superficial		$E_0 = 1.20 \pm 1.00$ $E_\infty = 0.80 \pm 0.55$ $\mu = 3.75 \pm 9.46$

Cytoindentation	Animal	(Shieh & Athanasiou, 2006)	Middle/deep	Viscoelastic	$E_0 = 0.78 \pm 0.38$ $E_\infty = 0.64 \pm 0.31$ $\mu = 3.18 \pm 7.33$
Micromanipulation	Animal	(B. V. Nguyen et al., 2010)	Full thickness	Non-linear elastic	$E = 14 \pm 10$
				Non-linear Viscoelastic	$E_0 = 21 \pm 3$ $E_\infty = 9.3 \pm 0.8$ $\mu = 2.8 \pm 0.5$

Table 1: The studies were divided according to the mechanical test used. For each analysed study, the following information is reported: origin which can be human or animal, reference, cartilage depth, material models and mechanical parameters. Linear elastic model: E is the elastic or Young's modulus (kPa); viscoelastic model: E_0 is the instantaneous Young's modulus (kPa), $E\infty$ is the equilibrium Young's modulus (kPa) and μ is the apparent viscosity ($kPa \cdot s$); porohyperelastic model, viscohyperelastic model and poroviscohyperelastic model: E is the equilibrium elastic modulus (kPa), C_1 (kPa) and D_1 (kPa^{-1}) are the temperature-dependent material constants, g_1 is the Prony shear relaxation (-), k_1 is the Prony bulk relaxation (-), τ_1 is the relaxation time parameter (s), k is the hydraulic permeability ($m^4/N \cdot s$) and H_A is the aggregate modulus (kPa). N/A = not available. Parameter values are reported as mean ± SD, except for those reported by (B. V. Nguyen et al., 2010) (only values attained via an optimisation procedure).

Differently from the chondrocyte, the chondron does not exhibit significant differences between sites and depths in terms of both mechanical response and mechanical properties (Alexopoulos, Haider, Vail, & Guilak, 2003; E. M. Darling, Wilusz, Bolognesi, Zauscher, & Guilak, 2010; Guilak, Alexopoulos, Haider, Ting-Beall, & Setton, 2005) as reported in table 2. On the contrary, the morphology and orientation of the chondron may change significantly depending on depth, as reported by Youn et al. (Youn, Choi, Cao, Setton, & Guilak, 2006) who investigated the chondron structure along the whole thickness of the AC (from the surface to the deep cartilage) of a porcine knee. Chondrons located at the superficial layer presented a discoidal flattened shape oriented parallelly to the surface of the cartilage, while chondrons located at an intermediate level were more rounded and did not exhibit a preferred orientation. Lastly, chondrons located at a deeper level revealed groups in which a single PCM was able to encapsulate multiple chondrocytes creating an oval-shaped structure oriented perpendicularly to the cartilage surface (Youn et al., 2006).

Mechanical Test	**Origin**	**Reference**	**Cartilage Depth**	**Material Model**	**Parameters**
AFM	(Allen & Mao, 2004)	Animal	Full thickness	Linear elastic	$E = 265 \pm 53$
AFM	(McLeod et al., 2013)[1]	Animal	Superficial	Linear elastic	$E = 54.9 \pm 4.5$
			Middle		$E = 49.4 \pm 4.5$
			Deep		$E = 50.6 \pm 4.5$
AFM	(E. M. Darling et al., 2010)	Human	Full thickness	Linear elastic	$E = 306 \pm 133$
		Animal			$E = 81 \pm 19$
		Animal			$E = 197 \pm 92$
AFM	(Wilusz et al., 2013)	Human	Full thickness	Linear elastic	$E = 137 \pm 22$

AFM	(Ng et al., 2007)[2]	Animal	Cultured	Linear elastic	$E = 4.14 \pm 0.4$
MPA	(Alexopoulos et al., 2003)	Human	Superficial	Linear elastic	$E^3 = 68.9 \pm 18.9$
			Middle/deep		$E^3 = 62.0 \pm 30.5$
			Full thickness		$E^3 = 66.5 \pm 23.3$
					$E^4 = 43.1 \pm 17.9$
MPA	(Alexopoulos, Williams, et al., 2005)	Human	Superficial	Biphasic	$E = 39.7 \pm 13.9$
					$k = 4.71 \pm 4.18$
			Middle/deep		$E = 36.8 \pm 20.6$
					$k = 3.69 \pm 3.4$
MPA	(Guilak et al., 2005)	Animal	Superficial	Linear elastic	$E^3 = 24.0 \pm 10.9$
					$E^5 = 25.1 \pm 11.5$
					$E^4 = 10.8 \pm 4.3$
			Middle/deep		$E^3 = 23.2 \pm 7.1$
					$E^5 = 23.6 \pm 7.3$
					$E^4 = 12.1 \pm 3.9$
Cytomanipulation	(B. V. Nguyen et al., 2010)	Animal	Full thickness	Linear elastic	$E = 19 \pm 2$
				Viscoelastic	$E_0 = 27 \pm 4$
					$E_\infty = 12 \pm 1$
					$\mu = 3.4 \pm 0.6$

Table 2: The studies were divided according to the mechanical test used. For each analysed study, the following information is reported: origin which can be human or animal, reference, cartilage depth, material models and mechanical parameters. Linear elastic model: E is the elastic or Young's modulus (kPa); viscoelastic model: E_0 is the instantaneous Young's modulus (kPa), $E\infty$ is the equilibrium Young's modulus (kPa) and μ is the apparent viscosity ($kPa \cdot s$); biphasic model: E is the equilibrium elastic modulus (kPa) and k is the hydraulic permeability ($m^4/N \cdot s$). Parameter values are reported as mean ± SD. All AFM tests were performed using AFM stiffness mapping and thus without the extraction of the chondron from the cartilage samples except for in (Ng et al., 2007). All MPA tests were performed on mechanically isolated chondrons. For the cytomanipulation test Chondrons were enzymatically extracted and tested at 0.3 deformation (linear elastic data) and 0.5 deformation (viscoelastic data). [1] The data reported in the work show slight orthogonal anisotropy. [2] Data of a cultured chondrocyte in vitro after 28 days. [3] Layered model used. [4] Half-space model. [5] Shell model.

3.4.2 Difference between human and animal cartilage

Chondrocytes were isolated from cartilage harvested from different sites, such as knees and hips (E. M. Darling et al., 2008; Jones et al., 1999; Trickey et al., 2000, 2004, 2006), for human cells (donors aged between 20–86 years), while animal cells were harvested from femoral condyles and distal metatarsal joints from different sources, such as rat (Freeman, Natarajan, Kimura, & Andriacchi, 1994), dog (Guilak et al., 1995), pig (E. Darling et al., 2006; Guilak et al., 2000) and cattle, which included cows, calves and steers (Florea et al., 2014, 2017; Ohashi et al., 2006; Koay et al., 2003; Leipzig & Athanasiou, 2005; Shieh & Athanasiou, 2006; Ofek, Wiltz, & Athanasiou, 2009; B. V. Nguyen et al., 2009, 2010; Wozniak et al., 2009; Bader et al., 2002; Han, Madden, Abusara, & Herzog, 2012; Dowling et al., 2012; Chahine et al., 2013). Comparing the

elastic modulus, E, of human and animal chondrocytes, it was observed that human chondrocytes range between 0.65 and 1.4 kPa (E. M. Darling et al., 2008; Jones et al., 1999), while greater variability was observed among different species (E ranging between 0.97 and 23.9 kPa (Florea et al., 2014; E. Darling et al., 2006; Florea et al., 2017; Ohashi et al., 2006; Koay et al., 2003; Leipzig & Athanasiou, 2005), as reported in table 1), but always within the same order of magnitude. Moreover, both human and animal chondrocytes were obtained from various joints; this aspect represents another key variable in the evaluation of biomechanical properties as it is likely that chondrocytes of different joints might have different biomechanical properties.

As observed in table 2, the mechanical properties of chondrons from different animal species are significantly different as well. Darling et al. (E. M. Darling et al., 2010) demonstrated that the ratios between the mechanical properties (namely their Young's Moduli) of the PCM and the ECM are constant and in the range of 0.34–0.37 for all species included in the study (human, rats and pigs). However, no details were provided regarding this ratio. It is unclear if it was obtained by averaging the mechanical properties of the ECM at different depths or if it was limited to generic AFM indentation tests.

3.5 Theoretical models

Chondrocytes' mechanical properties may differ also depending on the adopted model used to describe cell behaviour and to fit experimental data obtained from a specific experiment. The common approaches used to describe chondrocytes' material behaviour are the elastic or the viscoelastic one, as reported in many studies (e.g., (Guilak & Mow, 2000; E. Darling et al., 2006; Koay et al., 2003) to cite a few). Viscoelasticity is also able to capture the viscoelastic effects that usually emerge during the creep and stress–relaxation behaviours of a cell. When a cell is compressed until a large deformation occurs, a non-linear elastic model appears to be more suitable. For this reason, many studies include hyperelastic formulations (T. D. Nguyen & Gu, 2014; Florea et al., 2017; B. V. Nguyen et al., 2010), usually adopting a neo-Hookean material model. A biphasic formulation was also introduced to consider the contribution of two physical mechanisms: the intracellular fluid flow inside the cell, representing the cytoplasm, and the solid components, such as the cytoskeleton and organelles (Florea et al., 2017; Leipzig & Athanasiou, 2005). Some studies used models of increasing complexity, by combining two or more of the previous material models, in order to better describe the real behaviour of cells. These models are the viscohyperelastic, porohyperelastic and poroviscohyperelastic ones (B. V. Nguyen et al., 2010). However, it has been reported that similar values have been obtained for the cell modulus from the elastic, viscoelastic and biphasic models (E. Darling et al., 2006; E. M. Darling et al., 2008; Koay et al., 2003; Leipzig & Athanasiou, 2005; Shieh & Athanasiou, 2006). As it is possible to observe in table 1 and from the literature (B. V. Nguyen et al., 2010), the

Young's modulus obtained with a model of increasing complexity falls in the same range (0.62–27 kPa) of those obtained using simpler mechanical characterisation techniques (Guilak, 2000; E. Darling et al., 2006; Jones et al., 1999; Koay et al., 2003; Leipzig & Athanasiou, 2005; Shieh & Athanasiou, 2006; Ofek, Wiltz, & Athanasiou, 2009; Trickey et al., 2000). However, with a model of increasing complexity, such as the viscoelastic, hyperelastic or biphasic models, it is possible to describe not only the linear elastic behaviour of the cell but also the non-linear (hyperelastic), time-dependent response (viscoelastic) and the contribution of the fluid and solid phase inside the chondrocytes itself. In many material models, chondrocyte behaviour is assumed to be incompressible (Poisson's ratio, $\nu = 0.5$ (E. M. Darling et al., 2008; Guilak et al., 2000; Koay et al., 2003; Leipzig & Athanasiou, 2005; B. V. Nguyen et al., 2010)), even if it has been demonstrated that cell incompressibility is not valid under direct compression (e.g., during modified cytoindentation tests (Shieh & Athanasiou, 2006)).

Several theoretical models have been used to fit the experimental data in order to determine chondrocytes' properties. Force–displacement data obtained with the AFM technique are usually fitted with the Hertz contact model (Florea et al., 2014; E. Darling et al., 2006; Wozniak et al., 2009) or with a thin-layer Hertz model (E. Darling et al., 2006; E. M. Darling et al., 2007). The first one describes the interaction between two spheres, the cell and the cantilever tip; the second one represents a hard sphere (the cantilever tip) indenting a flat deformable substrate representing the cell. Experimental data gained with MPA tests are usually fitted with Theret's model (Theret, Levesque, Sato, Nerem, & Wheeler, 1988), to obtain the elastic cell parameter (Jones et al., 1999; Ohashi et al., 2006; Bader et al., 2002), or with the theoretical model formulated by Sato (Sato, Theret, Wheeler, Ohshima, & Nerem, 1990), which considers time dependence (E. Darling et al., 2006; Trickey et al., 2000, 2004; Guilak, 2000). In addition, the standard linear solid model was employed to determine the viscoelastic properties of chondrocytes during relaxation tests, performed with AFM (E. Darling et al., 2006; E. M. Darling et al., 2008) or micromanipulation (B. V. Nguyen et al., 2010) and during creep tests, conducted with MPA (E. Darling et al., 2006; Trickey et al., 2000; Guilak, 2000) or cytoindentation (Koay et al., 2003; Leipzig & Athanasiou, 2005; Shieh & Athanasiou, 2006). All these analytical models have the advantage of being easily applicable. Indeed, they rely on the linearity of the chondrocytes' mechanical responses as they consider cells formed only by a single solid component. To evaluate the parameters of a cell which shows viscohyperelastic behaviour, a model has been developed named the standard neo-Hookean solid model (SnHS), proposed by Zhou (Zhou, Lim, & Quek, 2005). This model was later modified (mSnHS) in order to capture the strain rate-dependent mechanical behaviour of both living and fixed cells (T. D. Nguyen & Gu, 2014).

3.6 Factors that can influence experimental results

3.6.1 Influence of mechanical test

The first factor to be considered is the different testing configurations, such as AFM, cytoindentation, micromanipulation and MPA. AFM and cytoindentation techniques are performed on chondrocytes attached to a substrate; in the former case, cells are usually seeded on poly-L-lysine coated slides (E. Darling et al., 2006; T. D. Nguyen & Gu, 2014), while in the latter, chondrocytes are usually attached to a glass slide (Koay et al., 2003; Shieh & Athanasiou, 2006; Ofek, Wiltz, & Athanasiou, 2009). MPA and micromanipulation procedures are used to assess the mechanical properties of cells in suspension (E. Darling et al., 2006; B. V. Nguyen et al., 2009, 2010). The elastic and viscoelastic properties could be obtained on suspended cells (E. Darling et al., 2006; Jones et al., 1999; Trickey et al., 2000, 2004, 2006), while the adhesion force can be investigated at the single-cell level on adherent cells (Hogan, Babataheri, Hwang, Barakat, & Husson, 2015).

Experimental tests can lead to different mechanical parameters depending on the adoption of suspended or adherent cells. Some studies compared AFM and MPA tests on chondrocytes and stated that no differences were found (E. Darling et al., 2006). On the contrary, other studies asserted that some differences were found when cells were tested in suspension or attached to a substrate. For example, micromanipulation performed on suspended cells (B. V. Nguyen et al., 2009, 2010), and modified cytoindentation tests performed on adherent chondrocytes (Leipzig & Athanasiou, 2005; Shieh & Athanasiou, 2006), lead to different mechanical parameters, even if both procedures compress the entire cell. Further differences emerged comparing several literature studies: MPA (Trickey et al., 2000), AFM (E. Darling et al., 2006) and cytoindentation (Koay et al., 2003) deform only a portion of the cell's membrane, while micromanipulation (B. V. Nguyen et al., 2009, 2010) and modified cytoindentation (Leipzig & Athanasiou, 2005) compress the whole cell into a large nominal strain. Moreover, MPA and AFM usually give information about local mechanical properties, e.g., the cell membrane, while micromanipulation reflects the mechanical properties of whole cells and of their subcomponents, such as the cytoskeleton and nucleus (B. V. Nguyen et al., 2010). As previously reported, observing table 1, the mechanical parameters of chondrocytes are different but in the same order of magnitude. This could be attributed to different testing methods but also to the inhomogeneity of the cell structure; indeed, the nucleus contributes considerably to unconfined compression, while it plays a smaller role in the tensile response to MPA (Leipzig & Athanasiou, 2005). Differences induced by the test setup have also been found in two studies which adopted cells harvested from the same species and joint; cytoindentation (Koay et al., 2003) and modified cytoindentation (Shieh & Athanasiou, 2006) were performed with the same device, but with slightly different procedures since the first one is an indentation procedure, while the second one is an unconfined compression. Comparing the results obtained via these two testing

methods, it was observed that the instantaneous Young's modulus obtained with the cytoindentation technique was about eight times higher than that obtained with the modified cytoindentation one.

Chondrocytes' mechanical parameters can also vary due to different setups while using the same experimental approach. In AFM experiments, different probe sizes (micrometers or nanometers) and tip shapes, e.g., spherical or pyramidal (Florea et al., 2014; E. Darling et al., 2006; E. M. Darling et al., 2008; T. D. Nguyen & Gu, 2014) are available. By varying the tip radius, authors found consistent changes in the Young's modulus; more precisely, with a sharp nanosized tip the elastic modulus resulted to be higher than that obtained with a larger spherical probe (Rico et al., 2005; Vargas-Pinto, Gong, Vahabikashi, & Johnson, 2013). This could be due to the fact that using a sharp tip to indent a cell, can cause different cytoskeleton rearrangements under the cell membrane or encounter differently dense areas of this structure (Florea et al., 2014), and second, the chondrocyte volume indented and investigated via the AFM tip is different (B. V. Nguyen et al., 2010). Moreover, the hydraulic permeability, k, is slightly different between experiments using a nanosized and those using a microsized tip probe (T. D. Nguyen & Gu, 2014; Florea et al., 2017).

Chondrons have been mainly tested using AFM and MPA techniques. The AFM indentation tests may provide information about the chondron when it is still embedded in the surrounding ECM using a stiffness mapping method. On the other hand, this approach lacks lateral resolution and thus, the obtained measures could be affected by the presence of the TM and ECM (Wilusz et al., 2013; McLeod et al., 2013; Ng et al., 2007). A possible solution was suggested in the literature in the use of a conservative approach when identifying the PCM which reduced the sample area for parameter estimation (E. M. Darling et al., 2010). Another problem with the AFM is the choice of the right indenter size to use; a nanometric indenter can be more precise in terms of area investigation but tends to cause the artificial stiffening of the sample if compared to micrometric indenters (E. M. Darling et al., 2010). AFM indentation can also be used to test cells adherent to a substrate as well as those captured in microwells (Ng et al., 2007). The MPA technique applies a tensile stress to the surface of the sample and usually requires cells to be suspended in a medium. This method can be used to test viscoelastic properties as well as the elastic response of the specimen. The studies of Alexopoulos (Alexopoulos et al., 2003) and Guilak (Guilak et al., 2005) showed that the use of a half-space model might lead to an underestimation of the mechanical parameters when compared to the use of a layered or shell model due to the fact that the half-space model does not take the geometry and compressibility of the chondron into account. Finally, it is worth mentioning that although these authors stated that the experimental data revealed a possibly viscoelastic response, only a few studies tried to characterise this type of response with a biphasic (Alexopoulos, Williams, et al., 2005) or viscoelastic (B. V. Nguyen et al., 2010) model.

3.6.2 Sample Harvesting Techniques and Culturing

Regarding chondrocytes, the harvesting technique is not considered a factor that can influence their mechanical properties, even if it could have an impact on the cell biomechanical parameters due to possible cell damage. Moreover, the harvesting method adopted in all the testing procedures reported in the studies analysed in this review is only the enzymatic one (Florea et al., 2014; E. Darling et al., 2006; E. M. Darling et al., 2008; Florea et al., 2017; Jones et al., 1999; Guilak et al., 2000; Ohashi et al., 2006; Koay et al., 2003; Leipzig & Athanasiou, 2005; Shieh & Athanasiou, 2006; B. V. Nguyen et al., 2010; Wozniak et al., 2009; Trickey et al., 2000; Bader et al., 2002; Trickey et al., 2004, 2006). After the harvesting procedure, chondrocytes are cultured in different ways depending on the testing method adopted to assess their mechanical properties. They are cultivated in alginate beads if cells are tested with the MPA technique (Jones et al., 1999; Guilak et al., 2000; Trickey et al., 2000, 2004) or attached to a substrate if they are tested with the AFM (Florea et al., 2014; E. M. Darling et al., 2008; T. D. Nguyen & Gu, 2014; Florea et al., 2017) or cytoindentation procedure (Koay et al., 2003). In the first case, chondrocytes are suspended in the beads in culture media (DMEM (Jones et al., 1999) or Ham's F-12 medium (Guilak et al., 2000) with FBS and penicillin/streptomycin) until tested. Immediately prior to testing, the alginate beads are dissolved in sodium chloride and sodium citrate to release the chondrocytes which are then suspended in Hank's balanced salt solution (Jones et al., 1999; Trickey et al., 2000, 2004) or in Dulbecco's phosphate-buffered solution (Guilak et al., 2000), containing bovine serum albumin and sodium chloride/sodium citrate solution (Jones et al., 1999; Guilak et al., 2000; Trickey et al., 2000, 2004). In the second case, cells are suspended in culture media (composed of DMEM, penicillin, streptomycin and FBS) and then seeded on poly-L-ly-sine-coated polystyrene plates (Florea et al., 2014; E. Darling et al., 2006; T. D. Nguyen & Gu, 2014; Florea et al., 2017). No studies investigated the influence of different culture methods on biomechanical parameters as well as different testing methods. Therefore, specific studies comparing different culturing and storage methods are needed in order to better clarify this point and to identify the best culture system for mechanotransduction tests. Chondrons showed significantly different mechanical responses depending on the harvesting technique used. Two techniques are typically adopted to isolate chondrons: enzymatic digestion of the territorial matrix (using dispase and collagenase) and a mechanical homogenisation process. The former leads to relatively abundant yields, while the mechanical extraction process reduces the number of viable chondrons (Knight et al., 2001). Mechanical tests of isolated chondrocytes (ICs), mechanically extracted chondrons (MCs) and enzymatically extracted chondrons (ECs), all from the middle/deep layers of canine AC, led to significantly different mechanical responses (Knight et al., 2001)). The MCs resulted in a stiffer global response compared to that of the ICs and ECs. Indeed, MCs resulted in being stiffer compared to the ICs and ECs embedded in agarose gel via compression experiments (Knight et al., 2001). This difference appeared to become less evident over time, as incubating the samples for

up to 7 days led to the partial reconstruction of the PCM around the ICs and MCs and thus to a more similar response between the three groups. This observation supports the hypothesis that the enzymatical extraction process leads to a degraded/damaged PCM in ECs. This point was further confirmed via osmotic challenge tests performed on ICs, ECs, and MCs (Hing et al., 2002). When exposed to a hypertonic solution, the ICs and ECs shrank more than the MCs did and the difference in swelling was reduced by culturing the samples for up to one week. These results together with the concept that the PCM could be involved in protecting the chondrocyte from osmotic changes support the hypothesis that enzymatic isolation tends to isolate chondrons with a damaged PCM compared to the MCs. Therefore, the ECs exhibit a behaviour resembling that of ICs, which completely lack the PCM structure (Hing et al., 2002; Knight et al., 2001), and this is supported by several published studies aimed at comparing the physiological or mechanical behaviour of ICs and ECs (B. V. Nguyen et al., 2010; Kelly, Wang, Mauck, Ateshian, & Hung, 2004). Chondrons are usually cultured using different methods: alginate beads (Ng et al., 2007), agarose gel (Kelly et al., 2004) or assembly in pellets (Graff, Kelley, & Lee, 2003). It should be noted that culturing chondrons tends to override the impact of the isolation method used (mechanical vs. enzymatic) as the chondrons are able to synthesize a new complete PCM in vitro when the proper nutrients and growth factors are added to the culture media. Although the differences between ECs and MCs tend to disappear after 3 weeks in culture (Graff et al., 2003), the cultured chondrons do not stop the development of a functional and complete PCM even after 28 days of culture (Ng et al., 2007). Thus, the ability of a chondrocyte to build a proper PCM could be exploited to solve some of the problems related to the extraction method used. It is worth mentioning that it is currently unknown how long it takes for ECs and ICs to form a fully functional PCM in vitro, and some studies (Ng et al., 2007; Graff et al., 2003) reported a final PCM stiffness lower than the one of freshly mechanically extracted chondrons, thus raising doubts about this possibility. In conclusion, a less functional PCM in ECs makes them behave more similarly to ICs in mechanical tests. Conversely, MCs tend to better preserve the PCM, thus leading to a stiffer chondron which behaves differently from ECs and ICs.

3.6.3 Sample storage

Although several studies did not report the storage method used, when reported, different storage strategies were observed for chondrons depending on the type of experiment performed. When dealing with AFM stiffness mapping, the cartilage samples were frozen at -20 °C, wrapped in phosphate-buffered saline (PBS) gauzes and then the cartilage samples were cut to obtain slices for AFM stiffness mapping (Wilusz et al., 2013; Wilusz & Guilak, 2014; E. Darling et al., 2006; McLeod et al., 2013). Other less common procedures were the use of fresh sample slices (Allen & Mao, 2004), and fixation with 4% para-formaldehyde followed by decalcification in 10% EDTA for 21 days (Chery et al., 2020). When performing MPA tests, the chondrons were extracted

from the cartilage and usually stored in a glass container (such as a petri dish), covered with PBS for immediate tests (Guilak et al., 2005).

3.6.4 Mechanical changes in OA cartilage

Over the years, both non-OA and OA chondrocytes' mechanical properties were investigated, leading to contrasting results, as is possible to appreciate from data reported in the literature and in table 3. Some studies reported that chondrocytes' properties are nearly identical for cells isolated from healthy and OA cartilage (Jones et al., 1999; Trickey et al., 2006). In 2000, Trickey et al. (Trickey et al., 2000) showed that OA cells were stiffer (the elastic modulus of OA chondrocytes is 1.5 times higher than that of healthy ones) and more viscous than the healthy ones (OA cells have a viscosity, which is about double the value of that reported for healthy cells), while in 2004, they reported that OA chondrocytes seemed to have a lower elastic modulus and viscosity than the healthy ones did (Trickey et al., 2004). It is still not established if these contrasting and different results could be related to the pathological state or to the different experimental conditions (e.g., sample storage, different isolation methods and/or conditions of culture).

Mechanical Test	**Origin**	**Reference**	**Cartilage Depth**	**Material Model**	**Parameters**
MPA	Human	(Jones et al., 1999)	Full thickness	Linear elastic	$E = 0.67 \pm 0.86$
MPA	Human	(Trickey et al., 2000)	Full thickness	Viscoelastic	$E_0 = 0.63 \pm 0.51$ $E_\infty = 0.33 \pm 0.23$ $\mu = 5.8 \pm 6.5$
MPA	Human	(Trickey et al., 2004)	N/A	Viscoelastic	$E_0 = 0.52 \pm 0.25$ $E_\infty = 0.25 \pm 0.13$ $\mu = 4.8 \pm 5$

Table 3: For each analysed study, the following information is reported: origin which can be human or animal, reference, cartilage depth, material models and mechanical parameters. Linear elastic model: E is the elastic or Young's modulus (kPa); viscoelastic model: E_0 is the instantaneous Young's modulus (kPa), E_∞ is the equilibrium Young's modulus (kPa) and μ is the apparent viscosity ($kPa \cdot s$). N/A = not available. Parameter values are reported as mean ± SD.

Hsieh et al. supported the evidence that OA chondrocytes are less stiff than healthy ones. They determined cell stiffness through AFM indentation and found that OA chondrocyte stiffness was 0.0347 ± 0.0005 N/m, while that of healthy ones was 0.09620 ± 0.009 (which was about three times higher with respect to the OA ones) (Hsieh et al., 2008). Interestingly, porcine chondrocytes stimulated with IL1-alpha display an increase in pPIEZO1 expression, which causes an increase in Ca2+ levels in the cells and attenuates the dynamics of the F-actin cytoskeleton (decreasing the mechanical stiffness of the cell), leading to an increase in the mechanosensitivity of chondrocytes to mechanical loading (W. Lee et al., 2021; Zhuang, Ren, Zhang, Jiang, & Zhou, 2023). More precisely, the decrease in the chondrocyte's stiffness resulted in increased cellular

deformation in response to mechanical loading (W. Lee et al., 2021). Interestingly, Young et al. investigated the role of Piezo channels in OA mice demonstrating that the deletion of both genes does not impact normal joint development and has limited effects on OA progression (Young & Kobayashi, 2023).

3.6.5 Changes at the chondron scale

Chondrons' mechanical properties were demonstrated to be affected by OA. As can be observed from table 4, the Young's modulus of an OA chondron is significantly lower than that of a healthy one in all tests performed. In general, OA is responsible for a loss of the elastic modulus of the PCM of about 30–50% in an OA AC (Wilusz et al., 2013; Alexopoulos et al., 2003; Alexopoulos, Williams, et al., 2005). In the early stages of OA, the importance of the mechanical properties at the chondron level is further reinforced by a finite element study by Khoshgoftar et al. (Khoshgoftar, Torzilli, & Maher, 2018). They observed that the strain fields can be changed significantly around the chondrocyte within the chondron by changing only the mechanical parameters of the PCM and keeping the remaining tissue unaltered.

Mechanical Test	Origin	Reference	Cartilage Depth	Material Model	Parameters
AFM	Human	(Wilusz et al., 2013)	Full thickness	Linear elastic	$E = 96 \pm 16$
MPA	Human	(Alexopoulos et al., 2003)	Superficial	Linear elastic	$E^1 = 29.1 \pm 19.6$
			Middle/deep		$E^1 = 43.9 \pm 23.0$
			Full thickness		$E^2 = 41.8 \pm 21.3$ $E^3 = 33.1 \pm 22.9$
MPA	Human	(Alexopoulos, Williams, et al., 2005)	Superficial	Biphasic	$E = 20.8 \pm 19.5$ $k = 10.46 \pm 6.96$
			Middle/deep		$E = 24.4 \pm 12.7$ $k = 9.91 \pm 11.3$

Table 4: The studies were divided according to the mechanical test used. For each analysed study, the following information is reported: origin which can be human or animal, reference, cartilage depth, material models and mechanical parameters. Linear elastic model: E is the elastic or Young's modulus (kPa); biphasic model: E is the equilibrium elastic modulus (kPa) and k is the hydraulic permeability ($m^4/N \cdot s$). Parameter values are reported as mean ± SD. [1] Layered model used. [2] Shell model. [3] Half-space model.

As explained earlier, Wilusz et al. [27] observed that some differences can be observed between chondrons located in the lateral and medial condyle of about 30%. In the same study, the authors showed that the onset of OA causes a reduction in the stiffness of chondrons' PCM located in the medial condyle which is not present for the PCM of chondrons in the lateral condyle. According to their findings, the loss in mechanical properties makes the distinction between the PCM of medial and lateral condyle not statistically significant (Wilusz et al., 2013). Alexopoulos et al. used different models (elastic layered half-space model and linear biphasic model) to characterise the material behaviour of chondrons (Alexopoulos, Setton, & Guilak, 2005). Similarly, from what was

seen for healthy chondrons, the authors stated that the half-space model underestimates the value of the elastic modulus (Alexopoulos et al., 2003), while they claimed that the biphasic model is an overall better representation of chondron behaviour as the latter takes into account the compressibility and finite geometry of the chondron. Furthermore, this second approach shows an increase in the chondrons' permeability together with the expected decrease in stiffness (Alexopoulos, Williams, et al., 2005). Precious insights could be collected also from computational models reported in the literature. Most of the studies reinforced the hypothesis that the PCM is a fundamental structure in mechanosensing and thus exerts a key role in the mechanotransduction of external stimuli (Guilak & Mow, 2000; Khoshgoftar et al., 2018; Alexopoulos, Setton, & Guilak, 2005). Alexopoulos et al. and Khoshgoftar et al. pointed out an increase in the local deformation of the cell due to the mechanical changes in the OA PCM, while Guilak et al. stated that it was reduced in favour of increased applied stress (Guilak & Mow, 2000; Khoshgoftar et al., 2018; Alexopoulos, Setton, & Guilak, 2005). Julkunen et al. tried to develop a complex model of cartilage tissue using a hierarchical approach accounting for both the macroscopic and microscopic structure as well as the differences that can be found at different depths (Julkunen, Wilson, Jurvelin, & Korhonen, 2009). The model was not able to reproduce the same results obtained from experimental analysis but pointed out the lack of a full description of the material and methods reported in experimental studies (Julkunen et al., 2009).

4 FE models of the cell

As explained in previous chapters, the mechanical response of the cell to external stimuli is the product of a very complex and dynamic set of properties, functions and components. Moreover, the scale in which cells act both from a spatial and a physical point of view, makes the investigation of their behaviour the more difficult to clearly understand and define.

In this regard, Finite Element Models (FEM) are widely recognized as a very useful tool in the hand of researchers. Using FE models it is possible to represent a cell with an arbitrary level of simplification according to the needs and goals of each model. Some models may be fairly simple if the objective is to capture the global response to external forces(Gladilin et al., 2007) or they can be discretized to represent most of the internal components when the goal is to describe the internal behaviour of this complex apparatus(Banerjee et al., 2022).

Since cells exist at such a small scale, the methods by which their mechanical behaviour is tested have to be very complex and ingenious. Even though the last decades provided researchers with innovative and accurate systems to test the main mechanical aspects of cells there are still aspects that are beyond reach such as the ability to capture the singular contribution of certain subcomponents to the global or local mechanical response. Once again, FE models can provide insights and explanations for such aspects(Barreto, Clausen, Perrault, Fletcher, & Lacroix, 2013; L. Wang, Wang, Xu, Chen, et al., 2019).

Although an all-comprehensive model seems unattainable with current technologies, some models have been shown to be able to reliably reproduce some of the key aspects of cells' behaviour. Some of the most successful and widely used ones are the continuum model and the tensegrity model(Van Oosterwyck, Geris, & Aznar, 2015).

In the following, the two strategies and the possible material behaviours used to describe the various elements of these models will be discussed in detail.

4.1 Continuum cell model

Continuum models are models in which all the components of the cell are represented by continuum bodies. The geometry of this type of model can vary greatly ranging from homogeneous models in which the cell is represented as a unique body(J. Chen & Lu, 2012; Mijailovich, Kojic, Zivkovic, Fabry, & Fredberg, 2002) to models in which many subcomponents (usually the membrane, nucleus and cytoplasm) are described as different entities having different mechanical properties(Y. Liu, Mollaeian, & Ren, 2019; Gladilin et al., 2007).

Thanks to their simplicity, these types of models have been successfully adopted for the

study of cells' biomechanics in silico for many years and were among the first types of models to be adopted for FE implementations.

Continuum models tend to reliably reproduce the global response of the cell to various experimental setups such as Atomic Force Microscopy (AFM) indentation tests(J. Chen & Lu, 2012; Y. Liu et al., 2019), magnetic bead twisting tests(Mijailovich et al., 2002) and microplate single cell stretching tests(Gladilin et al., 2007).

These types of models are easy to build and adapt to different goals. In the work of Mijailovich et al.(Mijailovich et al., 2002) the authors built a simplified model in which the cell is represented as a homogeneous isotropic slab on top of which a bead is placed and twisted to simulate magnetic bead twisting tests. The model implemented a linear elastic behaviour for the cell without any sort of discretization. Although the model was so simple it was still able to produce data useful to infer the relationship between the apparent elasticity of the cell experienced by the bead and the actual stiffness of the cell as a whole. This comes to show how even simple models can be effectively used for certain goals.

In the works of Liu et al. and Chen et al., the authors implemented a continuum model of the cell either as a homogeneous isotropic model(J. Chen & Lu, 2012) or as a more complex 3D structure accounting for the presence of the nucleus and its surrounding region(Y. Liu et al., 2019) to reproduce AFM indentation tests. Both works found good agreement with the experimental tests used to both calibrate and validate the models. In this case, the authors implemented a viscoelastic description of the cell that was able, in both studies, to capture the creep response of the cell. Gladilin et al. implemented a model accounting for the non-linear mechanical response by implementing a hyperelastic formulation which proved successful in reproducing microplate stretching experiments in which cells experienced a high level of strain(Gladilin et al., 2007).

One might come to the conclusion that using a simpler model should be preferred to a more complex and realistic approach since they both provide good results and the latter would simply bring an unnecessary layer of complexity and computational effort. This is true if the goal is indeed the simple characterization of some experimental works but that's not always the case. If we are to understand the role of biomechanics in the complex physiology of the cell, we need to be able to address the internal components with a reasonable degree of complexity.

As explained in chapter 2, the role of each subcomponent is clearly distinct from one another and if we are to appreciate the internal balance between these components it is imperative to develop more complex models such as the tensegrity models.

4.2 Tensegrity cell model

A tensegrity structure is composed of tension-bearing cables and compression-bearing elements that form a stable 3D structure without the compression-bearing elements being in contact with one another. From the description of the single components of the cytoskeleton provided in chapter 2, it is easy to see how this structure resembles a tensegrity structure where the microtubules act as the compression-bearing elements and the actin bundles and the actin cortex act as the tension-bearing network. The origin of this type of design is generally attributed to the architect Richard Buckminster Fuller who popularized the tensegrity design in his innovative buildings.

Using the principles of tensegrity structures it is possible to build many different structures. One of the simplest structures is the tensegrity prism here presented in figure 4.1a.

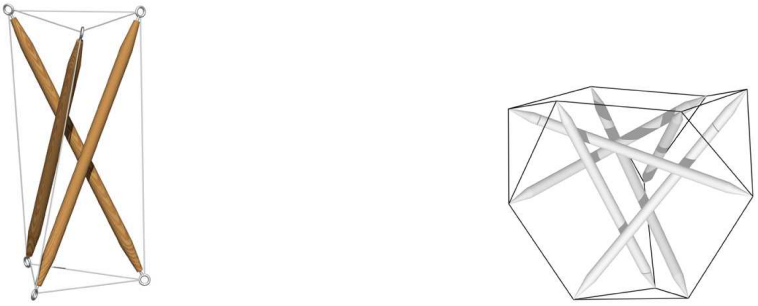

(a) A tensegrity prism (b) A tensegrity tetrahedron

Figure 4.1: Examples of simple tensegrity structures.

The tensegrity prism can be stacked indefinitely to form what is referred to as a Snelson tower from Kenneth Snelson, an American artist and sculptor who is another important pioneer of the principles of tensegrity and its applications. A class of tensegrity structures widely used and of interest for biomechanics is the one inspired by the geodesics on a spherical surface. An example of such a structure is depicted in figure 4.1b.

The first to introduce the idea of using tensegrity structures in the field of cells' mechanobiology was Donald Ingber(D. E. Ingber, 1997). Since then, many studies have proved the viability and usefulness of tensegrity structures in computational models of the cell(McGarry et al., 2004; L. Wang et al., 2019).

The usefulness of tensegrity models comes from their ability to reproduce some aspects of cells' biomechanics which are not captured by other types of models. For example, a tensegrity structure is able to provide a non-linear response using only linear elastic elements, it is able to withstand and alter its internal properties depending on the amount of prestress experienced and provides a structure to the cytoskeleton which is very similar to the one found inside cells.

Although tensegrity structures have a clear-cut definition, the term has been used in this

field with some degrees of freedom since not all the structures used in studies labelled as based on tensegrity do in fact adhere to the principle of unconnected compression-bearing elements. Not only that, a proper tensegrity structure should try to minimize the length of the cables and that is not always the case in the works that can be found in the literature. The concept of tensegrity has generally been used as an intuition and starting point to develop realistic models of the cytoskeleton.

Tensegrity models are mostly used in combination with the more classic continuum models to build hybrid models that contain a tensegrity structure for the cytoskeleton and continuum parts to represent the other components (such as the nucleus, the membrane and the cytoplasm).

As said, the tensegrity structures used to simulate the cytoskeleton of a cell are usually inspired by regular polyhedrons. One of the most used structures is the tensegrity icosahedron depicted in figure 4.2a. In this type of structure, the compression-bearing truss acts as the microtubules of the cell while the tension-bearing cables reproduce the effects of the actin bundles and cortex. This model is already able to represent most of the main mechanical aspects attributed to the cytoskeleton such as the strain-hardening and the non-linear mechanical response in the presence of prestressed cables(McGarry et al., 2004). In this work, the authors also showed how the tensegrity icosahedron can also be adapted to spread models of the cell in the shape of a spherical cap.

In the work of Wang et al.(L. Wang et al., 2019) the authors implemented a slightly more complex version of the tensegrity icosahedron model by adding a set of radial cables representing intermediate filaments similar to what can be seen in figure 4.2b. The filaments are placed radially and span from the nodes of the tensegrity icosahedron to the nodes of the nucleus. This arrangement mimics the role of intermediate filaments as mechanical buffers between the stresses experienced by the cell and the ones transmitted to the nuclear envelope. The authors tested the model both with and without the presence of intermediate filaments and observed that their presence or absence doesn't significantly influence the mechanical response of the cell as a whole but has a significant impact on the nucleus deformation. Thanks to these results, the authors were able to confirm what was already stated in chapter 2 regarding the intermediate filaments: their significance is related to their ability to act as buffers for the mechanical signals from the outside of the cell to the nucleus and thus prompting the biochemical response of the cell to external stimuli.

Considering that the real structure of the cell has the microtubules of the cell sprouting from the same common location near the nucleus (the MTOC), it is clear that a truly evidence-based structure will only take inspiration from tensegrity structures. This is because the central concept of compression-bearing elements not being in contact would be in contrast with this physiological arrangement. A structure that closely resembles this disposition was presented by Barreto et al.(Barreto et al., 2013). In their work, the authors depicted the microtubules as straight beams radially organized. Actin

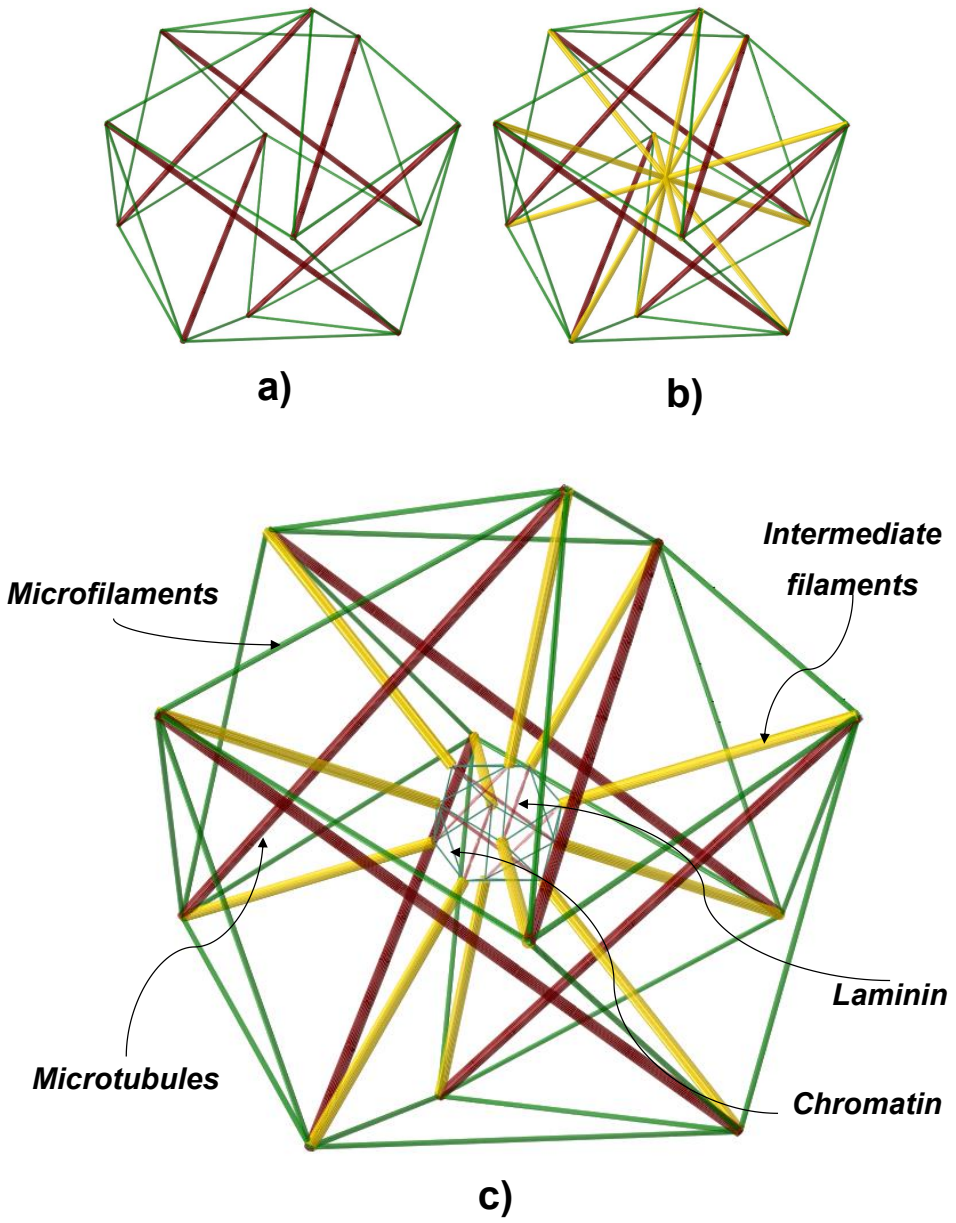

Figure 4.2: Tensegrity structures based on the tensegrity icosahedron. In green the tension-bearing actin, in red the compression-bearing microtubules and in yellow the intermediate filaments. (a) represents a simple tensegrity structure, (b) represents the same structure with the addition of radial intermediate filaments and finally (c) represents a more complex scheme in which an internal tensegrity structure is placed to represent the nuclear envelope.

bundles and the actin cortex have been presented as distinct structures, the former as a shell surrounding the cell and the latter as truss elements arranged near the cortex to simulate peripheral bundles. The model also included the cytoplasm and the nucleus as continuous bodies. The model proved to be very effective in representing the AFM indentation of the cell and was used to test the effect of the elements of the cytoskeleton by either removing one of them or all of them except for one thus isolating the role of each subcomponent. The results showed that in fact all components, except for the peripheral actin bundles, are indeed necessary to faithfully reproduce the experimental data thus highlighting the interconnected role of the various subcomponents as a system. Furthermore, the authors were able to test their results against cells in which specific subcomponents were chemically degraded in-vitro with corresponding models in which these subcomponents were removed. The authors found that the reduction in global stiffness was readily reproduced by their FE model. The authors also found that although the model proved extremely accurate for the tested cell type, it was not able to reproduce the same tests performed on a different cell type. Histological staining of the two cell types showed that the density and arrangement of the cytoskeletal subcomponents were different between the two cell types thus bringing the authors to the conclusion that different properties for the cytoskeletal proteins (or different organizations) have to be used for each cell type. Using the same model, the authors published a work in which they tested the behaviour of the model when subjected to an AFM indentation and to the sliding of the AFM tip along the surface of the cell(Barreto, Perrault, & Lacroix, 2014). In this extensive study, the authors confirmed other intuitions on the mechanical role of specific components and conditions known for cell mechanics. The authors found that the presence of a prestressed state for the actin bundles provided increased stiffness when the AFM tip was moved parallel to the cell surface thus highlighting how the physiological prestress found in the cell is in fact fundamental to understanding the role of actin bundles in the overall mechanical response. Once again, the model was used to test how different subcomponents affect the global response of the cell but this time they distinguished between the two types of tests. They were able to show how the actin-based structure is fundamental in response to stretching and that the microtubules mainly affect the response to compressive stresses.

An even more complex type of tensegrity structure used in the field of cell biomechanics is the one presented in figure 4.2c. In this structure, the model exhibits an internal tensegrity structure representing the nuclear envelope. This model is believed to be better able to represent the actual deformation of the nucleus than what can be obtained by using a continuum representation for this subcomponent. In the work of Bursa et al.(Bursa, Lebis, & Holata, 2012) the authors implemented a tensegrity-inspired structure of this kind made of 210 interconnected elements. The model has been used to evaluate the response of the cell to both micropipette tensile tests and AFM indentation tests providing good results in terms of the global response of the cell but still lacking when observing the degree of nuclear deformation. The authors highlighted how this

fact could be due to the excessive stiffness of the cytoskeletal elements or to the lack of bendability of the compression-bearing microtubules. This is very reasonable since microtubules do bend and buckle when subject to excessive compressive stresses as seen in chapter 2. This is once again a property that is not in common with classic tensegrity since the structural applications of those principles usually involve steel beams as the compression-bearing elements and are more easily stabilized and controlled in the absence of bending and buckling.

Starting from this intuition, a new class of tensegrity-based models is currently on the rise based on bendo-tensegrity: tensegrity structures in which the compression-bearing elements are able to bend and buckle. An example of this kind of approach applied to the tensegrity icosahedron can be found in the work of Fraldi et al.(Fraldi et al., 2019). In this study, the authors found that by simply adding the ability to bend, the model was able to reproduce some aspects not present in previous works such as the presence of non-symmetrical deformations as a result of the buckling of some of the elements. Bansod et al. implemented a very complex bendable structure in their analysis(Bansod, Matsumoto, Nagayama, & Bursa, 2018). This structure fuses the more biologically inspired model of Barreto et al. and the intuition of the need for bendable compression-bearing elements resulting in a 30 nodes star-shaped structure accounting for microtubules, actin filaments and intermediate filaments. The model was able to reproduce stretching tests performed with micropipettes and AFM indentation tests. The authors observed that the global response of the cell is independent of the specific position of the centrosome and confirmed what was already found from the previously cited studies: the components that mainly affect the mechanical response of the cell are the cytoskeleton subcomponents and the cytoplasm. Interestingly, the authors also found out that a similar magnitude of stretching or compression of the cell provides the same amount of stress on the surface of the nucleus thus inferring that the cell's mechanotransduction is similar (aside from the direction of stretching of the nucleus) in this two types of conditions.

One final note has to be made regarding the models presented so far, although they all proved reliable in their own applications and able to underline some previously intuited or never thought aspects of cells' biomechanics and the mechanisms underlying the mechanotransduction, they are all unable to capture a fundamental aspect of the cell. As noted by Barreto et al.(Barreto et al., 2014) all these models do not represent the cytoskeleton as a dynamic system able to reorganize in response to external conditions. While the works that included buckling in microtubules were better able to capture part of the reorganization by a decrease in the apparent stiffness due to the bending of these elements, the long-term reorganization is not included. Some advancements in this field have been made throughout the years via various proposed analytical models. Studies like the ones performed by Ronan et al.(Ronan, Deshpande, McMeeking, & McGarry, 2012), Vigliotti et al.(Vigliotti, Ronan, Baaijens, & Deshpande, 2016) and McEvoy et al.(McEvoy, Deshpande, & McGarry, 2017) all presented complex material models that

account for the reorganization of the cytoskeleton using thermodynamically motivated approaches. To the knowledge of the author, these works are yet to be applied in the field of finite element modelling.

5 A Continuum-Tensegrity FE model for chondrocyte biomechanics in AFM indentation and micropipette aspiration

This chapter is directly taken from an article published by the thesis author as part of the PhD program(Arduino et al., 2022). The work focuses on the identification and validation of a FEM model of a chondrocyte undergoing AFM indentation and MPA tests.

5.1 Introduction

Apart from genes and chemical factors, mechanical stimuli are important regulators for the development of organs and tissues, their growth and connected processes such as remodelling, regeneration or disease (see for example(Huang et al., 2004; D. Ingber, 2003; Panciera et al., 2020)). This strong influence is due to the fact that cells can sense and respond to mechanical signals, by converting them into biochemical responses (this process is called mechanotransduction, first coined in 1998(Carter, Beaupré, Giori, & Helms, 1998)). Moreover, external mechanical forces control the shape, type and function of a living cell by altering its internal balance, (Chicurel, Chen, & Ingber, 1998) thus, modifying the internal prestress of the cell's main subcomponents (the cytoskeleton, the membrane, the cytoplasm and the nucleus) and consequently influencing the biochemical signals produced by the cell(D. Ingber, 2003; Pravincumar, Bader, & Knight, 2012; Van Oosterwyck et al., 2015).

The evidence that biochemistry and signals transmission can be modified by cell mechanics variations is also strictly connected to apparently unrelated diseases manifestation, where abnormal mechanotransduction, sometimes combined with alterations of the Extra Cellular Matrix (ECM) mechanical properties, influences a disease development and spreadin(D. Ingber, 2003; Panciera et al., 2020). In particular, for oncological pathologies, tumour cells are usually characterized by a decrease in the mechanical properties that provide the cell with a higher deformation and mobility, thus suggesting that cell mechanics can be directly linked also to its metastatic potential(E. M. Darling et al., 2007; González-Bermúdez et al., 2019; Huang et al., 2004; D. Ingber, 2003; Zhu, Bao, & Wang, 2000). For this reason, the study of cell mechanics and related properties is facing a growing interest in the last years, from both an experimental and a computational point of view.

Various experimental approaches have been used to describe the passive response of cells(Hao et al., 2020), such as the AFM indentation(E. Darling et al., 2006; E. M. Darling et al., 2007, 2008), which is able to locally stress the cell with compression forces, thanks to a microscale cantilever with a spherical tip, or the Micropipette Aspiration

(MPA) (Evans & Yeung, 1989; González-Bermúdez et al., 2019; Guilak, 2000; Maître et al., 2012; Sato et al., 1990; Trickey et al., 2000, 2004), by means of microscale pipette tips that can apply negative pressure to the cell surface, thus exciting the cell with tensile stresses. Other techniques, such as Magnetic Tweezers (MT), are more interested in determining the mechanical properties of cell subcomponents such as the cytoskeleton(Bausch, Ziemann, Boulbitch, Jacobson, & Sackmann, 1998). However, experimental cell response measurements are usually characterized by a huge variability due to cell phenotypes and types(E. Darling et al., 2006; Efremov, Wang, Hardy, Geahlen, & Raman, 2017; Evans & Yeung, 1989; Lykov, Nematbakhsh, Shang, Lim, & Pivkin, 2017; McGarry et al., 2004; Rodriguez, McGarry, & Sniadecki, 2013; Sato et al., 1990; Trickey et al., 2000), shape(E. M. Darling et al., 2008), source(E. M. Darling et al., 2007; Lykov et al., 2017; Rodriguez et al., 2013), and ageing(Phillip, Aifuwa, Walston, & Wirtz, 2015). This being the case, it is quite difficult to fully describe the mechanical behaviour of a cell by means of in-vivo tests, and even more difficult to extract the role of each subcomponent.

For this reason, in-silico computational models have been developed through the years, to overcome such limitations and uncertainties, while proposing a valuable tool to understand cell mechanical behaviour(Baaijens et al., 2005; Bansod & Bursa, 2015; Barreto et al., 2014; Bursa et al., 2012; Katti & Katti, 2017; McGarry et al., 2004; Rajagopal, Holmes, & Lee, 2018; Zhou et al., 2005). Some of these models describe the cell as a homogeneous viscoelastic material(Baaijens et al., 2005; Bansod & Bursa, 2015; Barreto et al., 2014; Zhou et al., 2005), others specify the main subcomponents adopting a tensegrity structure to model the cytoskeleton(Bursa et al., 2012; Katti & Katti, 2017; Khunsaraki, Oscuii, & Voloshin, 2020; McGarry et al., 2004), as stated and assessed in past works(D. E. Ingber, 2003b, 2003a; Van Oosterwyck et al., 2015).

Computational models usually aim at describing cells undergoing AFM indentation, accounting for cell mechanics variability(Barreto et al., 2014) or the effect of an altered cytoskeleton to predict the mechanics of cancer cells(Katti & Katti, 2017), as well as MPA, to understand the influence of the pipette shape and the material properties(Baaijens et al., 2005; González-Bermúdez et al., 2019; Zhou et al., 2005).

For this purpose, thanks to a computational approach, we used finite elements to analyse the mechanical response of a cell experiencing both AFM indentation and MPA techniques, in order to: (i) develop a homogeneous model that is able to catch the global viscoelastic response of a cell subjected to both compression and tensile mechanical stimuli; (ii) propose a combined continuous-tensegrity model to observe how each subcomponent contributes to the overall mechanical behaviour; (iii) compare the two models to elucidate the influence of the cytoplasm and the cytoskeleton, by varying their mechanical properties. We first set both the homogeneous and the continuum-tensegrity models for the description of the AFM indentation tests, and then we validated their applicability with the MPA simulations, highlighting from these two types of tests some

useful insights on the roles of the subcellular components.

5.2 Finite element models of the cell and its subcomponents

Three-dimensional (3D) models of a cell were realized with the finite element software Abaqus Explicit 2019 (Dassault Systemes Simulia Corp., Providence, RI).

The model simulated a 16 μm diameter cell (similarly to the work of McGarry and Pendergast(McGarry et al., 2004)), composed of all those features that mainly contribute to the cell mechanics, such as the cytoskeleton (microfilaments and microtubules), the cytoplasm, the cell membrane and the nucleus (figure 5.1). A homogeneous continuous model (CM) and a combined continuous-tensegrity model (CTM) were developed to analyse the mechanical response of a cell undergoing AFM indentation and aspiration through micropipette.

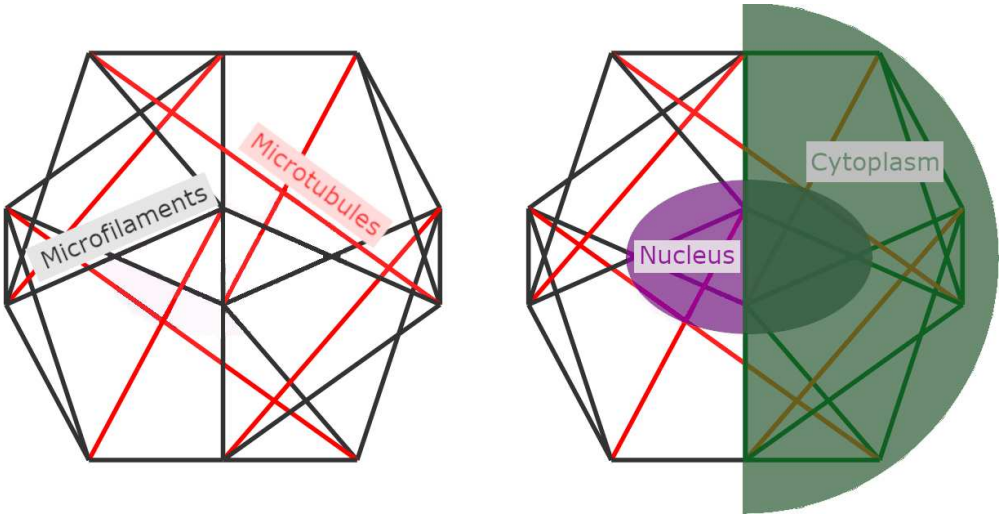

Figure 5.1: Continuum-tensegrity model of the cell, where the lattice represents the cytoskeleton (with microfilaments in black and microtubules in red), while the nucleus, membrane and cytoplasm are described as homogeneous materials.

In the CM the cell was represented with a 3D solid-sphere composed only by the cytoplasm, discretized by means of about 100.000 linear hexahedral elements, 110.000 nodes and 360.000 degrees of freedom. Within the CTM, the nucleus was represented, with reference to the literature(McGarry et al., 2004), as an ellipsoid (major axis 8 μm and minor axis 5 μm) while the membrane was modelled with a shell part with a constant thickness of 6 nm. In this case, the cytoskeleton was described with a tensegrity structure of six compression bearing struts and twenty-four tensional cables that are able to mimic the real behaviour of the microtubules and the microfilaments, respectively(Bursa et al., 2012; D. E. Ingber, 2003b, 2003a; McGarry et al., 2004). The connection between each strut and cable created twelve common nodes, representing

the 'receptor' sites where actin filaments clustered at adhesion complexes. Regarding their geometry, the microtubules had a cross-sectional area of 190 nm^2, while the microfilaments were thinner, with an area of 18 nm^2(McGarry et al., 2004). The CTM was discretized with a number of linear hexahedral elements between 70.000 and 400.000 depending on the model complexity, about 35.000 linear quadrilateral elements for the cell membrane and one linear truss element for each cytoskeletal subcomponent. In the model, the nodes of the membrane were coincident with the underlying cytoplasm and with cytoskeletal receptor sites, and tie constraints were assigned to cell subcomponents. The total number of nodes was within the range 105.000–440.000 resulting in 370.000–1.500.000 degrees of freedom.

Even if the model has the potential to mimic all kinds of cells, this work primarily focused on chondrocytes (specialized cells present in the cartilage) and could be addressed to chondrosarcoma cells (malignant tumour cells that originate from chondrocytes), thanks to a larger availability of data in the literature with respect to other cells.

5.3 Experimental tests on cells

5.3.1 AFM indentation tests

Atomic Force Microscopy (AFM) indentation is a powerful and versatile technique employed to investigate cell mechanics. At its core, AFM consists of a sharp probe, typically made of silicon or silicon nitride, attached to a flexible cantilever of known stiffness. The probe's tip is brought into close proximity to the cell's surface, and precise control allows for the application of a controlled force onto the cell. As the probe tip interacts with the cellular material, the cantilever deflects proportionally to the forces acting on it. This deflection is measured by a laser beam, which is directed onto the cantilever's back, creating an optical lever effect that accurately translates the deflection into force measurements(Lekka et al., 1999).

During AFM indentation, the cantilever gently pushes into the cell's surface, creating a force-indentation curve. This curve provides critical information about the cell's mechanical properties. Specifically, researchers can extract quantitative data useful to evaluate the cell's elastic and viscoelastic behaviour.

One of the significant advantages of AFM indentation is its ability to work in physiological conditions, where cells can be maintained in their native environment, preserving their structural and mechanical integrity. Moreover, different shapes and sizes of the AFM tip can be used to probe different regions of the cell, such as the cell membrane, cytoplasm, and nucleus, thus offering valuable spatial information about the mechanical heterogeneity within cells(Gavara & Chadwick, 2012).

Most works use a spherical probe tip thus capturing the behaviour of the cell as whole (E. Darling et al., 2006). While the use of a sharper tip can lead to higher spatial

resolution and the isolation of the effects given by different regions and subcomponents of the cell(Gavara & Chadwick, 2012).

The AFM indentation has also been applied to diseased cells such as cancer cells as first pioneered by the work of Lekka et al.(Lekka et al., 1999). Their work helped confirm that cancer cells tend to present a lower Young's modulus than their healthy counterparts.

In order to evaluate the stiffness of a cell undergoing AFM indentation tests, a model of the interaction between the cell and the probe has to be established. A good analytical model usually employed in this case is the Hertz contact model(E. Darling et al., 2006), reported in Equation 1, which describes the interaction between two spheres, one of which is assumed to be infinitely rigid. Given that the cantilever tip usually presents a stiffness many orders of magnitude higher than the one of the cell, it is possible to use this equation to describe the force-displacement relationship during the loading phase of an indentation experiment:

$$F = \frac{4E_{el}R^{1/2}}{3(1-\nu^2)} \cdot \delta^{3/2} \tag{1}$$

Where δ is the indentation length, E_{el} is the Young's modulus of the cell, ν is the Poisson's ratio and R is the equivalent radius for the experiment calculated using the relationship:

$$R = \left(\frac{1}{R_{cell}} + \frac{1}{R_{tip}}\right)^{-1} \tag{2}$$

where R_{cell} is the radius of the cell and R_{tip} is the radius of the cantilever spherical tip.

Using the AFM indentation approach it is possible to perform stress-relaxation tests on cells by applying and keeping a fixed displacement of the tip and registering the evolution of the contact forces. In order to quantify the resulting viscoelastic effect of the cell the relationship between the force and the displacement can be described by employing a Solid Linear Standard model (SLS) applied to the Hertz model described in equation 1 thus resulting in(E. M. Darling et al., 2007; E. Darling et al., 2006):

$$F = \frac{4E_R R^{1/2}\delta^{3/2}}{3(1-\nu^2)} \cdot \left(1 + \frac{\tau_\sigma - \tau_\epsilon}{\tau_\epsilon} e^{-t/\tau_\epsilon}\right) \tag{3}$$

where τ_σ and τ_ϵ are the relaxation times under constant load and constant deformation respectively, while E_R corresponds to the stiffness of the elastic branch of Maxwell's standard linear solid model. By fitting Equation 3 to a force-displacement curve, it is possible to obtain a standard linear solid representation of the cell's viscoelastic response, where:

$$E_0 = E_R\left(1 + \frac{\tau_\sigma - \tau_\epsilon}{\tau_\epsilon}\right) \qquad E_\infty = E_R(1+\nu) \tag{4}$$

where E_0 and E_∞ are the instantaneous and long-term elastic response respectively and ν is the Poisson's ratio of the cell(E. M. Darling et al., 2007).

5.3.2 Micropipette aspiration tests

Micropipette aspiration is a powerful technique used to investigate cell mechanics in the realm of cellular biomechanics. In this method, a micropipette with a fine, controlled radius is brought into proximity to the cell's surface. The pipette gently applies a known pressure to aspirate a small portion of the cell into the pipette, creating a measurable deformation. By monitoring the pressure needed to achieve this deformation, researchers can extract valuable data useful to evaluate the cell's elastic and viscoelastic behaviour.

Similarly to AFM indentation, micropipette aspiration offers the advantage of working under physiological conditions, enabling cells to remain viable and functional during the experiments.

During the micropipette aspiration process, the aspirated cell's deformation is visualized and recorded using advanced microscopy techniques, allowing for precise measurements. Additionally, this method can be used to investigate specific regions of the cell, such as the cell membrane, and cytoplasm by choosing appropriate values for the micropipette radius and pressure thus providing valuable insights into the spatial variations of cellular mechanics.

The micropipette aspiration technique is particularly useful in studying the response of cells to mechanical forces, including changes in their mechanical properties under different physiological and pathological conditions. It has significant applications in various areas of cell biology, tissue engineering, and regenerative medicine, offering crucial information for understanding cellular behaviour and mechanical responses in complex biological systems.

The pressure-displacement data collected can be then interpreted by means of an appropriate analytical model in order to extract the mechanical parameters of the cell. A frequently used model in this regard is the half-space viscoelastic model developed by Sato et al.34 which represents an extension of the previous half-space elastic model by Theret et al.37 This viscoelastic model assumes an incompressible behaviour for the cell. The aspiration length can be obtained from the following equation:

$$L_p(t) = R_p \frac{\phi \Delta P}{\pi E_1} \left(1 - \frac{E_2}{E_1 + E_2} e^{-t/\tau}\right) \tag{5}$$

where L_p is the projection length of the cell inside the pipette, R_p is the micropipette radius, ΔP is the pressure applied to the cell's surface, E_2 and E_1 are the elastic constants of the springs of the corresponding Maxwell standard linear solid representation of the cell, τ is the characteristic time of the creep response and finally ϕ is the "punch coefficient" usually reported to be $\phi = 2$.1.19,41

However, the half-space analytical model presents some limitations when applied to cell biomechanics, as also already reported in some works,1,41 since cell behaviour is compressible, with an average Poisson's coefficient of 0.35–0.4 and strains are not

infinitesimal. Cells can be described as incompressible when the rate of pressure applied to them is faster than the ability of the cell to modulate its volume using the channels described in chapter 1 but becomes too restrictive when dealing with the long-term viscoelastic response of the cell.

5.3.3 Boundary conditions for AFM indentation tests

The Atomic Force Microscope indentation was performed on a rounded cell adherent to a rigid substrate, where cell height and contact radius with the substrate were assumed with reference to the work of McGarry and Prendergast(McGarry et al., 2004), thus about 14 μm and 6 μm, respectively. A spherical rigid body simulated the cantilever tip of the AFM. Different analyses were performed with 5 μm and 10 μm tip diameter sizes, to observe possible changes induced by the indenter size in the load–displacement response of both the CM and CTM, such as the non-linear contribution of the cell subcomponents. The contact between the cell and the indenter was assumed to be frictionless, for the tangential behaviour, and hard contact type, for the normal behaviour. The bottom nodes, at the cell-substrate interface, were constrained in all three translational degrees of freedom. These constrained points mimicked the focal adhesion sites in cells adherent to a substrate, thus implying that the substrate is adopted as rigid. In some recent works, the influence of a solid substrate has been studied, especially when a large probe indents a spread cell, thus some bottom-effect corrections have been proposed(Garcia & Garcia, 2018; Garcia, Guerrero, & Garcia, 2020). However, thanks to the comparison with the Hertz model of the contact between two spheres and the models' outputs, we noticed no undesired effects due to the applied boundary conditions, probably also because we are adopting an almost spherical configuration of the cell, instead of a spread one.

The analyses were performed with a two-step dynamic explicit simulation. Similarly to experimental protocols reported in the literature(E. Darling et al., 2006), during the first step, a 1500 nm displacement was applied by the spherical indenter to the top of the cell; then this loading phase was followed by a relaxation one in which the cantilever was held in place for up to 60 s (figure 5.2). In this way, stress relaxation tests were performed on the central region of the cell using a 9.5 $\mu m/s$ approach velocity(E. M. Darling et al., 2008).

5.3.4 Boundary conditions for MPA tests

The Micropipette Aspiration tests simulated the interaction with a rounded visco-hyperelastic cell and a round rigid cylindrical pipette with a smooth-edged mouth and 900 nm round fillet. In this case, several simulations were realized, considering different ratios between the cell and the micropipette radii, more precisely with ratio values of 1.5, 2, 3, 4 and 5.5. The contact between the cell and the micropipette was assumed to be frictionless (tangential behaviour), and hard contact type (for the normal behaviour).

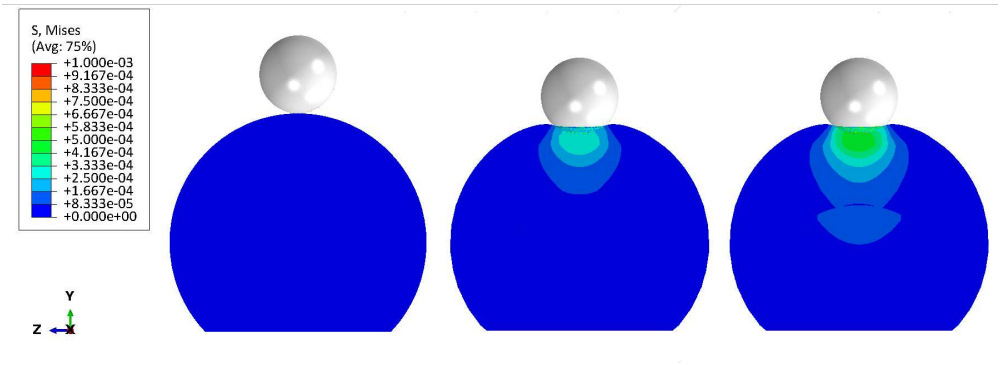

Figure 5.2: Analyses steps for the AFM indentation and stress relaxation tests. At the beginning of the simulation, the cell is at rest and put in contact with the rigid sphere representing the indenter. After approximately 0.16 s the maximum displacement is reached and stress relaxation begins. The rightmost figure shows the progressive reduction in the cell stresses due to stress relaxation. Von Mises stress distribution is reported with colourmap and graduated scale (in MPa).

The Micropipette Aspiration tests were performed with a two-time step dynamic explicit simulation, similarly to the AFM indentation. During the first step, lasting 1 s, the cell was exposed to a fluid negative pressure variation $-\Delta P$, within the micropipette. After this phase, the creep response of the cell was analysed by keeping a constant $-\Delta P$ and measuring the projection length L_P of the cell inside the pipette for up to 60 s (figure 5.3).

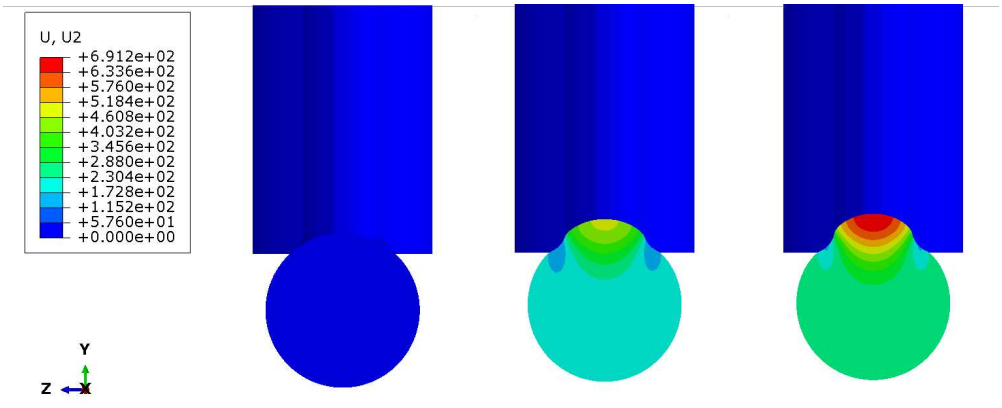

Figure 5.3: Analyses steps for the MPA and creep tests. At the beginning of the simulation, the cell is at rest and put in contact with the cell. The negative pressure is applied to the surface of the cell inside of the pipette and it is increased over 1 s after which it is kept constant to observe the creep effect. The rightmost figure shows the progressive increase in the projection length due to the creep effect. Total cell displacement is reported with colourmap and graduated scale (in nm).

Since there was a concentration of the deformation gradient near the pipette fillet, a dense mesh in the upper part of the cell was adopted, for both the cytoplasm and the

plasma membrane.

5.4 Mechanical properties of the cell subcomponents

Both the CM and the CTM were tested with viscoelastic and visco-hyperelastic material properties. The Neo-Hookean formulation was used for the hyperelastic material model. The mechanical properties adopted in this study are reported in tables 5 and 6, with reference to the several analysed configurations.

	Cytoplasm						
	E_{el}	E_R	τ_σ	τ_ϵ	ν	C_{10}	D_1
Viscoelastic model	1.28E-03	4.5E-04	19.7	9.5	037	-	-
Visco-hyperelastic model	-	-	19.7	9.5	037	2.33E-4	1220.66

Table 5: E_{el} (MPa) is the Young's modulus assuming a linear elastic formulation for the loading phase; E_R (MPa) is the relaxed modulus (see (E. M. Darling et al., 2008) for reference); τ_σ (s) time of relaxation of deformation under constant load; σ_ϵ (s) time of relaxation of load under constant deformation; ν (-) Poisson's coefficient; C_{10} (MPa) and D_1 $(\text{MPa})^{-1}$ are the parameters of the corresponding Neo-Hookean model.

	Continuum-tensegrity visco-hyperelastic model						
	E_{el}	E_R	τ_σ	τ_ϵ	ν	C_{10}	D_1
Cytoplasm	1.28E-03	4.5E-04	19.7	9.5	037	2.33E-4	1220.66
Microtubules	1.53E+04	-	-	-	0.38	2.78E+03	9.39E-05
Microfilaments	3.32E+04	-	-	-	0.38	6.02E+03	4.33E-05
Cell membrane	1.28E-02	-	-	-	0.3	2.46E-03	1.88E+02
Nucleus	5.11E-03	-	-	-	0.37	9.33E-04	3.05E+02

Table 6: E_{el} (MPa) is the Young's modulus assuming a linear elastic formulation for the loading phase; E_R (MPa) is the relaxed modulus (see (E. M. Darling et al., 2008) for reference); τ_σ (s) time of relaxation of deformation under constant load; σ_ϵ (s) time of relaxation of load under constant deformation; ν (-) Poisson's coefficient; C_{10} (MPa) and D_1 $(\text{MPa})^{-1}$ are the parameters of the corresponding Neo-Hookean model.

Both AFM indentation and MPA analyses lasted between 1 and 72 h, depending on the model complexity and the number of required steps, running contemporary on 20 threads of a High-Performance Computing Server Fujitsu Primergy RX4770 equipped with four Intel Xeon E7 8890 v4 processors, 512 GB RAM and SSD HD.

5.5 Simulation results

5.5.1 AFM Indentation: Loading Phase and Stress Relaxation Behaviour

Firstly, the AFM experiment was simulated with a homogeneous computational model, similar to past works(Shin & Athanasiou, 1999; Baaijens et al., 2005; Zhou et al., 2005). Both linear elastic and Neo-Hookean hyperelastic formulations were adopted and compared with respect to the Hertz analytical model, to confirm the almost equal response. In figures 5.4 and 5.5 we reported the comparison between the linear elastic Hertz model and different model configurations all with the Neo-Hookean material formulation.

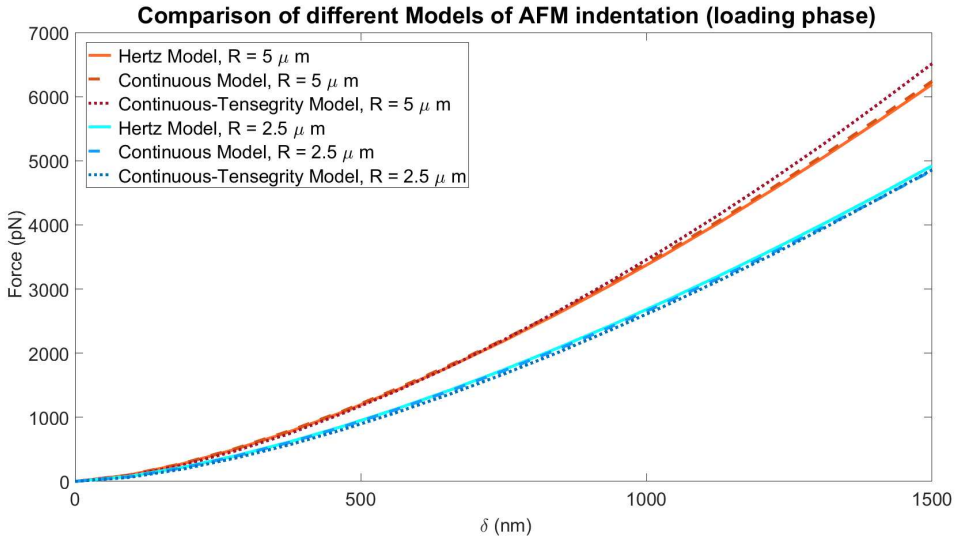

Figure 5.4: Comparison between the Hertz analytical model (HM, continuous lines), the homogeneous continuum model with hyperelastic formulation (CM, dashed lines) and the continuum-tensegrity model (CTM, dotted lines) during AFM loading phase. Two indenter sizes (R = 2.5 μm and 5 μm) were analysed with an indentation length of 1.5 μm. Mechanical parameters that were used for both the loading and stress-relaxation phases are reported in tables 5 and 6.

The force-displacement curves obtained using the two different indenter sizes (namely R = 2.5 μm and 5 μm) revealed a similar behaviour of both material formulations, close to the Hertz predictions, thus they can be used as a reference for the comparison with the complex continuum-tensegrity model.

In addition, stress relaxation data were obtained from the second step of the simulations, and reported with reference to the Hertz viscoelastic model (Eq. 1). In order to qualitatively and quantitatively describe the contribution of the cytoplasm versus the cytoskeleton, the mechanical properties of each subcomponent were altered using various parameters combinations, as reported in table 7. The parameter Q = E_{el1}/E_{el2} = 12.78

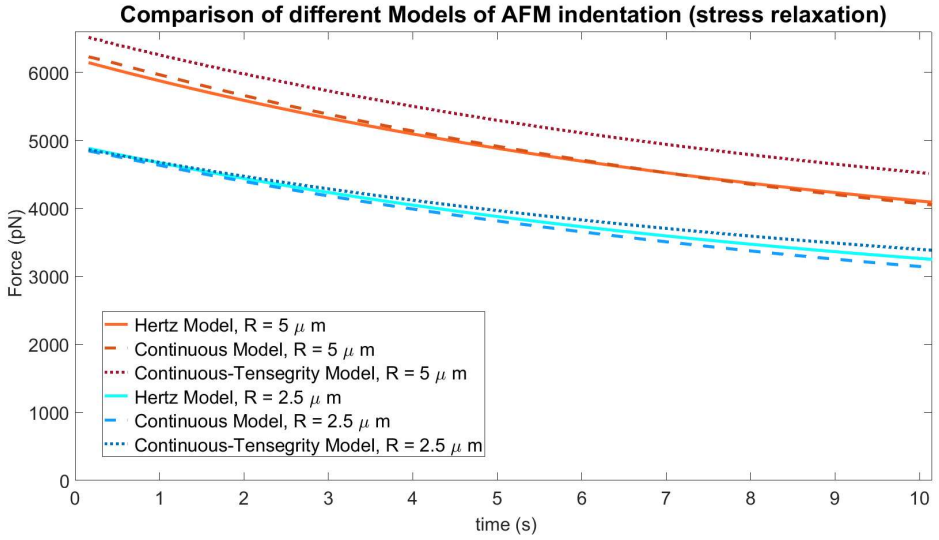

Figure 5.5: Comparison between the Hertz analytical model (HM, continuous lines), the homogeneous continuum model with hyperelastic formulation (CM, dashed lines) and the continuum-tensegrity model (CTM, dotted lines) during AFM Stress Relaxation phase. Two indenter sizes (R = 2.5 μm and 5 μm) were analysed with an indentation length of 1.5 μm. Mechanical parameters that were used for both the loading and stress-relaxation phases are reported in tables 5 and 6.

is the ratio between the elastic moduli of the cytoplasm of cell type 1 (E_{el1}) and cell type 2 (E_{el2}), and it was used to increase or decrease the mechanical properties between these cell types, obtaining other four sets of mechanical properties (Table 8).

		Cytoplasm	**Microtubules**	**Microfilaments**	**Membrane**	**Nucleus**
Fixed Parameters	E_R	4.50E-04	-	-	-	-
	τ_σ	19.7	-	-	-	-
	τ_ϵ	9.5	-	-	-	-
	ν	0.37	0.38	0.38	0.3	0.37
Cell type 1	E_{el}	1.28E-03	1.53E+04	3.32E+04	1.28E-02	5.11E-03
	C_{10}	2.33E-03	2.78E+03	6.02E+03	2.46E-03	9.33E-04
	D_1	1.22E-03	9.39E-05	4.33E-05	1.88E+02	3.05E+02
Cell type 2	E_{el}	1.00E-04	1.20E+03	2.60E+03	1.00E-03	4.00E-04
	C_{10}	1.83E-05	2.17E+02	4.71E+02	1.92E-04	7.30E-05
	D_1	1.56E+04	1.20E-03	5.54E-04	2.40E+03	3.90E+03

Table 7: These values were used to evaluate the role of the tensegrity structure with respect to the overall mechanical response of the computational model. E_{el} (MPa) is the Young's modulus assuming a linear elastic formulation; E_R (MPa) is the relaxed modulus; τ_σ (s) time of relaxation of deformation under constant load; σ_ϵ (s) time of relaxation of load under constant deformation; ν (-) Poisson's coefficient; C_{10} (MPa) and D_1 (MPa)$^{-1}$ are the parameters of the corresponding Neo-Hookean model.

		Cytoplasm	Microtubules	Microfilaments	Membrane	Nucleus
Cell type 1*Q	**Eel**	1.28E-03	1.96E+05	4.25E+05	1.63E-01	6.53E-02
	C10	2.33E-04	3.55E+04	7.69E+04	3.14E-02	1.19E-02
	D1	1.22E+03	7.35E-06	3.39E-06	1.47E+01	2.39+01
Cell type 1/Q	**Eel**	1.28E-03	1.20E+03	2.60E+03	1.00E-03	4.00E-04
	C10	2.33E-04	2.18E+02	4.71E+02	1.92E-04	7.30E-05
	D1	1.22E+03	1.20E-03	5.50E-04	2.40E+03	3.90E+03
Cell type 2*Q	**Eel**	1.00E-04	1.53E+04	3.32E+04	1.28E-02	5.11E-03
	C10	1.82E-05	2.77E+03	6.02E+03	2.45E-03	9.33E-04
	D1	1.56E+04	9.39E-05	4.33E-05	1.88E+02	3.05E+02
Cell type 2/Q	**Eel**	1.00E-04	9.39E+01	2.03E+02	7.82E-05	3.13E-05
	C10	1.82E-05	1.70E+01	3.69E+01	1.50E-05	5.71E-06
	D1	1.56E+04	1.53E-02	7.08E-03	3.07E+04	5.00E+04

Table 8: Four parameter combinations to stress both the role of the cytoplasm and the cytoskeleton to the overall mechanical cell response. The values of E_R, τ_σ, σ_ϵ and ν are kept as reported in table 7. E_{el} (MPa) is the Young's modulus assuming a linear elastic formulation; C_{10} (MPa) and D_1 (MPa)$^{-1}$ are the parameters of the corresponding Neo-Hookean model.

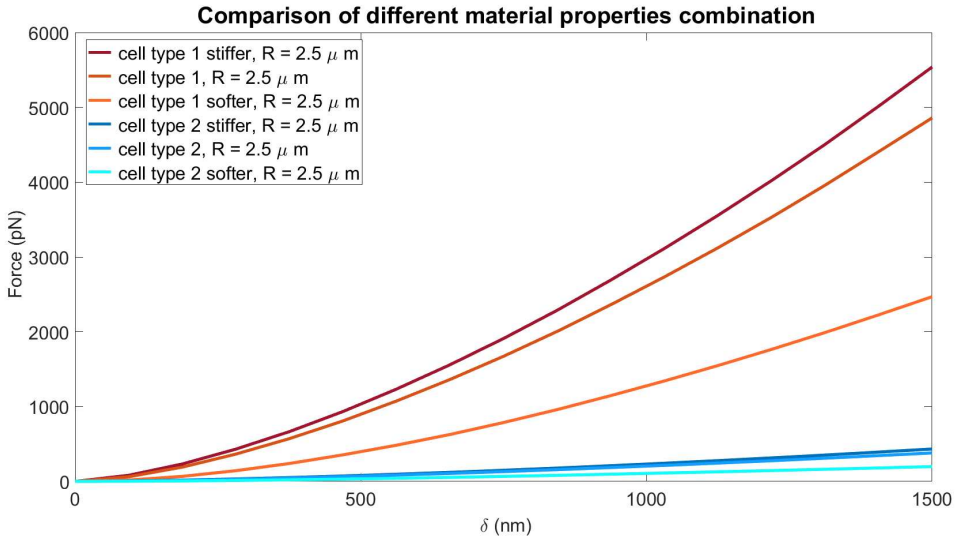

Figure 5.6: Comparison of different combinations of material properties for the cytoskeleton and the cytoplasm to observe the role of the tensegrity structure in the overall mechanical response of the model. Stiffer refers to the cell type 1 or 2 multiplied by Q, while softer states for cell type 1 or 2 are divided by Q. The parameters of each curve are described in tables 7 and 8.

The results of these simulations are reported in figure 5.6 while normalized values with respect to the maximum force reached in each group is shown in figure 5.7. It is possible to observe how the overall mechanical response is more affected by a decrease in the mechanical properties of the cytoskeleton rather than by its increase.

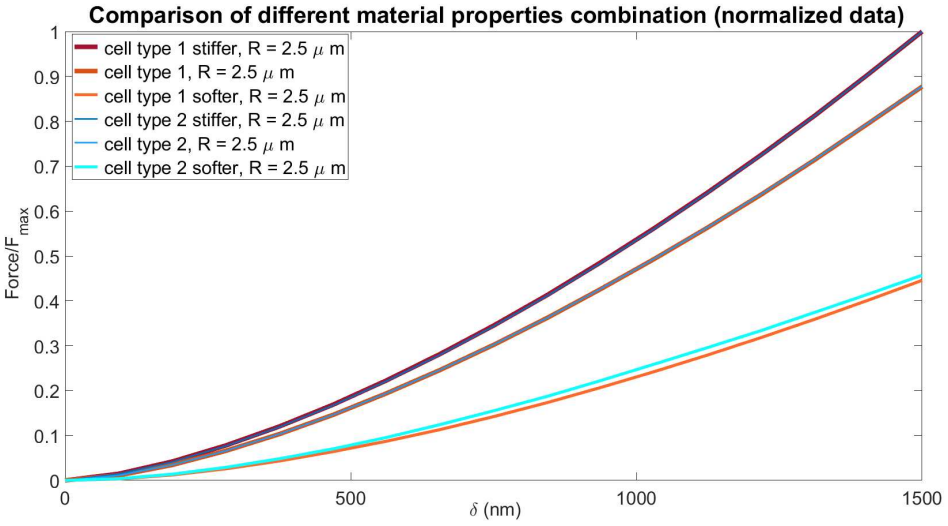

Figure 5.7: normalized results of Figure 5.6 with respect to the maximum force obtained for both cell type 1 and 2.

5.5.2 Micropipette Aspiration: Loading Phase and Creep Behaviour

In Figure 5.8 it is possible to observe the comparison between compressible and incompressible models of the micropipette aspiration during the loading phase using different values of the ratio between the micropipette diameter and the cell diameter. Some curves are obtained from the work of Baaijens et al.(Baaijens et al., 2005) and are compared with our simulations and the half-space model developed by Theret et al.(Theret et al., 1988) In figure 5.9 it t is possible to observe the influence of the Poisson's ratio during the loading phase, comparing our model with different results by Baaijens et al.(Baaijens et al., 2005) and the half-space model, highlighting the effects of adopting a compressible model instead of an incompressible one.

Since the ratio D_c/D_p has been shown to play a significant role in the resulting stimulus–response curves, different ratios have been further investigated (figure 5.10) and compared with previous results obtained from the literature(Baaijens et al., 2005). To account for possible coupling and scale effects, both the micropipette and the cell radii were alternatively changed, resulting in different combinations of D_c/D_p values.

The computational model has been tested for its viscoelastic response as well. Two of the simulations obtained using two values of the D_c/D_p ratio, as well as the experimental curve from the work of Baaijens et al.(Baaijens et al., 2005) are reported in figure 5.11. Then, once the CM has been validated by comparison with both computational and experimental data obtained from literature, the CTM has been included within the finite element simulation of micropipette aspiration, and compared with respect to the former model. Different orientations of the cytoskeleton could alter the results; thus, two possible tensegrity icosahedron dispositions were used. Figure 5.12 reports the

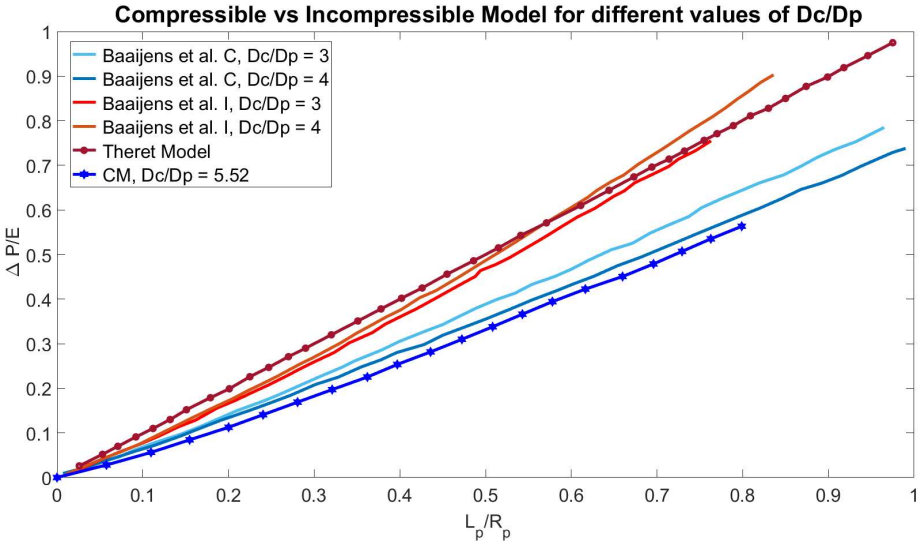

Figure 5.8: Comparison between incompressible (I) and compressible (C) models of the loading phase of a cell undergoing micropipette aspiration for different values of D_c/D_p. The curves from the work of Baaijens et al.(Baaijens et al., 2005) are compared to the Half-Space analytical model (red line with dot markers) and to our simulation (starred blue line). The cell diameter is fixed.

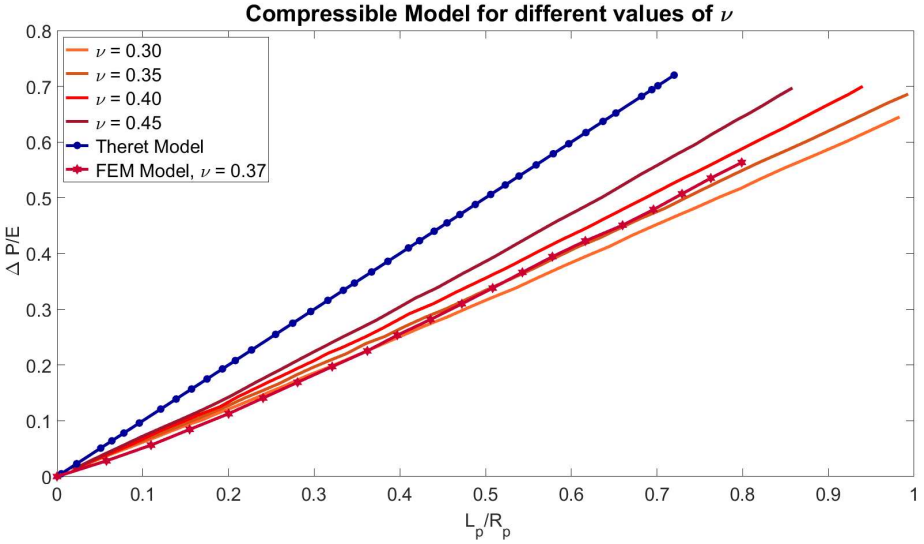

Figure 5.9: Dependence of the model by the Poisson's ratio. Data from the work of Baaijens et al.(Baaijens et al., 2005) are reported, compared with our simulation (starred red line), and the Half-Space model (blue line with dot markers).

two analysed configurations and figure 5.13 summarizes the results obtained during the loading phase in these simulations.

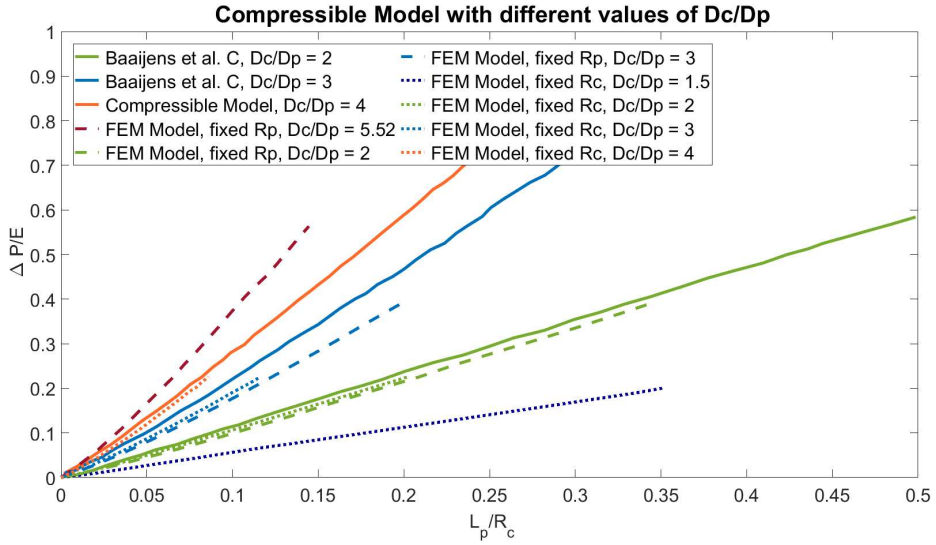

Figure 5.10: Comparison of simulations of the loading phase of the micropipette aspiration employing different D_c/D_p ratios. Different colours highlight the ratios (blue for 1.5, green for 2, light blue for 3, orange for 4 and red for 5.52) while different styles were used to identify our data and Baaijens et al.(Baaijens et al., 2005) Data are normalized with respect to cell radius instead of micropipette radius.

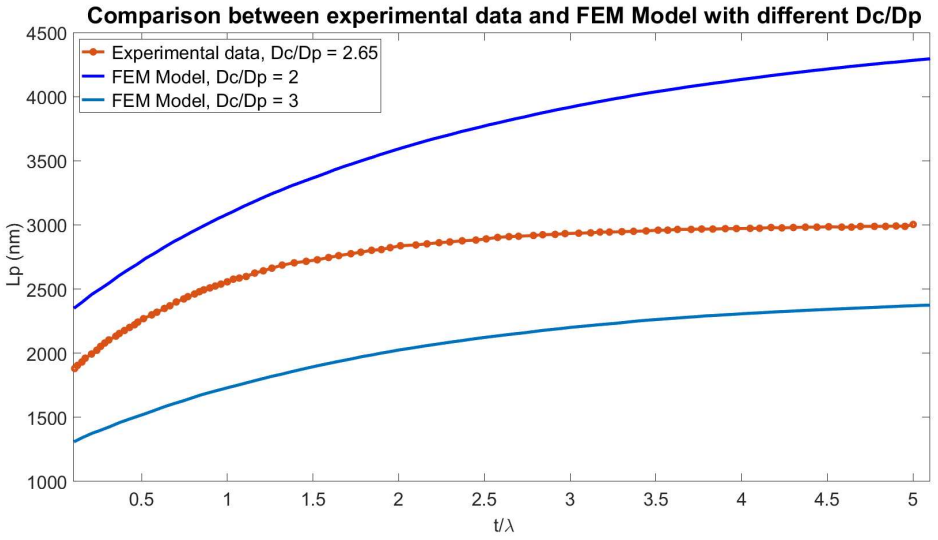

Figure 5.11: Comparison between experimental data (from Baaijens et al.(Baaijens et al., 2005)) and simulations by changing D_c/D_p.

5.6 Discussion

It has been assessed that a tumour cell exhibits a variation in its mechanical behaviour with respect to a healthy cell, which implies also a change in the mechanotransduction of signals that regulate its normal routine processes. For this reason, in-silico computational models have been developed throughout the years to deepen the knowledge about

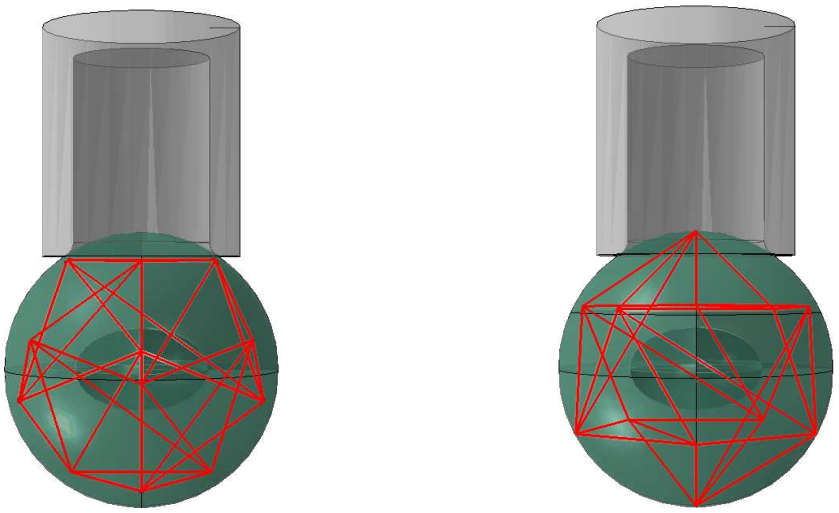

(a) Configuration 1 (b) Configuration 2

Figure 5.12: Configurations used for the MPA simulations using the CTM.

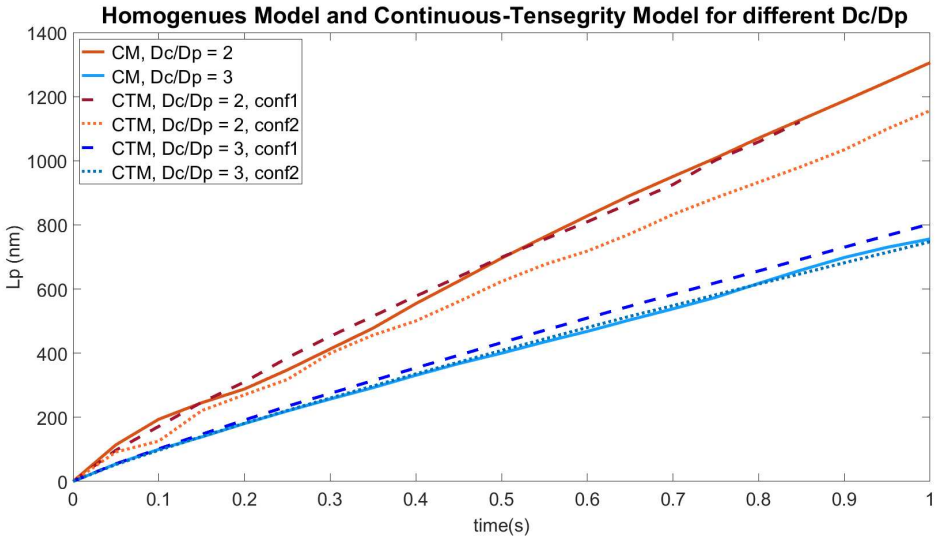

Figure 5.13: Aspiration length in time, with respect to the initial configuration of the cell cytoskeleton. A comparison with the CM is reported, as well as two different case studies with D_c/D_p equal to 2 and 3.

cell mechanical behaviour without experimental uncertainties. With this aim, in this work, we developed a finite element model of a cell and its subcomponents in order to evaluate and quantify the influence of each part, when the same cell is subjected to compression and tensile mechanical stimuli.

The first approach consisted in adopting a continuum model (CM) with a homogeneous material to simulate AFM indentation on a single cell and the related stress relaxation behaviour. Both the loading and stress-relaxation phases were confirmed by the Hertz model (figures 5.4 and 5.5), where an optimal correspondence was reached. When

the tensegrity structure and the other components were added to the computational model, a similar trend was noticed, but characterized by larger values, especially when increasing the indenter size. In particular, the load–displacement curve of the CTM slightly deviated from both the linear Hertz model and the CM when the indenter tip was greater. This aspect highlighted the contribution of the cell subcomponents with respect to the CM, when the behaviour became non-linear (greater displacements). Moreover, these effects became more evident if other parameters combinations were considered, as shown in figures 5.6 and 5.7, where the Young's modulus of the cytoplasm was kept constant and the other subcomponents' elastic moduli were variated by a factor Q. Computational results showed that a stiffer cytoskeleton, membrane and nucleus contribute in enhancing the response of the cell subjected to a compression force, but this influence is even more noticeable when these subcomponents are characterized by a softer behaviour, which strongly affects the overall cell mechanics (figure 5.6). Similar trends were found by changing cell type from 1 to 2, which consists of a softer cytoplasm (one order of magnitude lower). When considering the normalized results in order to analyse only the influence of cell subcomponents (figure 5.7), it is possible to infer that they significantly modify a cell's mechanical behaviour, regardless of the cytoplasm. In Barreto et al.(Barreto et al., 2014) the importance of actin filaments and microtubules during cell compression was highlighted, and in Katti et al.(Katti & Katti, 2017) they observed that a decrease in the mechanical properties of the cytoskeleton dramatically influences the global cell behaviour. In addition, Khunsaraki et al.(Khunsaraki et al., 2020), observed that the cytoskeleton is the most involved part to carry the reaction force during the AFM tip indentation. From our insights, we can also state that cytoplasm is able to influence the global mechanical response of a cell undergoing AFM indentation, since its variation led to significantly different behaviours of the cell, but cell subcomponents (especially the cytoskeleton) are the ones able to tune the overall cell behaviour in a not uniform way. This is evident in figures 5.6 and 5.7, where different mechanical parameters combinations were used: by reducing the mechanical properties of the subcomponents of one order of magnitude, the mechanical response of the cell significantly decreases while increasing them of the same amount does not influence the global response in the same way.

When dealing with MPA, other useful aspects emerged from the computational models. Theret's elastic model(Theret et al., 1988) has been adopted through the years to obtain the elastic properties of the cell (i.e., the elastic modulus) by describing a linear dependence between the normalized aspiration length and the applied pressure (see for example (E. Darling et al., 2006; Pravincumar et al., 2012; Sato et al., 1990; Sliogeryte et al., 2016)), as reported by Eq. (6). Theret's model assumes the cell as a homogeneous incompressible half space and considers only infinitesimal strains. However, it has been observed1 that this common approach is not suitable for cells characterized by a Poisson's coefficient $\nu < 0.5$ and subjected to large elongations. Moreover, in MPA, cells and micropipette sizes are comparable, thus contrasting the hypothesis of the half-space

model.

Theret's solution is reported in figures 5.8 and 5.9 with a dashed blue line, in contrast with our continuum model and previous studies by Baaijens et al.(Baaijens et al., 2005). When a compressible material is adopted, the need for a computational approach to catch cell biomechanics during MPA emerges. In agreement with Baaijens' predictions, our results for a single cell, modelled with only cytoplasm as a homogeneous compressible material, revealed a non-linear variation of the aspiration length (L_p) when increasing the applied negative pressure.

The influence of cell and micropipette diameters (D_c and D_p respectively) was also investigated, by varying one or both in the range D_c/D_p from 1.5 to 5.5 (figure 5.10). As reported in previous works(Baaijens et al., 2005; Zhou et al., 2005), differences in problem size (i.e., the ratio D_c/D_p) appear to strongly modify L_p; results also highlighted that the parameter which governs this behaviour is not only D_c or D_p but rather the ratio D_c/D_p. Figure 5.10 reports the aspiration lengths of different combinations of D_c/D_p, normalized by the cell radius instead of the micropipette one, since it usually may vary between cells. This visualization allows us to clearly identify the differences by varying D_c/D_p, in agreement with other proposed models in the literature.

When the CTM was used also to model MPA, in order to evaluate possible variations in the final L_p, two cytoskeleton orientations were analysed, namely, configuration 1 and configuration 2 (figure 5.12). Slight oscillations with respect to the CM were observed between the two configurations, but some more evident changes arose when the ratio D_c/D_p decreased, meaning that a larger portion of the cell is subjected to the negative pressure applied by the pipette. These oscillations highlighted that also in the MPA the cytoskeleton plays a role and some configurations (e.g., configuration 2) entail a more significant tensegrity structure involvement (dotted light blue line in figure 5.13), thus supporting the previous insights obtained in the AFM simulations. Moreover, in MPA both CT and CTM were modelled with the same material parameters adopted in the AFM, thus validated, thanks also to the experimental comparison reported in figure 5.11.

These two applications of the CTM and the obtained results confirmed the great importance and advantages of considering the main cell subcomponents when modelling a single cell subjected to various mechanical stimuli. Even if the here presented model presents some limitations (such as the lack of connections between the nucleus and the other parts or the missing interactions of the cell with the substrate), it represents a step forward in understanding the differences between cell types from a mechanical point of view. In particular, with our model, it is possible to explore how a variation in the mechanical properties of a single subcomponent may affect the overall cell behaviour. Moreover, the main benefit of adopting a tensegrity structure is its potentiality in shape adaptation, a key feature to include when dealing with living cells.

In the present work, we proposed a computational model to mimic the biomechanical behaviour of living cells, starting from a continuum model, and then adopting a combined continuum-tensegrity approach in order to elucidate how a variation in the parameters of cell subcomponents may alter the global cell response. Being able to model this intrinsic variability is a key factor in cell mechanics since it is also associated with a different behaviour between healthy and tumour cells. The analysis of the here proposed CM with reference to other past results from the literature confirmed its applicability for these future purposes, while the outcomes of the CTM with respect to the CM underlined the non-negligible mechanical contributions of the cell subcomponents. In particular, the results highlighted that when a single cell is subjected to AFM indentation and micro-pipette aspiration (MPA) the cytoskeleton may strongly alter the overall cell biomechanics.

Indeed, these FE models represent a useful tool for the mechanical investigation of both living and cancer cells, revealing to be also a valuable steppingstone in the studies of the mechanical processes that undergo during the different stages of tumour cells and to overcome the complexity in studying the neoplasms, in particular when referring to the inter and intra tumour variability.

6 Bendo-tensergity model of the cell

As described in chapter 4, some researchers have highlighted the need to introduce the bendability of microtubules in their models in order to completely capture the real behaviour of the cytoskeleton(Fraldi et al., 2019; Bansod et al., 2018).

The model presented in chapter 5 can be easily updated to introduce bendability in the microtubules by changing the description of these components from the previously used truss elements to beam elements able to bend.

In the realm of FEM both beam and truss elements are usually employed to describe slender structures such as the microtubules and the microfilaments of a cell. While truss elements are a simple and effective way to model structures with axial forces along their length, beam elements stand apart due to their added capability of capturing bending behaviour, an essential characteristic absent in truss elements. This critical distinction arises from the inherent design of beam elements these elements do not only consider geometric properties and material characteristics but also account for the cross-sectional area and second moment of area, enabling accurate representation of bending deformations under various loads.

In structural mechanics, the bending stiffness of a beam is described as a combination of its geometrical characteristics (by means of its second moment of area) and its mechanical properties (the elastic modulus in the case of a linear elastic beam).

Earlier we described the microtubule as having a constant cross-sectional area of 190 nm^2 and having a full circular profile. This simplification is usually enough for representing the microtubule as a truss in most simulations but if we are to describe its bendability we need to refer to the actual geometry of the microtubules in order to preserve this quantity and represent it with the right level of accuracy.

In the work of Jiang et al.(Jiang, Jiang, Posner, & Vogt, 2008), the authors described the geometry of microtubules by taking into consideration its structure made of 13 protofilaments enveloped on one another in a spiral fashion. Their work came to describe the microtubule as shaped as a hollow circular pipe having an internal radius of 7.7 nm and an outer radius of 12.5 nm. Such geometry has been used and implemented in Abaqus to create microtubules with an appropriate bending stiffness.

6.1 Notes on bending stiffness

As hinted earlier, the bending stiffness is linked to the stiffness of a beam and its second moment of area. This quantity is used to link the bending moment M applied to a beam and the resulting curvature κ by means of:

$$M = B_t\kappa = EI\kappa \tag{6}$$

Where E is the Young's modulus of the beam (assuming linear elastic behaviour) and I is the second moment of area of the beam.

This relationship comprises the role of the bending stiffness. The higher B_t is the more the beam will resist the bending moment by causing a lower level of curvature. It is worth mentioning that B_t does not necessarily have to be constant through the beam's length while it will be treated as such in this work since microtubules tend to have a homogeneous cross-section.

The second moment of area is a quantity that describes the distribution of points in an area with respect to an axis. The general formula to calculate it is:

$$I_{AA'} = \int \int_R \rho^2 dA \tag{7}$$

Where AA' is a generic axis perpendicular to the region of interest R and ρ is the distance of an infinitesimal area from the axis AA'.

In the case of a circular hollow profile like the one of microtubules, the second moment of are is described as:

$$I = \frac{\pi}{4}\left(r_1^4 - r_2^4\right) \tag{8}$$

Where r_1 is the external radius of the circular ring and r_2 is the internal one.

In the case of a full circular profile, the previous equation becomes:

$$I = \frac{\pi}{4} r^4 \tag{9}$$

Applying the equations presented to a full circular profile for the microtubule using a cross-sectional area of 190 nm^2 we would get a bending stiffness of about $B_t = 3.45e-24$ $N \cdot m^2$ while if we are to calculate the same quantity using the geometry provided by Jiang et al. we would get a value of $B_t = 1.97 - 23\ N \cdot m^2$ which is in line with previous reports Gittes et al.(Gittes, Mickey, Nettleton, & Howard, 1993) and Fraldi et al.(Fraldi et al., 2019).

6.2 Simulation results

The model presented in chapter 5 has been adapted to include bendable microtubules. As explained, this has been done by simply replacing the truss elements representing the microtubules with beams having a circular pipe cross section as the one described by Jiang et al.(Jiang et al., 2008). Each truss element has been replaced by 40 beam elements to obtain a better discretization of the bending curvature.

The model has been used to simulate both AFM indentation tests and MPA tests using the same boundary conditions used for the continuum tensegrity model as described in the previous chapter. In the following, the results of such analysis are discussed and

interpreted.

6.2.1 AFM indentation

When performing indentation tests on the new model, it is possible to observe some small bending on the microtubules as depicted in figure 6.1. It is worth noting that the indentation performed on this model does cause only a slight bending which is not apparent without scaling the deformation of the model to a factor of x50.

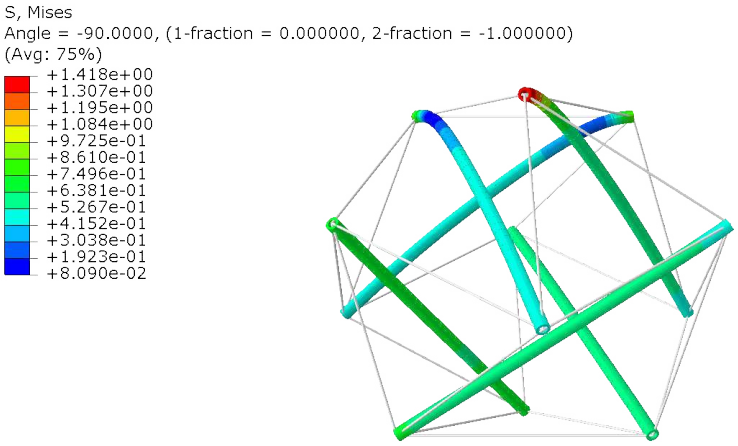

Figure 6.1: Structure of the cytoskeleton at the end of the loading phase. The results are obtained by running the continuum-tensegrity model with bendable microtubules. The deformations are scaled by a factor of x50 to better visualize the bending of the microtubules.

The mechanical response of the model doesn't appear to be significantly affected by the presence of bendable microtubules as depicted in figures 6.2 and 6.3. Only in the case of the smaller indenter tip, we can see a slight discrepancy between the two models probably due to the fact that the smaller indenter tip is better able to interact with the cytoskeletal structure thus increasing the effect of the change in the microtubules behaviour.

The difference between the results of the AFM simulations using bending or non-bending elements with a small indenter ($R = 2.5\mu m$) is 5% at its peak. Such a small value can be regarded as non-significant, especially considering the wide range of mechanical responses found in the literature due to the intra-tumour variability.

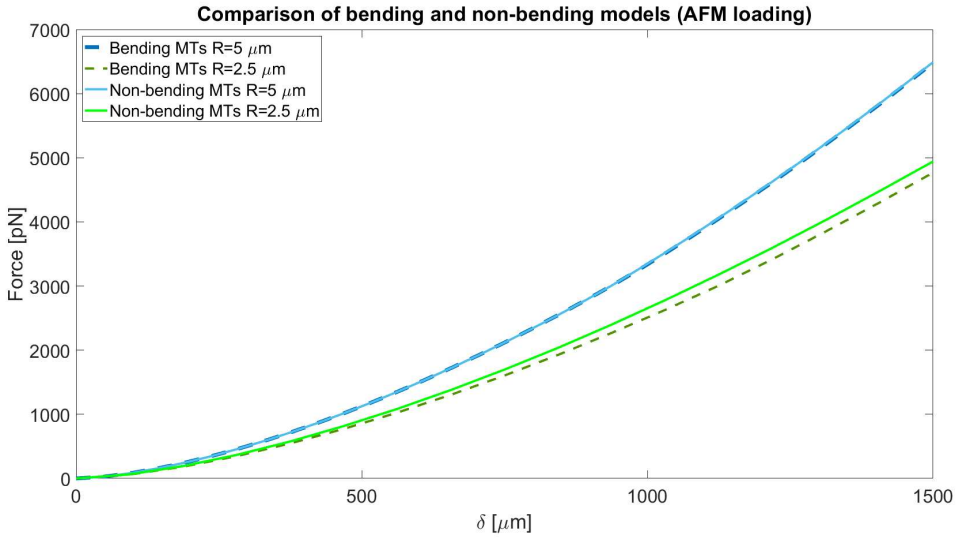

Figure 6.2: Comparison of the results for the loading phase of the AFM simulations using a model with bendable microtubules compared to a model with non-bendable microtubules. Results are obtained for indentation with a spherical indenter of radius $R = 5\mu m$ or $R = 2.5\mu m$.

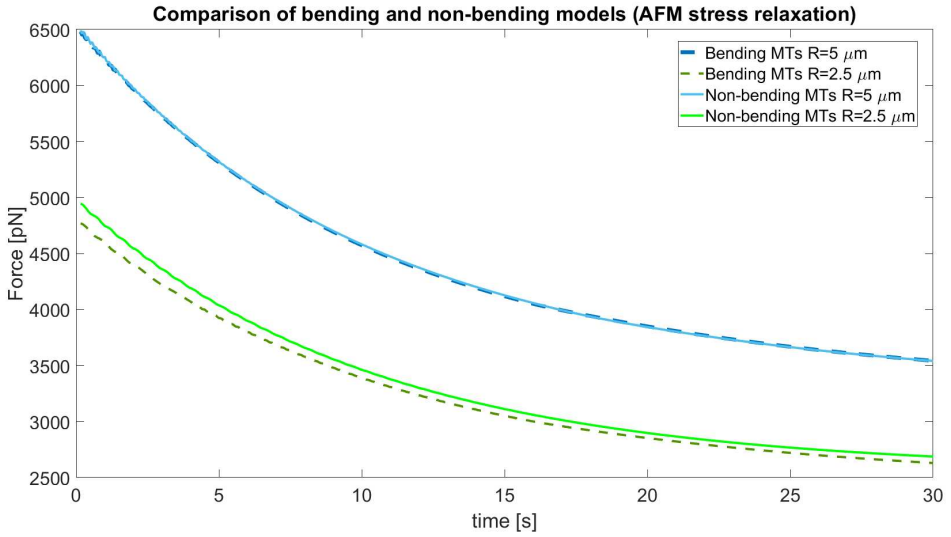

Figure 6.3: Comparison of the results for the stress relaxation phase of the AFM simulations using a model with bendable microtubules compared to a model with non-bendable microtubules. Results are obtained for indentation with a spherical indenter of radius $R = 5\mu m$ or $R = 2.5\mu m$.

6.2.2 MPA simulations

In the case of micropipette aspiration tests, the bending behaviour of the microtubules is more evident as depicted in figures 6.4. In this case, no scaling factor is required to observe the bending of the elements composing the cytoskeletal structure. This more

accentuated bending behaviour is due to the compressive action of the micropipette on the cell model.

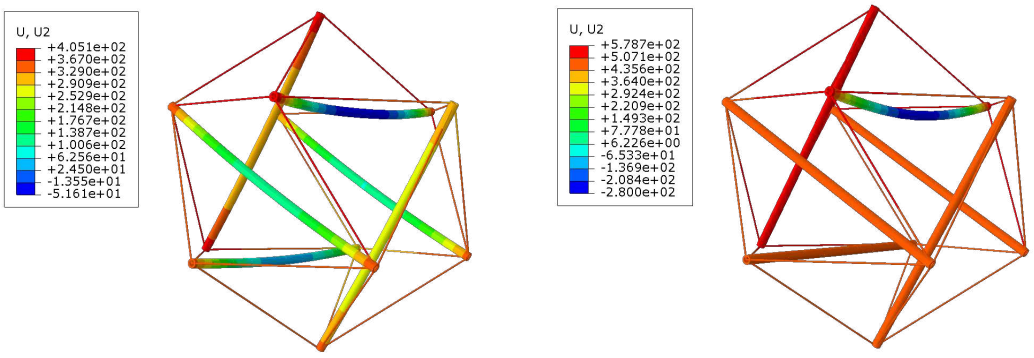

(a) Loading phase (b) Creep phase

Figure 6.4: Bending behaviour of the microtubules in different phases of the micropipette aspiration simulations. No scaling factor has been used for this case.

The difference between the bending and non-bending CT models is not significant, for both the loading (figure 6.5) and creep phases (figure 6.6).

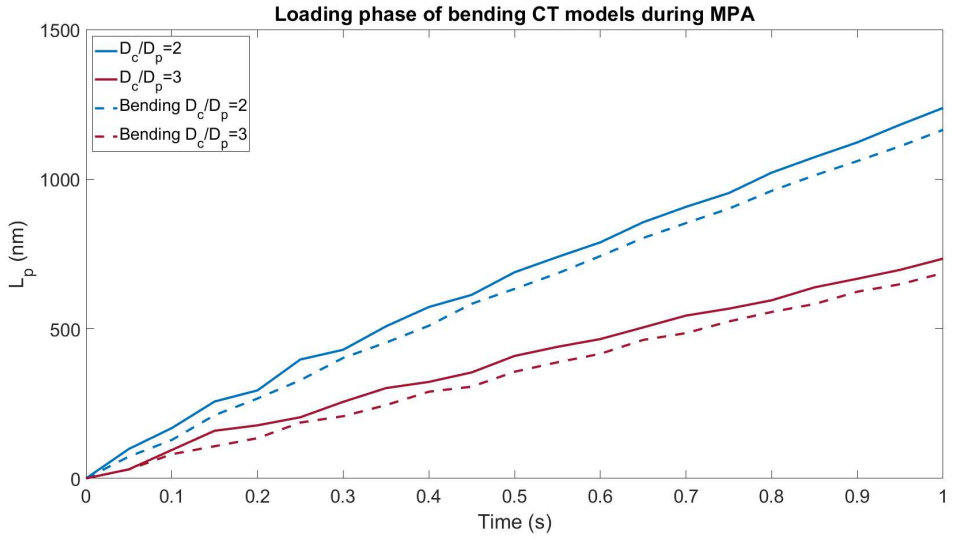

Figure 6.5: Comparison of the results for the loading phase of the AFM simulations using a model with bendable microtubules compared to a model with non-bendable microtubules. Results are obtained for indentation with a spherical indenter of radius $R = 5\mu m$ or $R = 2.5\mu m$.

The main difference is found between the presence or absence of the cytoskeletal structure itself as can be seen in figure 6.6. This difference is attributed to the fact that the cytoskeleton acts as an obstacle thus causing the cell to require a higher pressure to reach the same amount of total displacement. It is worth reminding that in this model the microtubules and microfilaments are not described as viscoelastic but rather

as simply linear elastic beams and trusses.

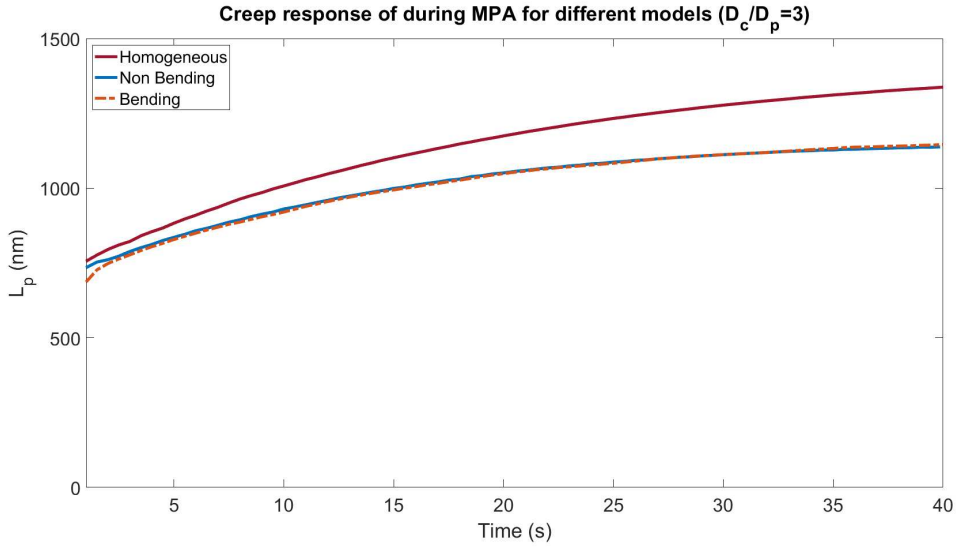

Figure 6.6: Comparison of the results for the stress relaxation phase of the AFM simulations using a model with bendable microtubules compared to a model with non-bendable microtubules. Results are obtained for indentation with a spherical indenter of radius $R = 5\mu m$ or $R = 2.5\mu m$.

As seen, the presence of a cytoskeleton with bending microtubules produces results similar to the ones obtained using the simple continuum-tensegrity model. This fact underlines how both models are accurate in representing the global response of the cell while still retaining part of the complexity of the cell subcomponents. Depending on the scope of the analysis, each model can be used to faithfully represent the overall behaviour of both tumour and healthy cells.

7 Cell growth models

The models presented so far are very good in passively representing the mechanical response of the cell but lack the ability to take into account the adaptability of cells to their environment.

As already discussed in chapter 1 the cell is able to adjust its volume by controlling the amount of water and ions present inside of it. This ability is fundamental for sustaining normal physiological behaviour and is usually impaired or altered when a cell develops a pathological state. For example, potassium channels have been linked to the capacity of tumour cells to resist apoptosis(Gao et al., 2011).

The volume of the cell is known to be linked to the osmotic pressure differences between the cytosol and the extracellular environment as well as to the changes in internal and external hydrostatic pressure.

Some promising analytical models have been developed throughout the years to describe the complex system that regulates the changes in the volume of the cell. One of the most prominent works in this regard is the model developed by Hongyuan Jiang and Sean X. Sun (Jiang & Sun, 2013).

7.1 The Jiang-Sun model

The model developed by Jiang and Sun starts from the assumption that the volume occupied by a cell is mainly due to the amount of water present inside it. This assumption is fairly accurate as discussed in chapter 1. For this reason, investigating the factors that can influence the flow of water across the membrane is the same as evaluating the rate of change of the volume itself.

As said, the flow of water is linked to the hydrostatic and osmotic pressures and for this reason the authors described the change in volume as related to a quantity called the chemical potential of water:

$$\Psi = P - \Pi \tag{10}$$

Where P represents the hydrostatic pressure and Π is the osmotic pressure. By defining these quantities inside and outside the cell it is possible to describe the flow of water as:

$$J_{water} = -\alpha \Delta \Psi = -\alpha(\Psi_{in} - \Psi_{out}) \tag{11}$$

For simplicity, the authors assumed the cell to occupy a spherical volume and thus linked the flow of water to the change in the cell's radius:

$$\frac{dr}{dt} = J_{water} = -\alpha \Delta \Psi = -\alpha(\Delta P - \Delta \Pi) \tag{12}$$

Where $\Delta P = P_{in} - P_{out}$ and $\Delta \Pi = \Pi_{in} - \Pi_{out}$. With this simple equation, it is possible

to adjust the speed at which the cell adapts its volume in response to environmental stresses by adjusting the parameter α related to the permeability of the cell membrane.

With this description of the volume change, the authors investigated the role of the 4 variables present in the model: Π_{in}, Π_{out}, P_{in} and P_{out}. The authors assumed the external osmotic pressure and the external hydrostatic pressure to be constant in general. This hypothesis is fairly acceptable in most cases although it should be taken out when dealing with drastic changes such as the ones experienced by chondrocytes (increase in the overall hydrostatic pressure due to cartilage compression) and in tumour cells (local fluctuations of the osmotic pressures due to rapid biological activity). This hypothesis leaves out the values of Π_{in} and P_{in} as the main variables in controlling the change in the volume of the cell.

The osmotic pressure inside the cell is related to the number of ions dissolved in the cytosol. Ions can flow in and out of the cell by means of different pumps and channels that can either be passive or active. The permeability of these channels, together with the osmotic pressure gradient, allows the description of the flow of ions through the membrane. In this model, only one species of ion is used and effects such as electroneutrality are not considered in describing the flow of ions. Both aspects are reported to not be significant for the overall model reliability.

The authors included two types of ion transporters in their model: mechanosensitive channels (MS) and active pumps.

MS channels are used to describe the overall mechanical response due to all kinds of mechanosensitive channels present on the cell membrane. These types of channels open in response to an increase in stress at the cell membrane being closed below a threshold of cortical tension and progressively opening as the stress increases. In actuality, when MS channels open they allow an influx of calcium ions which in turn open up other channels and pumps thus providing a net efflux of ions and a decrease in the internal osmotic pressure. For simplicity, the authors described these ion channels as to be causing an efflux of ions.

The authors describe the probability of opening of MS channels as a Boltzmann function P_{open} which is set to 0 when the cortical stress is below a threshold value σ_c, 1 if the stress is equal or greater to a saturating stress σ_s and evolving linearly between these two values. Assuming the presence of N MS channels the authors describe the ion flux due to MS channels as proportional to $NP_{open}\Delta c/h_0$ where Δc is the concentration gradient of ions and h_0 is the membrane thickness. This description allows to write the following equations to describe the flux of ions due to MS channels:

$$J_1 = \begin{cases} 0 & \text{if } \sigma \leq \sigma_c \\ -\beta(\sigma - \sigma_c)\Delta\Pi & \text{if } \sigma_c < \sigma < \sigma_s \\ -\beta(\sigma_s - \sigma_c)\Delta\Pi & \text{if } \sigma \geq \sigma_s \end{cases} \tag{13}$$

Where β is a rate constant. Note that in this case the proportionality with $\Delta c/h_0$ has been replaced with the osmotic pressure difference since $\Delta\Pi = RT\Delta c$ (with R being the gas constant and T the current absolute temperature) and having the constants R, T and h_0 absorbed in the rate constant β. As mentioned by the authors, the flux of ions described in equation 13 can be directed both ways depending on the sign of the osmotic pressure difference $\Delta\Pi$.

Active pumps work against the concentration gradient to pump ions inside the cell. In order to do this the cell needs to consume energy in the form of ATP hydrolysis. The authors describe the change in the free-energy due to the pumping action as $\Delta G = RTlog(c_{in}/c_{out}) - \Delta G_a$. Since in most cases the relationship $c_{in} > c_{out}$ holds true, this process needs an energy source (depicted as ΔG_a in the equation) in order to become favourable.

Taking all of this into account, the flux of ions due to the activity of active pumps can be described as $J_2 = -\gamma'\Delta G$ with γ' being a general permeation constant. This formulation can be further simplified assuming that the concentration of ions inside and outside the cell is in the same order of magnitude ($c_{in} - c_{out} \ll c_{in}$) and applying a Taylor expansion. All of this leads to a more usable and practical equation:

$$J_2 = \gamma(\Delta\Pi_c - \Delta\Pi) \tag{14}$$

Where γ is a constant and $\Delta\Pi_c$ is a critical osmotic pressure obtained by posing $\Delta G = 0$. Generally, the term $\Delta\Pi_c$ shouldn't be used as a constant but rather as a function of the external osmotic pressure but since the author mostly worked assuming a constant external osmotic pressure the term can be considered constant as well. When the authors tested a version of the model in which the term $\Delta\Pi_c$ was dependent on the external osmotic pressure they noticed a very small difference in the overall response of the model to external stimuli.

Having described the flux of these two types of channels, it is possible to describe the overall change in the number of ions inside the cell as:

$$\frac{dn}{dt} = 4\pi r^2(J_1 + J_2) \tag{15}$$

Two parameters are left to be defined: the hydrostatic pressure and the cortical stress. The authors did not specify what model was used to compute the hydrostatic pressure inside the cell but it is fair to assume that it was calculated using the thin-wall pressure vessel approach applied to a sphere. This model allows us to relate the hydrostatic pressure inside of a thin-wall vessel to the normal stresses on the surface of the sphere as:

$$\sigma = \frac{pr}{2t} \tag{16}$$

Where σ is the cortical stress, p is the hydrostatic pressure, r is the radius of the

spherical pressure vessel and finally t is the thickness of the thin wall (which in this case is the cell membrane). For the cortical stress, the authors considered using a general viscoelastic model in the form of:

$$\sigma = \frac{K}{2}\left(\frac{S}{S_0} - 1\right) + \eta\frac{1}{S}\frac{dS}{dt} - \sigma_a \tag{17}$$

Where K is the Young's modulus of the cortex, S is the current surface of the sphere, S_0 is the reference surface of the sphere, η is the viscosity of the cortex and σ_a is the active component of the stress due to the contraction of myosin motors. Although this formulation is the most complete, the authors showed that the viscous part of the equation is negligible to the overall response. Taking into account the spherical geometry assumed for this model, the authors further simplified the previous equation leading to:

$$\sigma = \frac{K}{2}\left(\frac{r^2}{r_0^2} - 1\right) - \sigma_a \tag{18}$$

Where r is the current radius of the cell and r_0 is the reference radius.

In table 9 are reported the values of the parameters identified by the authors.

Symbol	Parameter and unit	Value reported
h	Thickness of the cortical layer (μm)	0.5
K	Young's modulus of the cortical layer (kPa)	6
σ_a	Active stress due to myosin motors (Pa)	-100
σ_c	Threshold stress of the MS channels (Pa)	300
σ_s	Satuarting stress of the MS channels (Pa)	900
$\Delta\Pi_c$	Critical osmotic pressure difference of the ion pumps (GPa)	30
r_0	Reference cell radius (μm)	8
Π_{out}	Osmotic pressure outside the cell (MPa)	0.5
α	Rate of water transport ($m \cdot s^{-1} \cdot Pa^{-1}$)	10^{-9}
γ	Rate of ion flux across active pumps ($mol \cdot m^{-2} \cdot s^{-1} \cdot Pa^{-1}$)	10^{-17}
β	Rate of ion flux across MS channels ($mol \cdot m^{-2} \cdot s^{-1} \cdot Pa^{-2}$)	2×10^{-11}

Table 9: Values of the parameters used in the work of Jiang and Sun (Jiang & Sun, 2013). The parameters refer to a general cell.

The authors tested the model and found that, in physiological conditions, it is able to reach a dynamic steady state in accordance with what is known regarding the pump-leak concept widely accepted in the literature. Furthermore, the authors tested and confirmed the ability of the model to represent the cell's volume adaptation in response to both hypertonic and hypotonic osmotic shocks.

7.2 The McEvoy model

McEvoy et al. developed a more complex model that uses most of what has been already described for the Jiang-Sun model with the addition of a few elements (McEvoy et al., 2020).

For example, the authors linked the flow of water across the membrane to both osmotic pressure difference and hydrostatic pressure difference but also to the surface area of the cell as well leading to:

$$\frac{dV}{dt} = -AL_{p,m}(\Delta P - \Delta\Pi) \tag{19}$$

Where A is the surface area of the cell and $L_{p,m}$ is the permeability to water of the membrane. The dependency on the area rises from the fact that a cell having a bigger surface area will be able to exchange more water with the outside both as simple diffusion through the membrane and because of a greater number of aquaporins present on the membrane.

The flux of ions through the MS channels is still described by a picewise linear equation $\dot{n}_{ms} = -\omega_{ms}(\sigma)\Delta\Pi$ where the permeability coefficient $\omega_{ms}(\sigma)$ is described by:

$$\omega_{ms}(\sigma) = \begin{cases} 0 & \text{if } \sigma \leq \sigma_c \\ \beta(\sigma - \sigma_c) & \text{if } \sigma_c < \sigma < \sigma_s \\ \beta(\sigma_s - \sigma_c) & \text{if } \sigma \geq \sigma_s \end{cases} \tag{20}$$

Similarly, the flux of ions through the active pumps is still described as:

$$\dot{n}_p = \gamma(\Delta\Pi_c - \Delta\Pi) \tag{21}$$

The authors introduced a new set of channels referred to as leak channels which are assumed to be always open and thus always allowing a flux of ions in the same direction as the concentration gradient. These channels have a constant permeability and their flux is proportional to the osmotic pressure difference:

$$\dot{n}_l = \omega_l\Delta\Pi \tag{22}$$

Where ω_l is the permeability of the leak channels.

Putting together equations 20, 21 and 22 we can derive the total flux of ions as:

$$\frac{dN}{dt} = -A((\omega_{ms}(\sigma) + \omega_l + \gamma)\Delta\Pi - \gamma\Delta\Pi_c) \tag{23}$$

The values of the parameters identified for this model are reported in table 10.

Finally, it is worth mentioning that the authors also analysed the role of gap junctions in cell clusters and spheroids. Gap junctions (GJs) are structures that permit the exchange of water and ions between cells. Their role is very important in modulating the volume of cells that are part of a cluster creating volume gradients that can boost the cells' ability to modulate their size in response to environmental and biological aspects. Since this work focuses on single cells, the behaviour of GJs will not be reported here.

Symbol	Parameter and unit	Value reported
h	Thickness of the cortical layer (μm)	0.6
K	Young's modulus of the cortical layer (kPa)	6
σ_a	Active stress due to myosin motors (Pa)	100
σ_c	Threshold stress of the MS channels (Pa)	75
σ_s	Satuarting stress of the MS channels (Pa)	600
$\Delta\Pi_c$	Critical osmotic pressure difference of the ion pumps (GPa)	40
r_0	Reference cell radius (μm)	7.1
Π_{ext}	Osmotic pressure outside the cell (MPa)	0.67
$L_{p,m}$	Rate of water transport ($m \cdot s^{-1} \cdot Pa^{-1}$)	7×10^{-12}
γ	Rate of ion flux across active pumps ($mol \cdot m^{-2} \cdot s^{-1} \cdot Pa^{-1}$)	2.25×10^{-17}
β	Rate of ion flux across MS channels ($mol \cdot m^{-2} \cdot s^{-1} \cdot Pa^{-2}$)	2×10^{-11}
ω_l	Rate of ion flux across leak channels ($mol \cdot m^{-2} \cdot s^{-1} \cdot Pa^{-1}$)	1.5×10^{-9}

Table 10: Values of the parameters used in the work of McEvoy (McEvoy et al., 2020).

7.3 Sensitivity analysis

In order to better understand the analytical model proposed by McEvoy et al.(McEvoy et al., 2020), a Matlab code implementing the model for a spherical cell has been developed.

Some boundary conditions have been given to the model to obtain a steady state solution. If we are to observe the model's equations (especially equation 21) it becomes easy to realize that the model will reach a steady state with a dynamic equilibrium. Even if we are to impose $\Delta\Pi = 0$ and $\Delta P = 0$ thus stopping the flow of water, the active pumps will inevitably cause an increase in the internal osmotic pressure thus disrupting the equilibrium and causing an increase in the volume of the cell until the following conditions are met simultaneously:

$$\gamma\Delta\Pi_c = (\gamma + \omega_{ms} + \omega_l)\Delta\Pi \tag{24}$$

$$\Delta\Psi = \Delta P - \Delta\Pi = 0 \tag{25}$$

This means that according to the model, a cell in a resting steady state is continuously subjected to both an osmotic pressure difference and a hydrostatic pressure difference by having both internal hydrostatic pressure and osmotic pressure higher than the ones of the surrounding environment. This is confirmed by some findings in the literature regarding the hydrostatic pressure and osmotic pressure levels inside the cell(S. Liu et al., 2019).

Thus, given a set of parameters like the ones presented in table 10 it would be possible to impose a dynamic steady state with the condition:

$$\Delta P = \Delta\Pi = \frac{\gamma\Delta\Pi_c}{\gamma + \omega_{ms} + \omega_l} \tag{26}$$

In order to better understand the behaviour of the model and the role of each of the subcomponents, a thorough sensitivity analysis of the model parameters is performed.

Observing that the values of $\Delta\Pi$ and ΔP at steady state are usually around 100 Pa(Jiang & Sun, 2013; McEvoy et al., 2020), an initial condition of $\Delta P = \Delta\Pi = 0$ was adopted in the analytical model in order to create an unstable condition that would allow us to observe the transient phase of the model. It is finally worth mentioning that the conditions here described do not depend on the geometry of the cell but do not consider the presence of external mechanical stresses that could alter the final value of the internal hydrostatic pressure.

In figure 7.1 it is possible to observe the evolution of some of the variables of interest for the McEvoy model in a model where the initial condition is given by $\Delta P = \Delta\Pi = 0$ and the values of the model's constants are given by table 10.

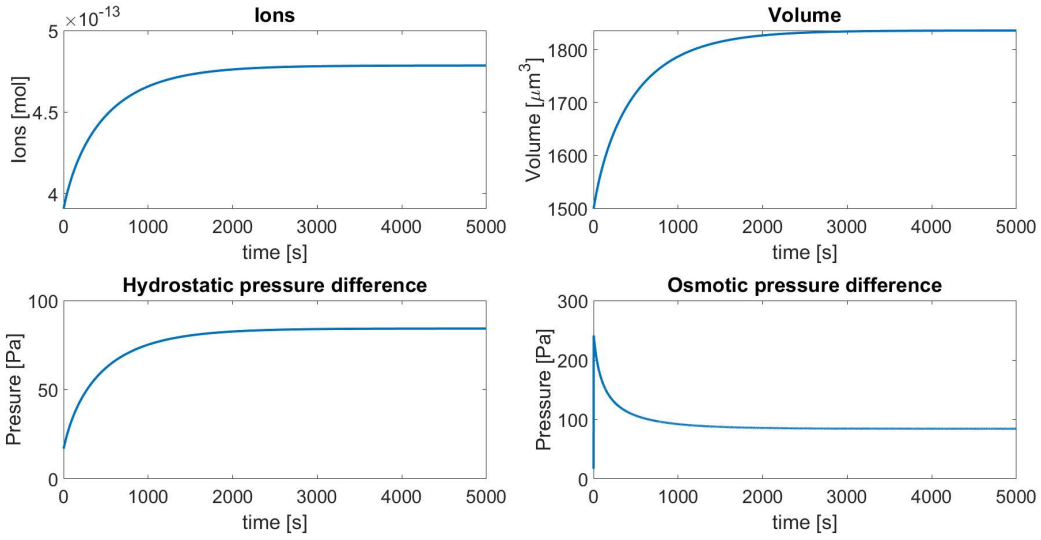

Figure 7.1: Curves obtained with the Matlab implementation of the McEvoy model using the parameters provided in table 10.

These results are comparable to the ones obtained by Jiang et al.(Jiang & Sun, 2013) where they assessed that in their analytical results, the steady state values for the hydrostatic and osmotic pressure differences are about 100 Pa. The lower values obtained in this case are to be expected since this model includes leakage channels.

7.3.1 Change in membrane permeability to water

The equation regulating the volume of the cell has only one constant $L_{p,m}$. This value represents the permeability of the membrane to water as well as the amount of water that flows through aquaporins (and by that the number of aquaporins present on the cell membrane).

By changing the value of this parameter we can change the behaviour of the system as reported in figures 7.2, 7.3 and 7.4.

An increase of $L_{p,m}$ by one order of magnitude (figure 7.2 causes many changes in the

speed and transient phase of the model. Not only the model reaches the dynamic steady state more quickly (about 3 times faster from about 30 minutes to 10 minutes) but the initial overshoot of the osmotic pressure difference is no more present as well.

A further increase of $L_{p,m}$ does not cause a similarly significant change in the behaviour of the model (figure 7.3). In this case, the model reaches its steady state in less than 10 minutes but the most significant difference is the fact that the osmotic pressure difference doesn't show an initial abrupt change but rather a regular increase similar to what is experienced by the hydrostatic pressure difference.

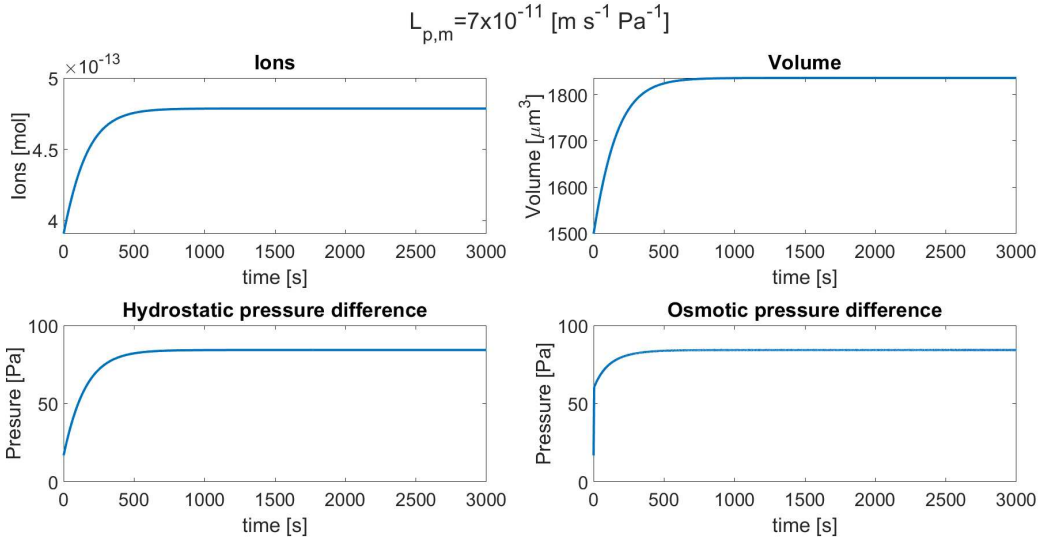

Figure 7.2: Curves obtained by increasing the membrane water permeability ($L_{p,m}$) by one order of magnitude with respect to the value of table 10.

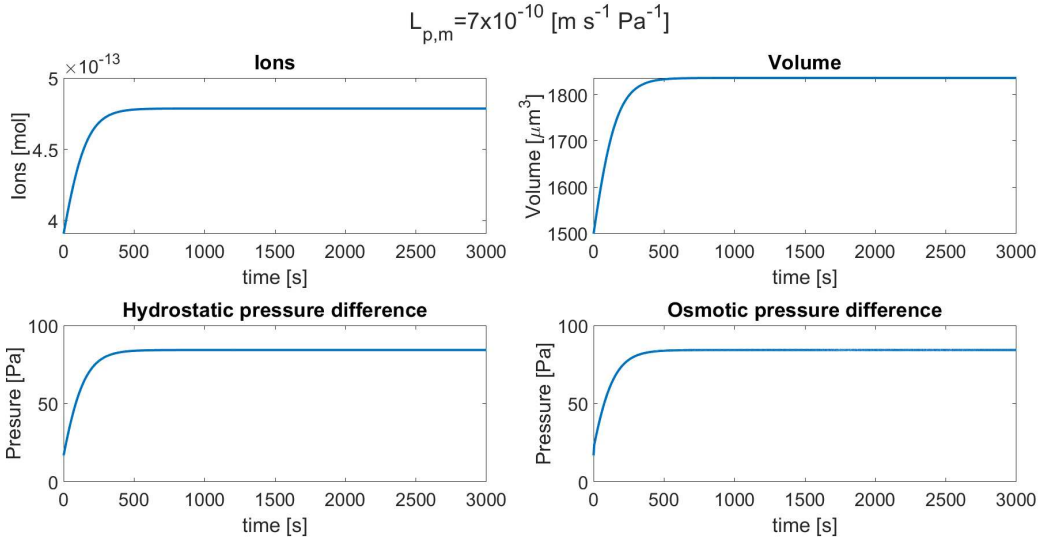

Figure 7.3: Curves obtained by increasing the membrane water permeability ($L_{p,m}$) by two orders of magnitude with respect to the value of table 10.

On the other hand, if $L_{p,m}$ is to be decreased by one order of magnitude (figure 7.4) the model appears to need about 250 minutes to reach a steady state and the maximum value of the osmotic pressure difference initial spike becomes around 400 Pa.

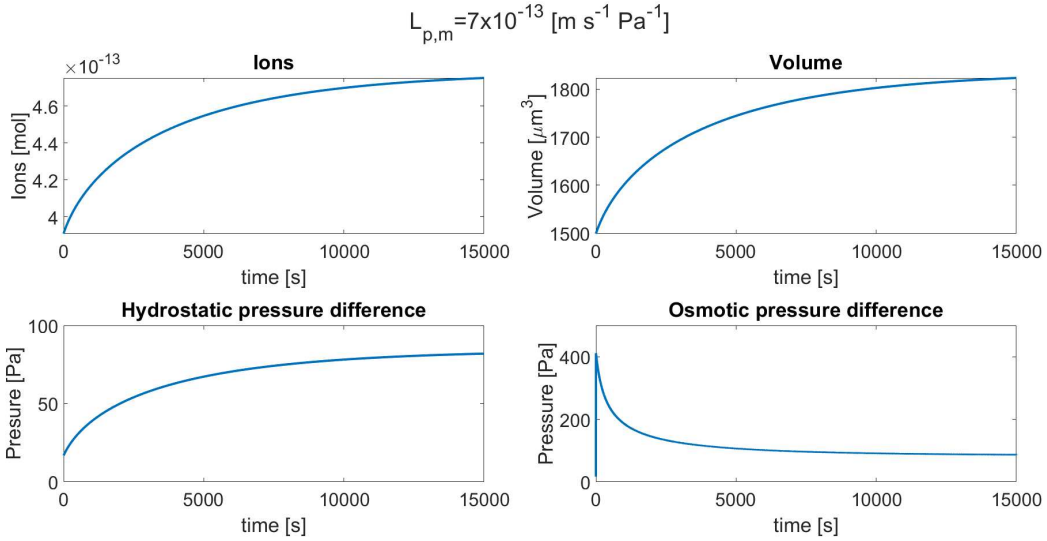

Figure 7.4: Curves obtained by decreasing the membrane water permeability ($L_{p,m}$) by one order of magnitude with respect to the value of table 10.

As expected, changes in the value of the water permeability of the plasma membrane mostly appear to regulate the speed at which the model reaches the steady state as well as its capability to oppose osmotic shocks. On the other hand, these changes do not influence the steady state values since the $L_{p,m}$ parameter of equation 19 does not change the steady state condition described earlier.

7.3.2 Changes in proteins' permeability to ions

Another important regulator of the model is the permeability of each of the membrane proteins to ion flow.

In figures 7.5 and 7.6 it is possible to observe the different effects of changing the permeability parameter ω_l of the leakage channels.

An increase of ω_l by one order of magnitude translates into a lower steady state value for hydrostatic and osmotic pressure differences. This is to be expected since a stronger flux of ions in the direction of the osmotic pressure gradient will be better able to contrast the activity of the ion pumps. This is further stressed by the reduction in the maximum overshoot of the initial osmotic pressure difference. Since the external osmotic pressure Π_{ext} is assumed constant, a lower $\Delta\Pi$ translates to a lower internal osmotic pressure and thus a lower final volume.

A reduction in the value of ω_l by one order of magnitude (figure 7.6 does not provide significant differences. The final volume, number of ions and pressure differences all

reach slightly higher resting values but the effect is not particularly significant. This shows that the role of the leakage channels is not particularly important to the overall model. Furthermore, this aspect was to be expected since the results obtained are not remarkably dissimilar from the ones of Jiang et al. where these proteins were not considered.

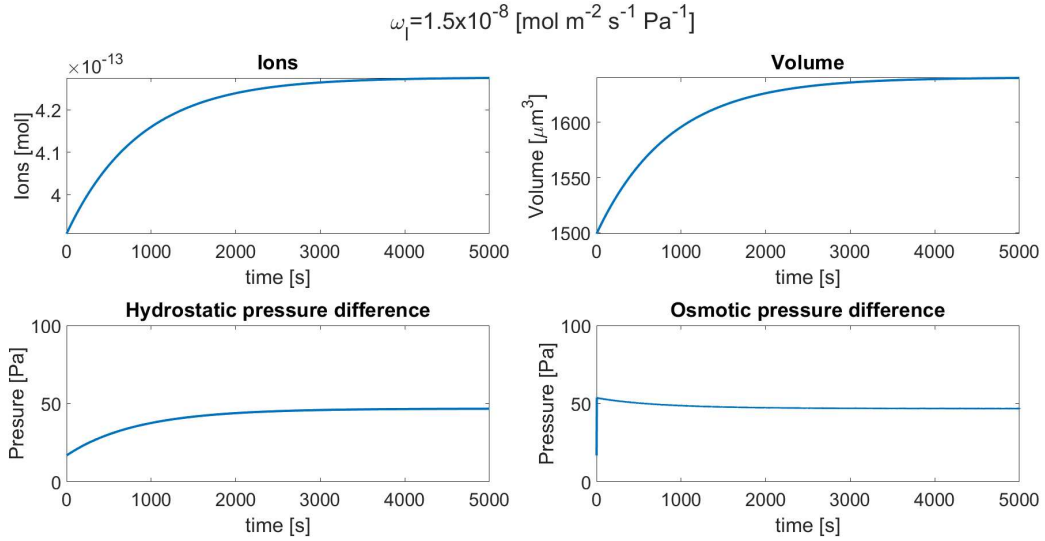

Figure 7.5: Curves obtained by increasing the permeability of leakage channels (ω_l) by one order of magnitude with respect to the value of table 10.

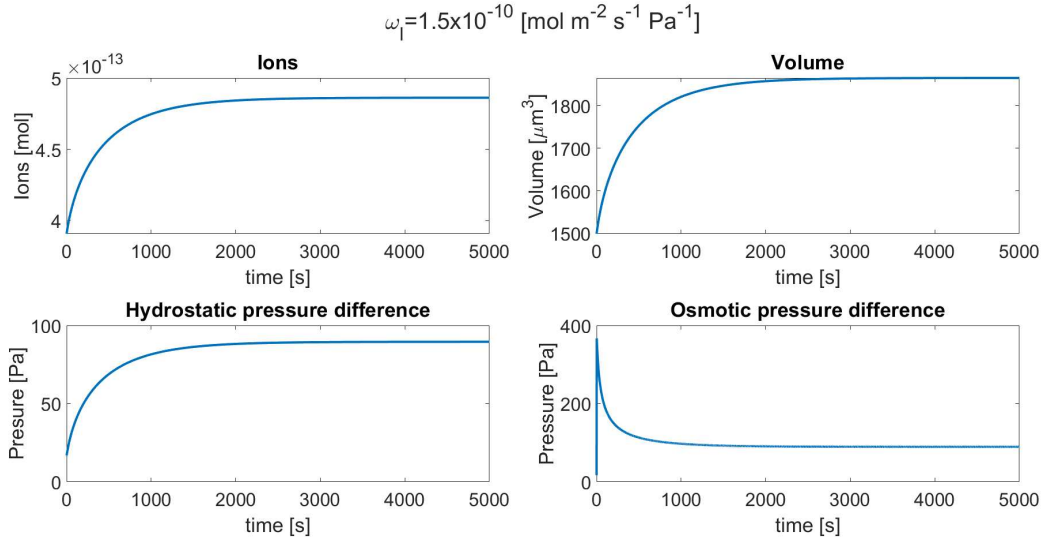

Figure 7.6: Curves obtained by decreasing the permeability of leakage channels (ω_l) by one order of magnitude with respect to the value of table 10.

Finally, it is worth pointing out that changes in the permeability of leakage channels do not translate into a significant change in the time needed to reach the dynamic steady state. This is expected as we observed that the speed at which the model reaches the

steady state is mostly regulated by the value of $L_{p,m}$.

In Figures 7.7 and 7.8 can be seen the changes in the model behaviour when changing the value of the permeability of active pumps.

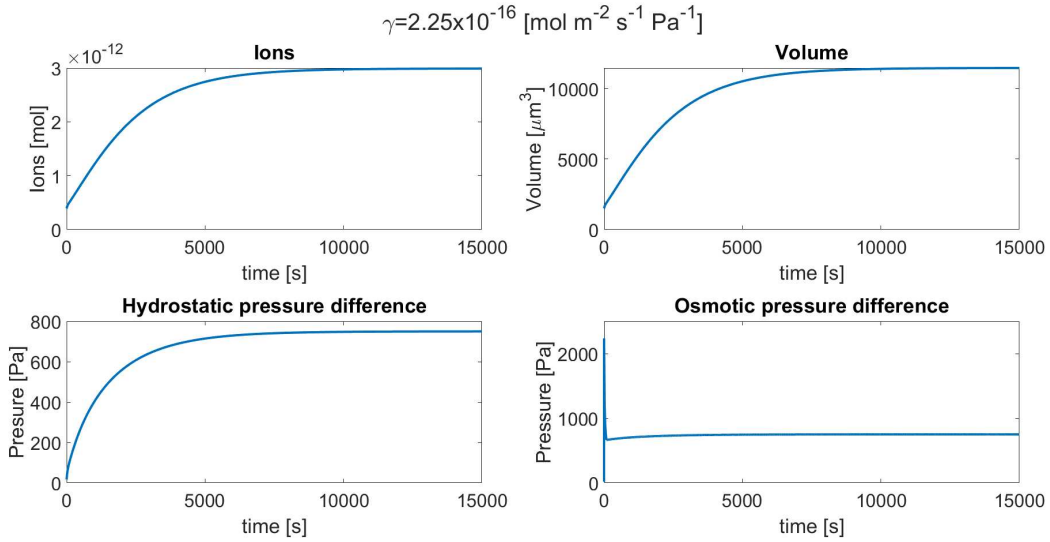

Figure 7.7: Curves obtained by increasing the permeability of active pumps (γ) by one order of magnitude with respect to the value of table 10.

Increasing the permeability of the active pumps γ significantly impacts the steady state values of all the output variables. Since the active pumps are the main factor in disrupting the initial condition $\Delta\Pi = \Delta P = 0$, an increased permeability will cause a greater influx of ions and thus the effects shown in figure 7.7.

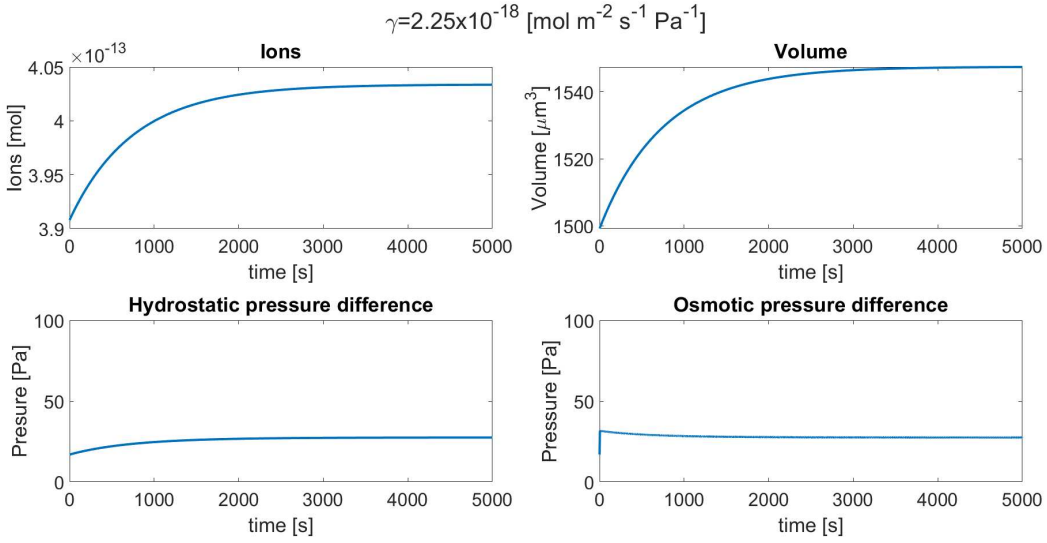

Figure 7.8: Curves obtained by decreasing the permeability of active pumps (γ) by one order of magnitude with respect to the value of table 10.

Decreasing the value of γ, on the other hand, reduces the disrupting capability of the active pumps thus causing lower resting values overall. Once again, the effect of the changes in the permeability of the active pumps affects significantly more the final resting values than the speed at which such values are reached.

In figures 7.9 and 7.10 it is possible to observe the effect of changing the permeability of mechanosensitive channels.

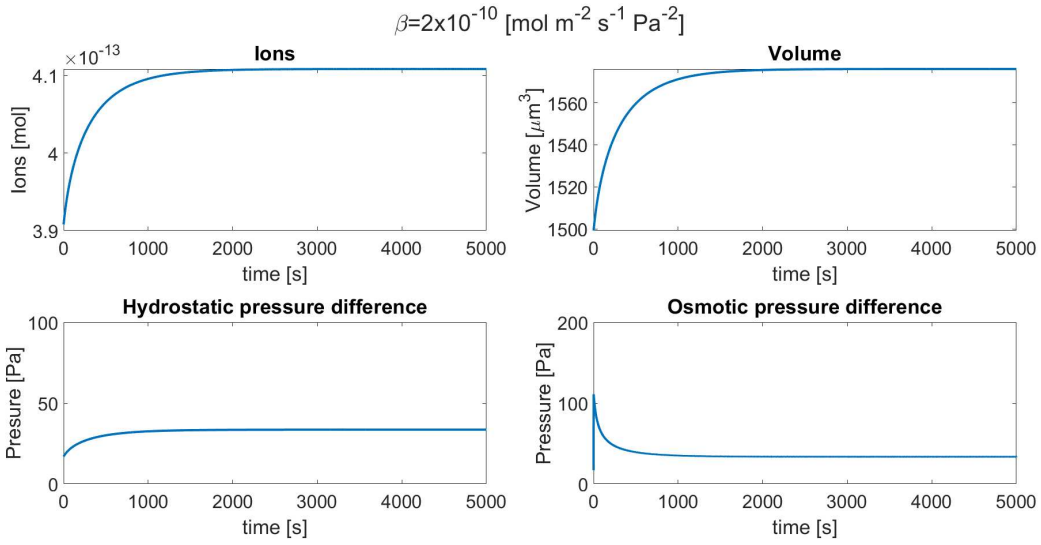

Figure 7.9: Curves obtained by increasing the permeability of mechanosensitive channels (β) by one order of magnitude with respect to the value of table 10.

Similar to what was observed for the leakage channels, an increase in the permeability of the mechanosensitive channels causes all the variables to set at a lower resting value. Interestingly, the mechanosensitive channels are not able to avoid the initial overshoot of the osmotic pressure difference as they need the threshold value of cortical stress (σ_c) to be achieved in order to start acting on the model.

Decreasing the value of β then causes an increase in the resting values of the model output variables as expected. A peculiar behaviour can be spotted in the osmotic pressure difference curve in figure 7.10: after the initial overshoot, the osmotic pressure difference decreases before starting to again grow towards the dynamic steady state value.

Further inspection of the model highlights the source of this behaviour: during the initial phase, the permeability of mechanosensitive channels is on the rise thus allowing (together with leakage channels and the leak portion of the active pumps) to contrast the influx caused by the active pumps. Once the mechanosensitive channels reach their saturation level, their ability to contrast the active pumps becomes challenged and the latter takes over thus causing a rise in the osmotic pressure difference.

Figure 7.11 displays a detail of the fluxes of ions at the moment of interest.

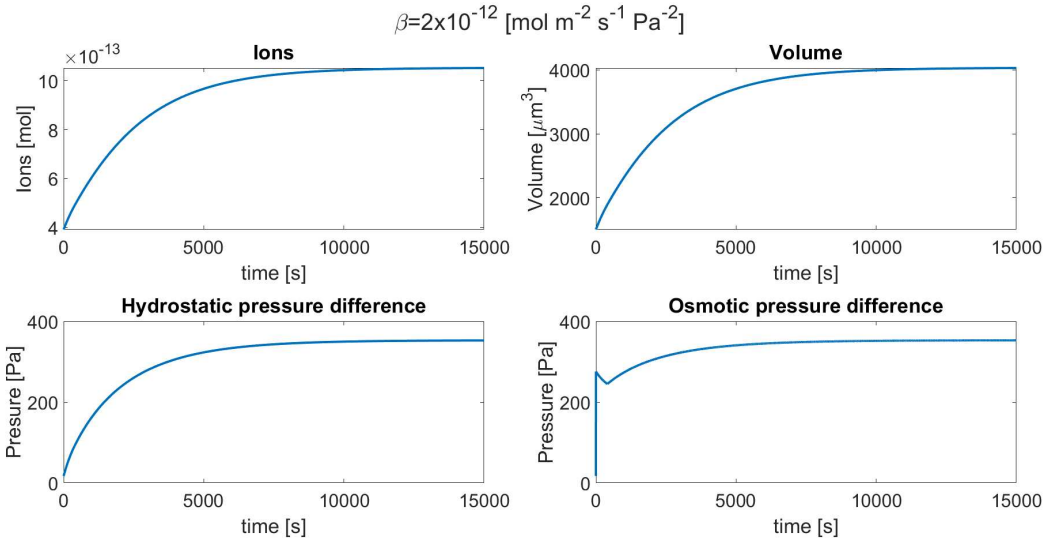

Figure 7.10: Curves obtained by decreasing the permeability of mechanosensitive channels (β) by one order of magnitude with respect to the value of table 10.

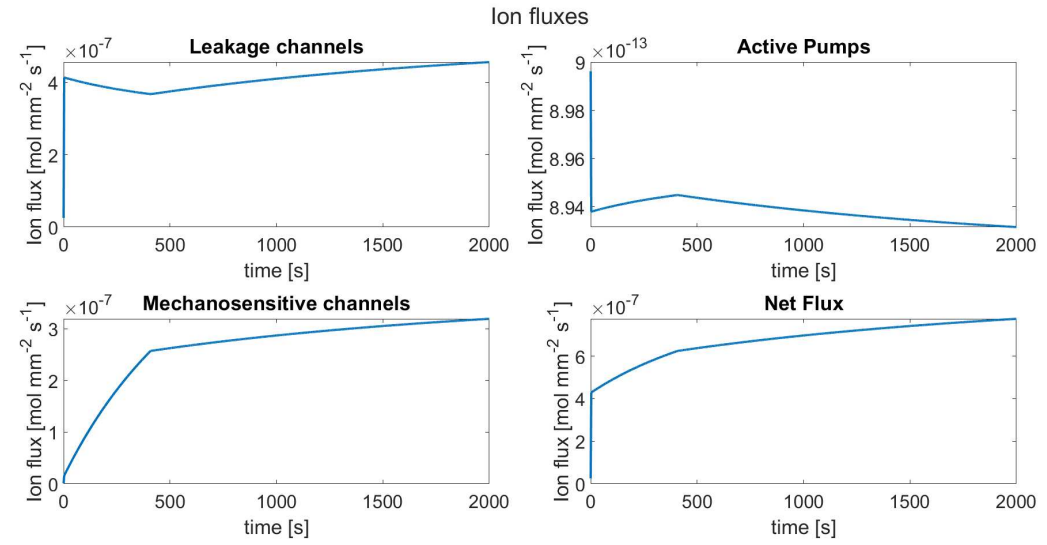

Figure 7.11: Ion fluxes due to the various membrane proteins during the simulation depicted in figure 7.10. At around 480 seconds it is possible to observe the change in the slope of all the fluxes due to the reach of the saturating stress by the mechanosensitive channels.

Finally, it is worth noting that the increase in the permeability of mechanosensitive channels does significantly reduce the length of the transient phase in the model. This is due to the fact that in this case, mechanosensitive channels are better able to oppose the pumping activity of the active pumps.

7.3.3 Changes in the cortical stress

Another interesting parameter that regulates the behaviour of the model is the rigidity of the cortical stress. This value can vary from cell to cell as explained in chapter 2. More interestingly, the stiffness of the cortical stress can be altered during certain pathological states such as cancer.

Figures 7.12 and 7.13 show the usual model outputs obtained by varying the cortical stiffness K.

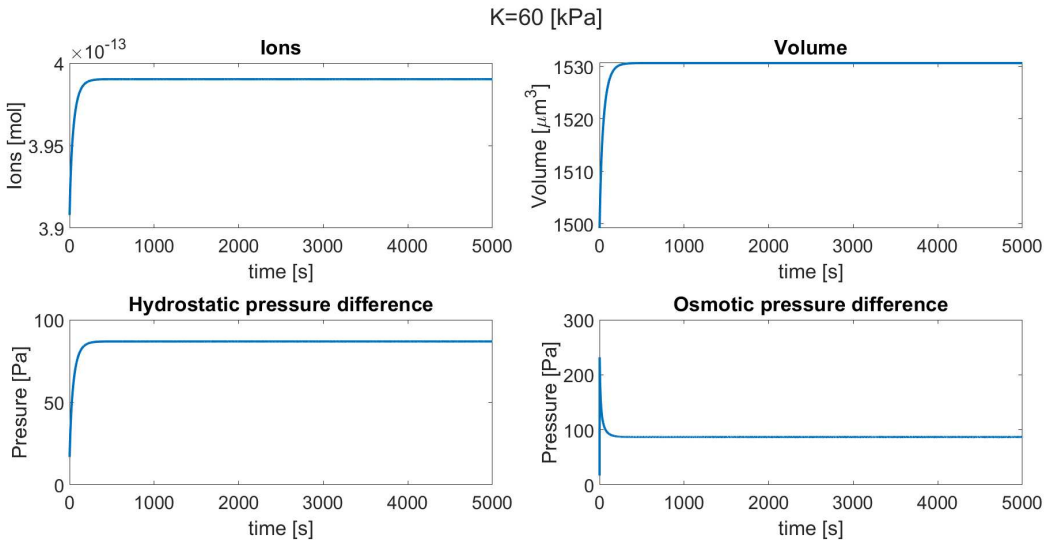

Figure 7.12: Curves obtained by increasing the stiffness of the cell membrane (K) by one order of magnitude with respect to the value of table 10.

A stiffer membrane translates to a higher hydrostatic pressure as more water is required to achieve higher volumes and for this reason, the final volume obtained in this case becomes significantly lower than the one of a membrane with the reference value of K reported in table 10. The final values of hydrostatic and osmotic pressure differences are mostly unaffected by this increase in stiffness showing a small increase due to the pumping system working on a lower volume. Another aspect that is significantly changed by the increase in stiffness is the duration of the transient phase. This is due to the fact that the rate at which internal hydrostatic pressure is accumulated is largely increased thus making it easier to reach the steady condition $\Delta\Pi = \Delta P$.

If the stiffness value is reduced, on the other hand, the model needs to employ a significantly longer transient phase in order to reach equilibrium. As depicted in figure 7.13, even after 14 hours the steady state is not reached. This is due to the long time needed to accumulate internal hydrostatic pressure since the more compliant membrane will be able to stretch more given the same amount of hydrostatic pressure. This, in turn, would make it so that the total amount of water needed to stop the growth would be significantly higher and thus the time needed to reach such a state (since the rate of

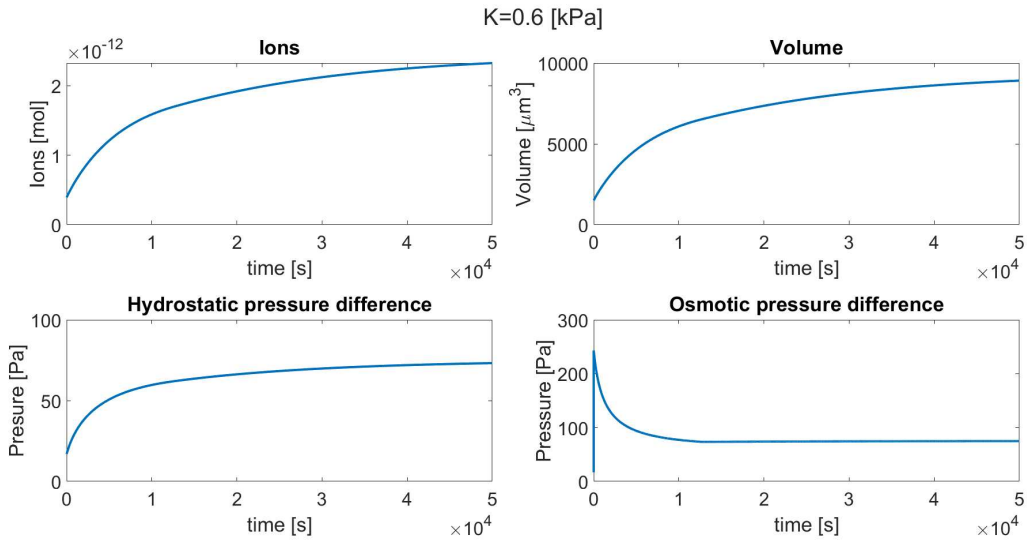

Figure 7.13: Curves obtained by decreasing the stiffness of the cell membrane (K) by one order of magnitude with respect to the value of table 10.

change in volume is mostly regulated by $L_{p,m}$).

These results show that the stiffness of the membrane K is another very significant factor in regulating the speed and final values of the model. This is extremely significant since it is known that the actin network and more specifically the actin cortex become loose and disorganized in cancer cells as previously described in chapter 2.

7.4 Osmotic pressure challenge

Jiang and Sun used their model to show how cells react to osmotic shocks(Jiang & Sun, 2013). The osmotic challenge is a typical experiment to observe the volumetric changes of a cell subjected to controlled changes in the osmotic pressure of the extracellular environment. These experiments allow us to observe the changes in volume and other parameters of interest when the cell is subjected to chemical stressors such as exposure to a hypotonic or hypertonic solution.

In their work, the authors simply changed the description of the external osmotic pressure from the constant value $\Pi_{ext} = 0.5$ to a more complex formulation thus creating the curves depicted in figure 7.14

The equations governing such curves would divide the time domain into three phases. The first phase is the steady state before the beginning of the osmotic challenge in which the osmotic pressure is kept constant at a value $\Pi_{ext} = \Pi_0$. During the second phase, the external osmotic pressure suddenly drops to a value $\Pi_{ext} = \Pi_1$ following the equation:

$$\Pi_{ext} = \Delta\Pi_0 \cdot e^{-\omega(t-t_0)} + \Pi_1 \tag{27}$$

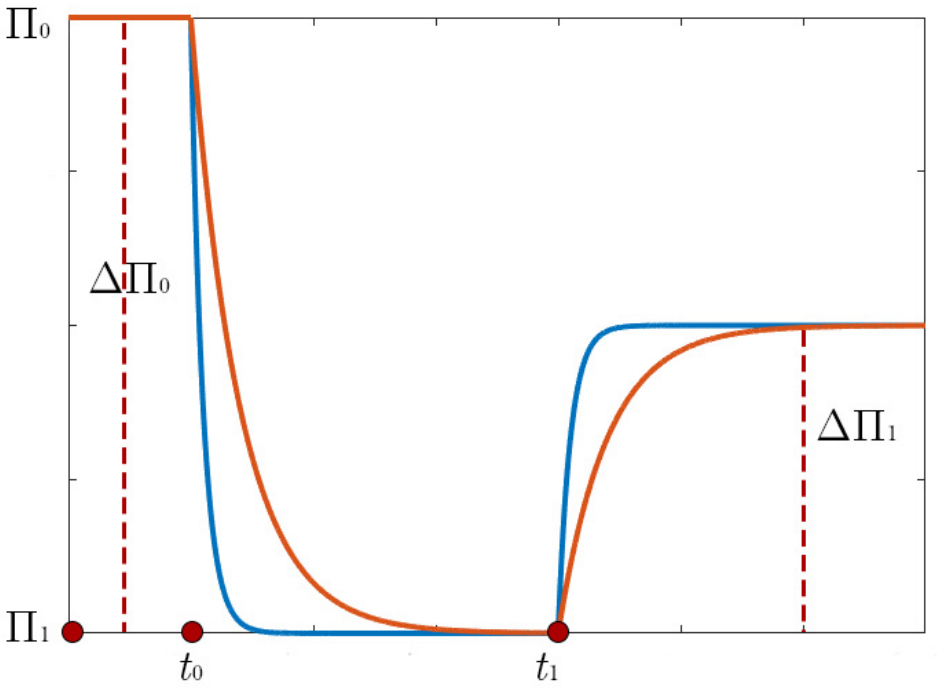

Figure 7.14: Examples of curves used to model the change in the external osmotic pressure to simulate an osmotic challenge.

Where $\Delta\Pi_0$ is the difference between the initial osmotic pressure and the hypotonic solution one, Π_1 is the hypotonic solution osmotic pressure, t_0 is the time at which the drop in osmotic pressure starts and ω is a rate constant which regulates the steepness of the curve.

Finally, the third phase is one in which the cell is again exposed to a solution with a higher content of solute described by the following equation:

$$\Pi_{ext} = \Delta\Pi_1 \left(1 - e^{-\omega(t-t_1)}\right) + \Pi_1 \tag{28}$$

Where $\Delta\Pi_1$ is the osmotic pressure difference between the hypotonic solution and the hypertonic one, t_1 is the time at which the rise in osmotic pressure starts and ω and Π_1 retain the same meaning as in the previous equation. Concerning the value of ω, this parameter acts so that the closer it is to 0 the more the curve will resemble a linear change in osmotic pressure while the higher it is the steeper and faster such change will be. With reference to figure 7.14, for example, the blue line has a value of ω four times higher than the one of the orange line.

Solving the analytical model for an osmotic challenge using the approach given by Jiang and Sun(Jiang & Sun, 2013) applied to the formulation given by McEvoy et al.(McEvoy et al., 2020) gives the results depicted in figure 7.15.

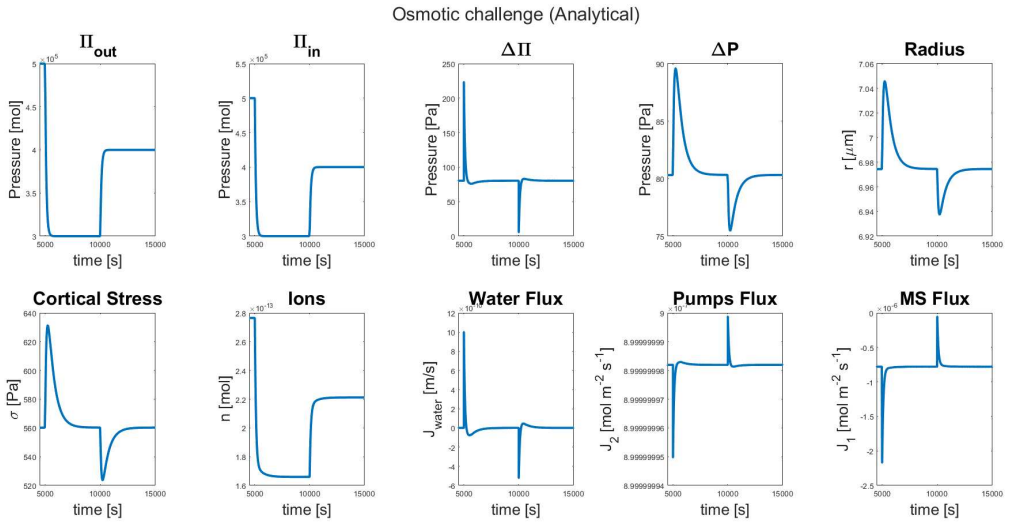

Figure 7.15: Curves representing the evolution of the main parameters from the model described by McEvoy et al. used to represent a cell undergoing an osmotic challenge. The external osmotic pressure Π_{ext} is used as the input signal in the model thus causing the evolution of the system.

It is worth observing that the resting radius of the model is not dependent on the external osmotic pressure and that the cell will always adjust its internal ion content to always end up with the same values for most quantities such as $\Delta\Pi$, ΔP, r, σ as well as the flux of ions through the cell membrane. This finding was already reported in the work of Jiang et al. where they also identified that the variables controlling the final resting radius for this model are $\Delta\Pi_c$, σ_c, σ_a, r_0, K, α, β and γ[3]. The authors identified the following equation as the one dictating the resting radius:

$$r_s = A_1 + sqrt(A_1^2 - A_2) \tag{29}$$

Where A_1 and A_2 can be expressed as:

$$A_1 = \frac{r_0(\gamma(\Delta\Pi_c r_0 - 2hK) + 2\beta hK(2K + 2\sigma_a + \sigma_c))}{4\beta hK^2}$$
$$A_2 = \frac{r_0^2(K + \sigma_a)(-\gamma + \beta(K + \sigma_a + \sigma_c))}{\beta K^2}$$

As mentioned earlier, this phenomenon is due to the decision to use a fixed value to represent the critical osmotic pressure $\Delta\Pi_c$ as a constant instead of accounting for its dependency on the external osmotic pressure Π_{ext}. The authors also pointed out that the effect of introducing such dependency is very small as a drop in the external osmotic pressure from 0.5 GPa to 0.3 GPa provides a change to the resting radius of about 10%.

[3]Parameters from the Jiang-Sun model from paragraph 7.1 and table 9.

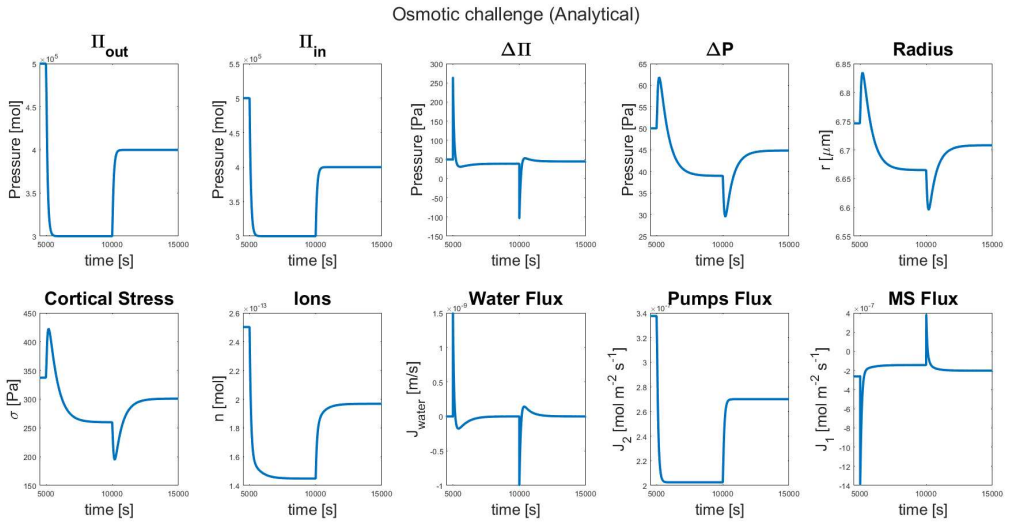

Figure 7.16: Curves representing the evolution of the main parameters from the model described by McEvoy et al. used to represent a cell undergoing an osmotic challenge. The critical osmotic pressure governing the flux of active pumps has been adapted to be dependent on the external osmotic pressure.

In figure 7.16 are reported the graphs relative to the osmotic challenge simulation using the model by McEvoy et al. in which the critical osmotic pressure is dependent on the external osmotic pressure using $\Delta\Pi_c = 3\Pi_{ext} \cdot 10^4$. The graphs illustrate small variations in the resting radius, osmotic pressure difference, and hydrostatic pressure difference. Notably, the baseline values of ion and water flux also undergo slight alterations, although they remain closely aligned with the original values, except for the flux through active pumps.

7.5 Impermeable biomass and biomass synthesis

An important characteristic of most cells is their ability to grow in size and mass during their lifetime to then divide into two identical cells. This behaviour is used to increase the number of cells in a population and sometimes to replace dead or faulty cells.

To create two identical copies, the cell needs to accumulate mass inside of it which is not expelled and that makes the total volume double the initial amount.

In this model, there is no initial amount of mass as the cell is considered at equilibrium with the initial conditions but it is still interesting to add a controlled signal in the model to simulate the production of mass during the cell cycle to achieve a final volume similar to what is found in adult cells ready for mitosis.

Since this model is not specific to any type of cell in particular, the work of Miettinen et Al.(Miettinen et al., 2022) has been used as a reference for an ideal volume goal.

In their work, the authors report the dry mass and dry mass density profiles for L1210 cells. L1210 cells belong to a cell line from the skin of a rat with lymphocytic leukaemia. The use of this type of cell as a reference for biomass synthesis is due to the paucity of robust data in the literature in this regard.

Figure 7.17 shows the dry mass and dry mass density profile of a wild-type L1210 cell during a cell cycle.

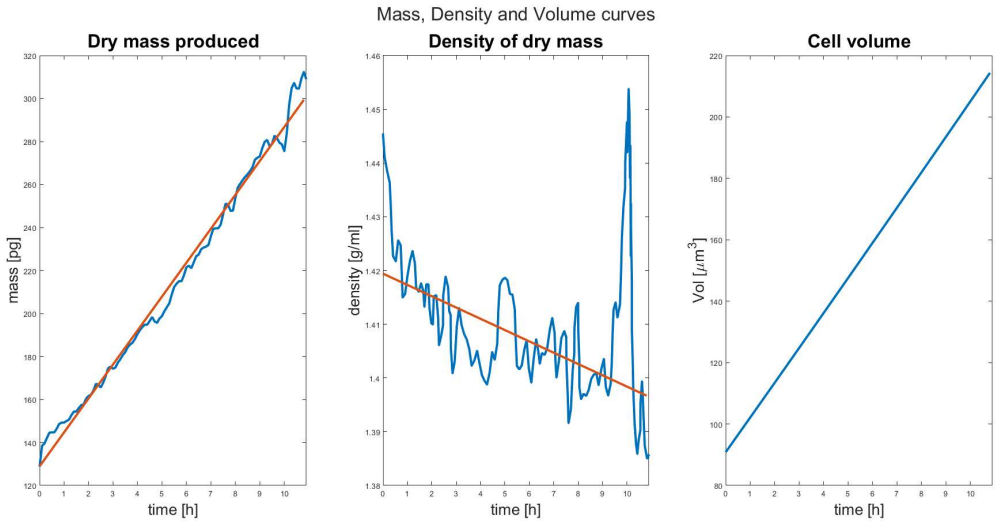

Figure 7.17: Dry mass, dry mass density and cell volume curves of a wild-type L1210 cell. The Volume curve is obtained by using a linear interpolated version of the dry mass and dry mass density curves from the work of Miettinen et Al.(Miettinen et al., 2022).

Having both the information regarding the mass and its density it is possible to calculate the volume curve (figure 7.17) using the relationship:

$$V(t) = m(t)/\rho(t)$$

Where $V(t)$ is the volume curve, $m(t)$ is the dry mass quantity and $\rho(t)$ is the density curve.

Having the volume curve it is possible to observe that for this cell the final volume is about 2.3604 the initial one.

To implement the presence of impermeable biomass in the model it is necessary to introduce a quantity n_{imp} representing the impermeable mass produced by the cell that cannot move through the cell membrane.

This quantity is then made to start at 0 until the cell reaches the steady state and then increase linearly until it reaches the maximum quantity required to go into mitosis. This quantity is represented in the model as moles for simplicity when having to deal with both the ions and biomass quantity.

The impermeable mass n_{imp} contributes to growth of the cell but does not interfere with the ion exchanges and thus the osmotic pressure inside the cell is divided into two parts: the osmotic pressure due to ions $\Pi_{in,I}$ and the one due to the biomass produced $\Pi_{in,B}$. The model remains largely unchanged but the osmotic pressure difference have to be rewritten as:

$$\Delta\Pi_{Ion} = \Pi_{in,I} - \Pi_{out}$$
$$\Delta\Pi_{Tot} = \Pi_{in,I} + \Pi_{in,B} - \Pi_{out}$$

Where $\Delta\Pi_{Ion}$ is the osmotic pressure difference due to the ions and $\Delta\Pi_{Tot}$ is the osmotic pressure difference due to both the ions and the impermeable biomass produced. Using this two variables it is possible to rewrite the ODEs as follow:

$$\frac{dV}{dt} = -AL_{p,m}(\Delta P - \Delta\Pi_{Tot})$$
$$\frac{dN}{dt} = -A((\omega_{ms}(\sigma) + \omega_l + \gamma)\Delta\Pi_{Ion} - \gamma\Delta\Pi_c)$$

With this new description of the model it is now possible to simulate the production of impermeable biomass in the model and its effect on the models' volume.

8 FE implementation of the Biomechanical model

Having a complete understanding of the models described in chapter 7, it was decided to implement such models using a custom Fortran code to be used in Abaqus CAE. The model implemented follows the description made by McEvoy et al.(McEvoy et al., 2020).

Since the model describes only two components (the cytoplasm and the actin cortex/cell membrane) the model has been built using only these two components. A simple spherical geometry has been adopted to represent the cell to be able to better compare the simulation results with the works of McEvoy et al. and Jiang and Sun(Jiang & Sun, 2013).

In order to build such a model, three custom subroutines have been developed. In this chapter we present the main reasoning behind the subroutines together with the results of the model's simulations while a more thorough description as well as the actual code used are listed in appendix A.

The custom Fortran code is composed of 3 main subroutines: a UMAT, a UVARM and a UEXTERNALDB.

The UMAT subroutine is used to describe the mechanical behaviour of the two parts comprised in this model. The cytoplasm has been described as a hyperelastic body with the same stiffness as the continuum model from chapter 5 but with an almost incompressible formulation. As mentioned earlier, the cell shouldn't be treated as an incompressible body when dealing with large timescales such as the ones used in the following simulations but since the volumetric change of the cell is described by the flux of water through the cell membrane, we can indeed treat the cell as having a Poisson's ratio of $\nu = 0.5$. The UMAT receives the volume increment calculated by the ODEs regulating the biomechanical model and the elements comprising the cytoplasm as subsequently expanded to reach the calculated final volume. Once the cell is expanded, the local values of hydrostatic pressure for each of the cytoplasm element is calculated and stored. The actin cortex, on the other hand, is described as being a linear elastic body with a Young Modulus of $E = 6\ kPa$ and a Poisson's ratio of $\nu = 0.3$. Furthermore, the UMAT calculates the average cortical stress of the actin cortex to be later used to calculate the opening of mechanosensitive channels. Finally, during the first iteration of the UMAT, the active component of the cortical stress due to the presence of myosin motors is added to the membrane's stress vector.

The UVARM subroutine is simply used to calculate the volume of each element composing the cytoplasm. During the first iteration, the value obtained is used to have a reference of the initial volume of the cell while during later iterations it can be used

to check if the UMAT correctly scaled the current volume to the right value or if some correction is needed.

Finally, the UEXTERNALDB gathers the local values of cortical stress, volume and hydrostatic pressure from the previous subroutines and uses them as inputs to a subroutine which solves the model's ODEs employing the Runge-Kutta method thus calculating the new internal osmotic pressure and volume of the cell which will be used in the next iteration of the code.

Using the FE approach allows the model to not be reliant on the theoretical models used to calculate the internal hydrostatic pressure and the cortical stress.

8.1 Transient phase simulations

The model has been used to simulate the transient phase from the initial condition $\Delta\Pi = \Delta P = 0$ to the dynamic steady state.

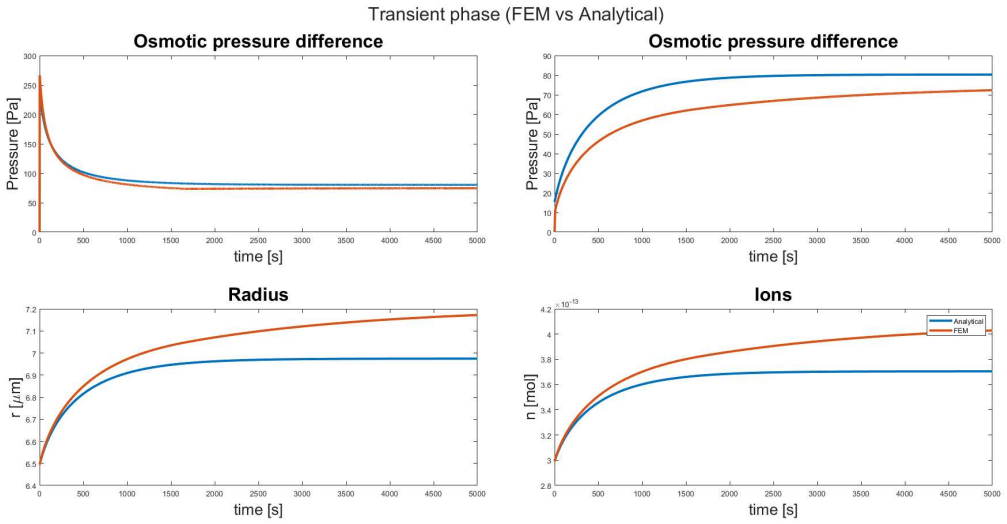

Figure 8.1: Curves representing the evolution of the main model's parameters. The Orange line represents the FE simulation results while the blue one represents the analytical solution.

The results of such simulation are presented in figure 8.1. As depicted in such figure, the analytical and FE models do not provide the same results growing more and more apart. The reason behind such discrepancy is the use of the thin-wall pressure vessel theory to calculate the internal hydrostatic pressure in the analytical model. This theoretical approach is valid as long as there are no deformations or infinitesimal ones but is not able to capture the evolution of the internal pressure as the cortex deformation becomes finite.

One way to overcome such a limitation is to use an empirical law to describe the evolution of the internal hydrostatic pressure. This can be obtained by simply fitting the internal

hydrostatic pressure values from the FE simulation against the volume data and using such fit to calculate the internal hydrostatic pressure values inside the analytical model.

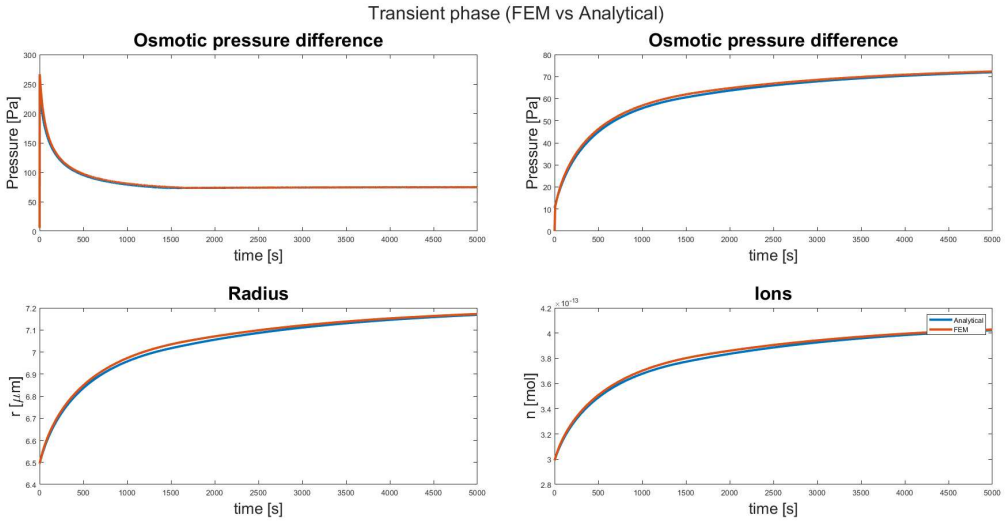

Figure 8.2: Curves representing the evolution of the main model's parameters. The Orange line represents the FE simulation results while the blue one represents the analytical solution.

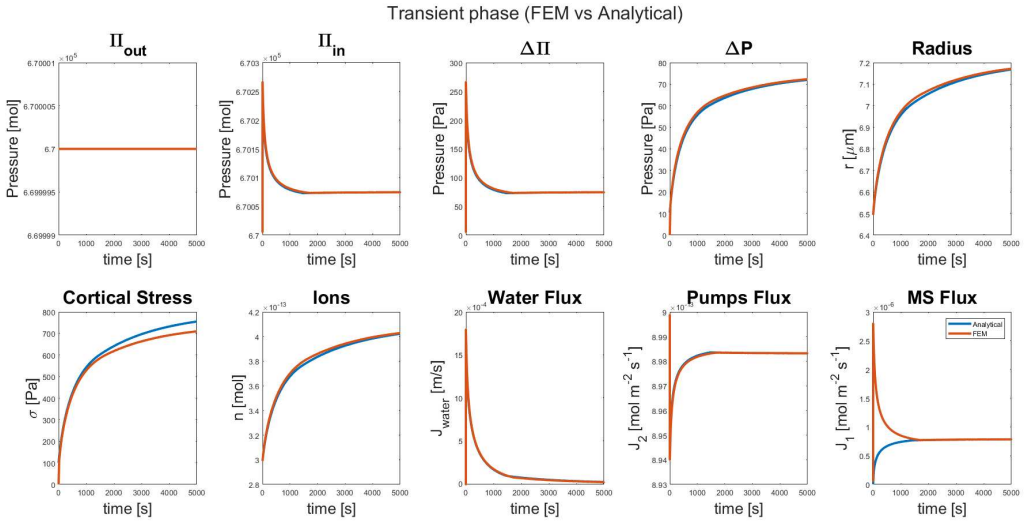

Figure 8.3: Curves representing the evolution of the main model's parameters. The Orange line represents the FE simulation results while the blue one represents the analytical solution.

Figures 8.2 and 8.3 show the evolution of the models' variable when adopting this new approach. It is clear that the use of an empirical fit to describe the evolution of the internal pressure in the model leads to much more agreement between the results of the two models.

Still, some differences can be spotted especially looking at the cortical stress trend. By the end of the simulation, the analytical approach seems to overestimate the amount of stress present on the membrane. This could be once again due to the fact that the analytical solution is an approximation of the real behaviour of the membrane.

8.2 Osmotic challenge simulations

As explained in the previous chapter, the osmotic challenge is an experiment very well suited to observing the response of the cell to external stressors such as changes in the external osmotic pressure. To implement the osmotic challenge, an accessory subroutine has been added to change the amount of external osmotic pressure during the simulation.

One problem arises when trying to describe the external osmotic pressure by using the formulation given in the previous chapter. Solving the set of ODEs for such rapid changes in the external osmotic pressure would require a very small time step during the steepest parts of the slope while larger ones can be used once the more unstable part is overcome. On the other hand, Abaqus does not check the goodness of the solution of the set of ODEs to move to a subsequent step automatically. Implementing a solution that takes that into account would require a deep understanding of the inputs and outputs of Abaqus signals. Furthermore, the solution should take into account strategies to adequately estimate the next time increment. Another strategy could involve the use of a very small time increment throughout the simulation but that would make the model very heavy computationally-wise and create space for more noise and numerical errors to occur. A simpler solution which is adequate for the scope of this thesis is to describe the external osmotic pressure as a piecewise linear equation such as the ones described in figure 8.4.

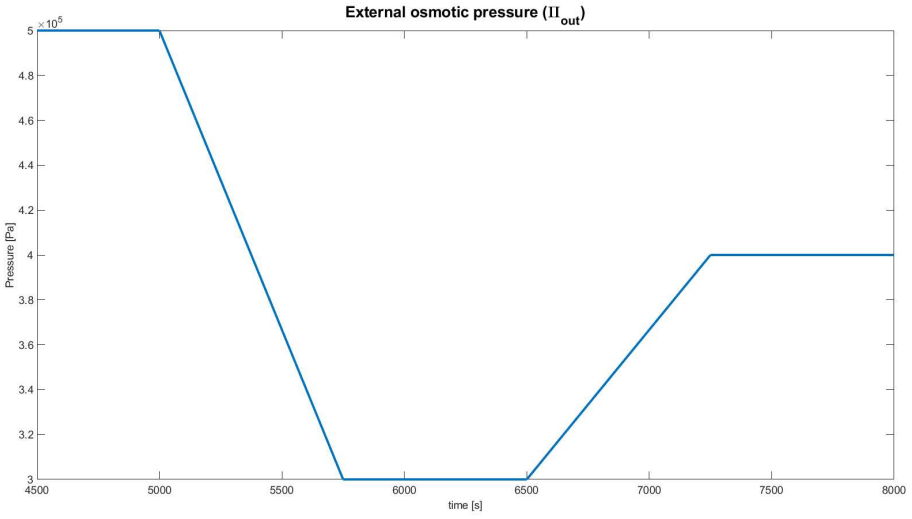

Figure 8.4: Pice-wise linear signal used to represent the evolution of the external osmotic pressure in the FE simulations of the biomechanical model.

This formulation divides the two phases of the osmotic challenge into two parts. Assuming that the hypotonic solution is introduced at a time t_0 and stays in contact with the cell until time t_1 then the total time in contact would be $t_{hypo} = t_1 - t_0$. During this time, the osmotic pressure will linearly decrease to the hypotonic value for $t_{hypo}/2$ of the time and then will rest at the hypotonic external osmotic pressure for the remaining $t_{hypo}/2$ of the time. The same approach is used to simulate the second phase in which the hypotonic solution is substituted by a hypertonic one. Similarly to what was done in the work of Jiand and Sun(Jiang & Sun, 2013), both steps have the same time length resulting in a slightly less steep curve for the second step.

Due to the presence of some outliers, the resulting data has been cleaned and both the original curves and the filtered versions are presented in figure 8.5

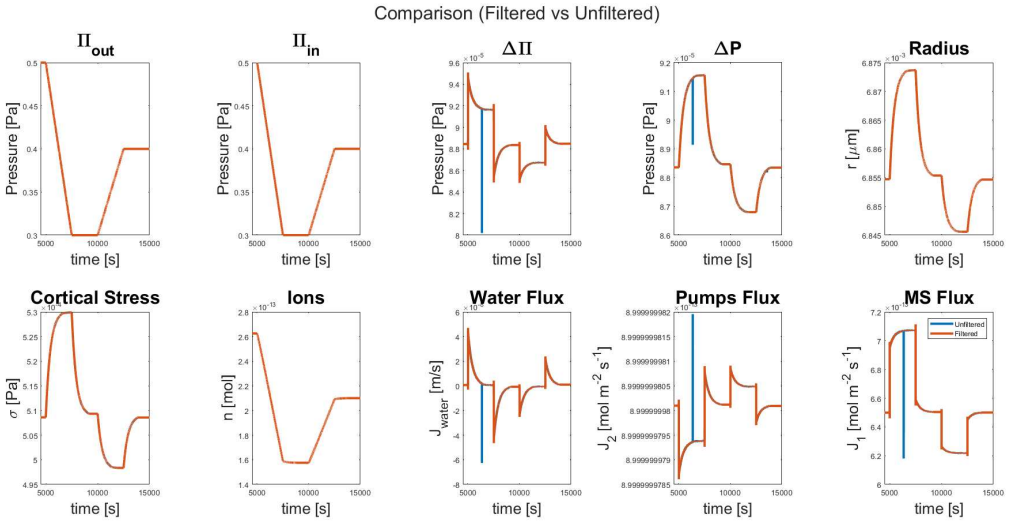

Figure 8.5: Results from the FE analysis of a cell undergoing osmotic challenge. Curves in blue are the raw data obtained from the FE analysis and the orange curves represent the filtered version.

The clean data from the numerical simulation have been compared to the analytical model. Once again, the internal hydrostatic pressure has been modelled using the same approach seen for the steady state solution. The resulting curves are presented in figures 8.6 and 8.7.

The analytical and FE solutions differ from one another, this is due to the the difference in cortical stress that was already noticed for the steady state problem. As explained earlier, this is due to the cortical stress being described by an approximate solution. It would be possible to use the same strategy that was adopted for the hydrostatic pressure and find an empirical law using the FE results but doing that would simply make it so that the mechanical part of the model would be completely calculated by the FE model. This shows one of the limitations of an analytical solution in comparison with the FE model here presented.

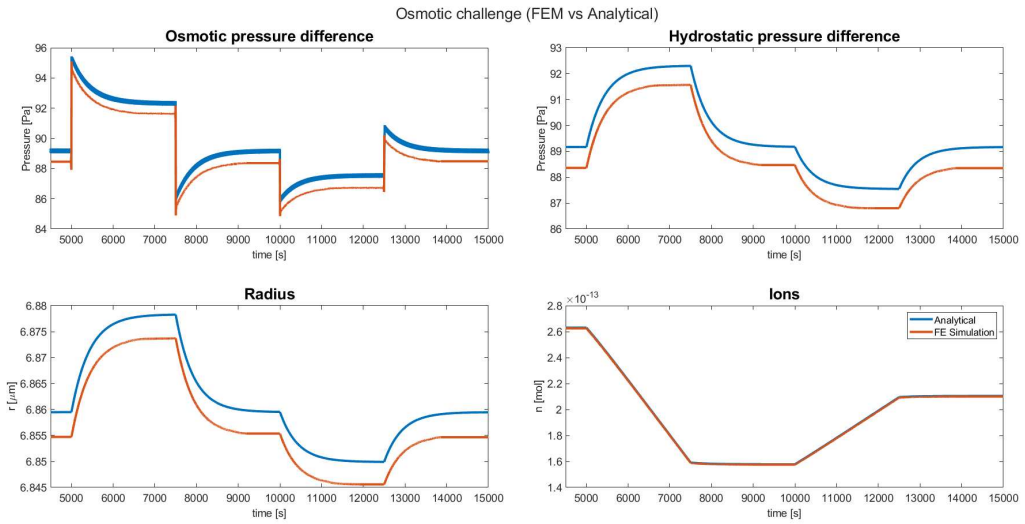

Figure 8.6: Curves representing the evolution of the main model's parameters. The Orange line represents the FE simulation results while the blue one represents the analytical solution.

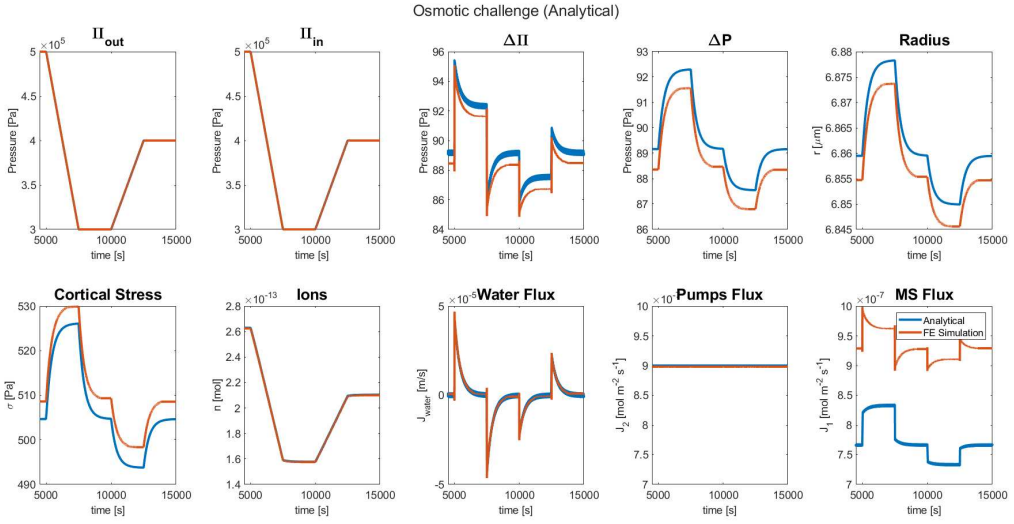

Figure 8.7: Curves representing the evolution of the main model's parameters. The Orange line represents the FE simulation results while the blue one represents the analytical solution.

8.3 Biomass synthesis simulations

Using the approach described in the previous chapter, it was decided to simulate the growth of the model due to the presence of an impermeable biomass n_{imp}.

The analysis includes an initial transient phase to reach the steady state after which the impermeable biomass begins to grow until the target limit $3.77 \cdot 10^{-16}$. This value was

found empirically by testing the model with different values of biomass target in order to reach a volume 2.36 times greater than the initial volume using the insights from the previous chapter.

The results of this analysis are presented in figure 8.8.

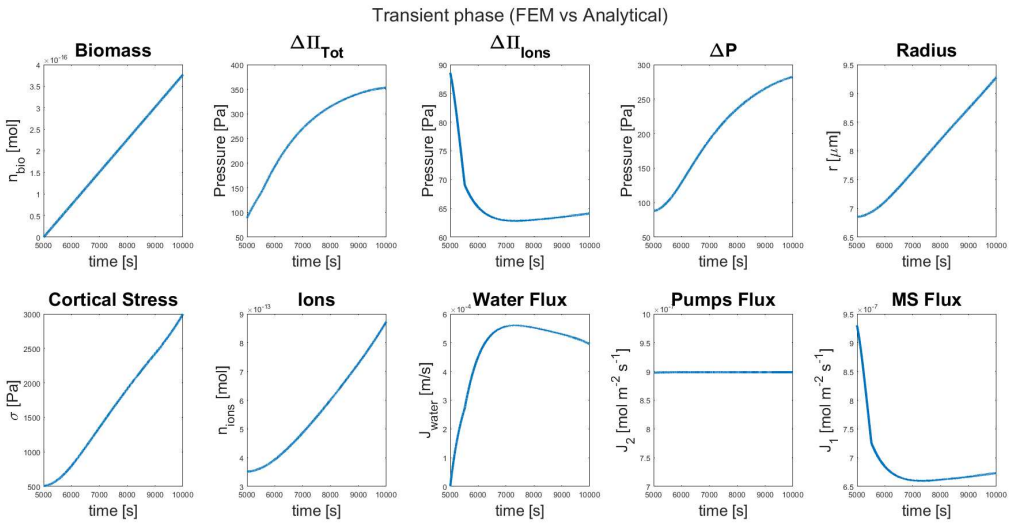

Figure 8.8: Curves representing the evolution of the main model's parameters.

Some peculiar behaviour can be seen in the model. Although the number of ions decreases due to an increase in the cell volume, the rate at which ions enter the cell is not enough to keep the osmotic pressure due to ions up. On the other hand, the osmotic pressure difference due to the total mass (biomass and ions) inside the cell increases sharply.

Of course, this simulation aims only at showing the ability of the model to grow and respond to the presence of biomass production but the value of impermeable biomass itself it is not representative of the real mass since the material composing the cell cannot be significantly less than the amount of ions currently inside the cell.

Further studies could help create a model able to represent the real evolution of the cell's mass throughout the cell cycle as well as to show the behaviour of the cell in response to a non-linear production of biomass.

9 Conclusions

The models presented in this work have proven to be reliable in addressing both the mechanical and the biological response of the cell in the scenarios of interest. The continuous, continuous-tensegrity and bendo-tensegrity models offer different levels of complexity and fidelity to the mechanical aspects pertaining to the cellular response to mechanical stimuli. These models have been proven to be effective in representing the mechanical response during atomic force microscopy indentation tests and, to some degree, to the response during micropipette aspiration tests. Although the continuous model has been once again proven to be able to faithfully represent the global response of the cell while remaining computationally light, the more complex tensegrity models can offer insights into the mechanical response of singular cell subcomponents and their role in the overall response. Since the cell is able to react to mechanical stimuli by processes like mechanotransduction, it is paramount to develop a thorough understanding of the role of these subcomponents in the overall response. This can only be achieved by employing models that take into consideration the real morphology and mechanics of the cell such as has been done with the models here presented. These models could be further improved by the introduction of phenomenons such as the microtubule catastrophe thus providing even more reliable results and expanding their usability. Since cells are not passive materials but rather active organisms able to remodel and modulate their mechanical response in accordance to external signal it is similarly important to delve into the biological aspects as it has been done with McEvoy's biomechanical model hereby presented. The introduction of the cellular response to changes in osmotic pressure and cell impermeable biomass can greatly improve the simplistic passive models allowing them to make further steps into a comprehensive model of cell physiology. The ability of these models to predict the response of the cell to chemical stressors such as this in silico can improve the arsenal of doctors and biologists in their search for cures for many pathologies which could otherwise be only studied in vitro or in suboptimal conditions in vivo. As mentioned in the previous chapters, this model still includes simplifications such as the use of only one species of ion and the disregard for electroneutrality. It is clear that this model could greatly benefit from further development in these parts to be able to completely describe the cell response to changes in the environmental osmotic pressure. Both the mechanical and the biomechanical models presented in this work can predict the behaviour of an average cell whether healthy or in a pathological state. The medical world, on the other hand, is providing more and more proof of the need to create patient-specific solutions. While models representing the average behaviour of a cell can be valuable and informative, real cells can display significant variability in their mechanical response and this is especially true for tumour cells. For this reason, the paucity of data in the literature and the lack (to the author's knowledge) of widespread and comprehensive databases of cell behaviours is a hurdle that needs to be addressed. Computational models and numerical models

can be easily adapted to simulate a widespread range of real scenarios and thus they can provide a useful, cheap and reproducible framework for studying cell behaviour.

The models presented in this work can help us improve our understanding of cell behaviour both in pathological and physiological conditions and will be a valuable tool for researchers aiming at a complete understanding of the smallest living components of the human body.

Appendices

The following code is a Matlab code able to produce the analytical solution to the biomechanical model by McEvoy et Al.

The specific model refers to a transient phase to reach the steady state (5000 seconds) followed by the biomass synthesis simulation that occurs during 5000 seconds.

A Matlab implementation of McEvoy's model

```
%% Parameters and constants
% UNITS
%
% Mass            Tonne
% Pressure        MPa
% Length          mm
% Temp            K
% Force           N
% Time            s

global r0 K sigmaa sigmac sigmas th beta R Tk P0crit Wl Wa TotT BioTarg
    StartT Ttarg
syms Bio(t) Ions(t) Vol(t)

%% Model parameters

Wl = 1.5e-9;              % leakage channels permeability (mol mm^-2 s^-1
    MPa^-1)
Wa = 2.25e-17;          % active pumps permeability (mol mm^-2 s^-1 MPa^-1)
R = 8314.46;          % gas constant (mJ mol^-1 K^-1)
Tk = 309.15;          % absolute temperature (K)
beta = 2e-5;          % MS channels permeability (mol mm^-2 s^-1 MPa^-2)
P0crit = 40000;       % critical osmotic pressure (MPa)
BioTarg = 3.44e-17;         % target biomass to be produced (mol)
r0 = rad(1.147250700000001e-06);          % reference volume of the cell (
    mm)
Lpm = 0.007;              % rate of water transport (mm s^-1 MPa^-1)
K = 0.006;            % membrane elastic modulus (MPa)
th = 5e-4;            % membrane thickness (mm)
sigmaa = -1e-4;       % active cortical stress (MPa)
sigmac = 7.5e-5;        % threshold stress for MS channels (MPa)
sigmas = 6e-4;        % saturating stress for MS channels (MPa)

%% Time options
```

```
StartT = 5000;
Ttarg = 5000;
TotT = StartT + Ttarg;

%% Set ODES
y0 = [0, Pout(0)*Volume(r0)/(R*Tk), Volume(r0)];
tSpan = [0, TotT];

options = odeset('RelTol',5e-14,'AbsTol',5e-14);
[T, Y] = ode45(@(t,y) fcn(t, y, Wl, Wa, P0crit, Lpm), tSpan, y0, options);

OsmP = zeros(length(T),1);
Press = zeros(length(T),1);
ExtOP = zeros(length(T),1);
PinV = zeros(length(T),1);
sig = zeros(length(T),1);
Flux3 = zeros(length(T),1);
Biom = zeros(length(T),1);
for i = 1:length(T)
    t = T(i);
    if (i == 1)
        v = y0(3);
        ion = y0(2);
    else
        v = Y(i,3);
        ion = Y(i,2);
    end
    Press(i) = Phin(v);
    ExtOP(i) = Pout(t);
    PinV(i) = Pin(v,ion);
    OsmP(i) = PinV(i)-ExtOP(i);
    p = OsmP(i);
    sig(i) = cortStress(v);
    Flux3(i) = j3(v,p);
    Biom(i) = Biomass(t);
end

NetF = Flux1 + Flux2 + Flux3;



function dy = fcn(t, y, Wl, Wa, P0crit, Lpm)
dy = [-A(y(3))*((Wl+Wa+Wms(y(3)))*(Pin(y(3),y(2))-Pout(t)) - Wa*P0crit);
      -A(y(3))*Lpm*(Phin(y(3)) - (Pin(y(3),y(2)+Biomass(t))-Pout(t)))];
end

function Area = A(Vol)
    radius = rad(Vol);
    Area = 4*pi*radius^2;
end

```

```
function r = rad(Vol)
    r = ((3.*Vol)./(4*pi)).^(1/3);
end

function press = Pout(t)
    press = 0.67;
end

function sig = cortStress(Vol)
    global r0 K sigmaa
    r = rad(Vol);
    rr = (r.^2)./(r0^2);
    sig = (K/2).*(rr-1) - sigmaa;
end

function w = Wms(Vol)
    global sigmac sigmas beta
    sig = cortStress(Vol);
    if sig < sigmac
        w = 0;
    elseif (sig >= sigmac && sig <= sigmas)
        w = beta*(sig-sigmac);
    elseif sig > sigmas
        w = beta*(sigmas-sigmac);
    end
end

function press = Phin(Vol)
    global th
    r = rad(Vol);
    sig = cortStress(Vol);
    press = sig*th*2/r;
end

function press = Pin(Vol, Solute)
    global R Tk
    press = (Solute.*R.*Tk)./Vol;
end

function v = Volume(radius)
    v = ((4*pi).*(radius.^3))./3;
end

function f1 = j1(OsmP)
    global Wl
    f1 = Wl.*OsmP;
end

function f2 = j2(OsmP)
    global P0crit Wa
    f2 = Wa.*(P0crit - OsmP);
```

```
134 end

136 function f3 = j3(Vol, OsmP)

138     WmsV = zeros(length(Vol),1);
        for i = 1:length(Vol)
140         WmsV(i) = Wms(Vol(i));
        end
142     f3 = -WmsV.*OsmP;
end
144
function nimp = Biomass(t)
146     global BioTarg StartT Ttarg
        if (t< StartT)
148         nimp = 0;
        elseif (t>=StartT)
150         k = (BioTarg/Ttarg);
            t = t - StartT;
152         nimp = k*t;
        end
154 end
```

In order to simulate an osmotic challenge one would just need to set the BioTarg variable to 0 and change the Pout(t) function as follows.

f

```
global StartT ChallT
2     L = 0.3;
      H = 0.5;
4     M = 0.4;
      if (t<=StartT)
6         press = H;
      elseif ((StartT<t)&(t<StartT+ChallT/2))
8         t = t - StartT;
          s = (L-H)*2/ChallT;
10        q = H;
          press = s*t + q;
12    elseif ((t>=StartT+ChallT/2)&(t<StartT+ChallT))
          press = L;
14    elseif ((StartT+ChallT<=t)&(t<StartT+ChallT+ChallT/2))
          t = t - StartT - ChallT;
16        s = (M-L)*2/ChallT;
          q = L;
18        press = s*t + q;
      elseif ((t>=StartT+ChallT+ChallT/2))
20        press = M;
      end
22 end
```

B Fortan Subroutines

B.1 UMAT

The following UMAT subroutine has been developed to describe two materials present in the model (Cytoplasm and Membrane).

In the following, the code has been subdivided into relevant portions to aid the description of each part.

```
      SUBROUTINE UMAT(STRESS,STATEV,DDSDDE,SSE,SPD,SCD,
     1 RPL,DDSDDT,DRPLDE,DRPLDT,
     2 STRAN,DSTRAN,TIME,DTIME,TEMP,DTEMP,PREDEF,DPRED,CMNAME,
     3 NDI,NSHR,NTENS,NSTATV,PROPS,NPROPS,COORDS,DROT,PNEWDT,
     4 CELENT,DFGRD0,DFGRD1,NOEL,NPT,LAYER,KSPT,KSTEP,KINC)

      INCLUDE 'ABA_PARAM.INC'

      CHARACTER*80 CMNAME
      DIMENSION STRESS(NTENS),STATEV(NSTATV),
     1 DDSDDE(NTENS,NTENS),DDSDDT(NTENS),DRPLDE(NTENS),
     2 STRAN(NTENS),DSTRAN(NTENS),TIME(2),PREDEF(1),DPRED(1),
     3 PROPS(NPROPS),COORDS(3),DROT(3,3),DFGRD0(3,3),DFGRD1(3,3)

      DIMENSION EELAS(6), EELASP(3), BMAT(6), BBARP(3), BBARN(3, 3),
     1          DISTGR(3,3), DFGRD1e(3,3)

      PARAMETER(ZERO=0.D0, ONE=1.D0, TWO=2.D0, THREE=3.D0, FOUR=4.D0,
     1 SIX=6.D0)

      PARAMETER(ELEMSIZE=99000, INTEGPTS=8)
      REAL   REF_VOL, CURR_VOL, xg, xlamg, FINALVOL, TEMP,
     1       PRESSURES(ELEMSIZE,INTEGPTS), INCARRAY(999000, 5),
     2       E, nu, lambda, mu, CORTSIGMA(ELEMSIZE,INTEGPTS),
     3       AStress
      INTEGER INCLINE
      LOGICAL TEST
      COMMON/PRESSURE/ PRESSURES, CORTSIGMA
      COMMON/INCREMENT/ FINALVOL, INCARRAY, INCLINE
      COMMON/VOLUMES/REF_VOL, CURR_VOL
```

The UMAT subroutine employs the use of three common blocks to share data with the other subroutines.

The PRESSURE common block holds the matrix PRESSURES and CORTSIGMA which are responsible for holding the values of hydrostatic pressure of the cytoplasm elements and the cortical stress values for the elements representing the cortical membrane.

The INCREMENT common block holds important information relative to the current and previous increments. The variable FINALVOL holds the last computed final volume (or target volume), the matrix INCARRAY holds the most relevant data points of the simulation and is used to access values at previous increments in case of failure to converge and finally, INCLINE is a counter pointing at the last line of INCARRAY.

The VOLUMES common block holds the values for the reference volume REF_VOL (the volume at the beginning of the simulation in a stress-free condition) and the current volume CURR_VOL of the cytoplasm.

```
      IF (CMNAME.EQ.'CYTOPLASM') THEN
2
        C10 = PROPS(1)
4       D1 = PROPS(2)
        iswitch=int(PROPS(3))
6
        XPI = 3.14159265359
8
      if (KINC.LT.TWO.AND.KSTEP.LT.TWO) then
10        xlamg = 1.0
          xg = 0.
12        STATEV(5) = xg
      else
14        xg = (FINALVOL/REF_VOL)**(1.0/3.0) - 1.0
          STATEV(5) = xg
16        xlamg = 1.0 + xg
      end if
18
      IF (NOEL.EQ.ONE.AND.NPT.EQ.ONE) THEN
20        open(110,file='/MyFolder/Data5.dat',status='old', access='append
    ')
          write(110,*) xg
22        close(110)
      ENDIF
24    dfgrd1e = (1/xlamg)*dfgrd1
```

In the first part of the code, the values for the Neo-Hookean model are stored in the C10 and D1 variables which will be used in the remaining part of the code to compute the cytoplasm response. The most interesting part, on the other hand, is the scaling of the deformation gradient to achieve the final volume of the cell. During the first increment, the growth is set to zero in order to allow the code to set the initial values needed to solve the ODEs. Finally, the scaling value xg is stored in a data file to be later used to analyze the model's behaviour.

```
2     DET=dfgrd1e(1, 1)*dfgrd1e(2, 2)*dfgrd1e(3, 3)
```

```
     1    -dfgrd1e(1, 2)*dfgrd1e(2, 1)*dfgrd1e(3, 3)
      IF(NSHR.EQ.3) THEN
        DET=DET+dfgrd1e(1, 2)*dfgrd1e(2, 3)*dfgrd1e(3, 1)
     1           +DFGRD1e(1, 3)*dfgrd1e(3, 2)*dfgrd1e(2, 1)
     2           -dfgrd1e(1, 3)*dfgrd1e(3, 1)*dfgrd1e(2, 2)
     3           -dfgrd1e(2, 3)*dfgrd1e(3, 2)*dfgrd1e(1, 1)
      END IF
      SCALE=DET**(-ONE/THREE)
      DO K1=1, 3
        DO K2=1, 3
          DISTGR(K2, K1)=SCALE*dfgrd1e(K2, K1)
        END DO
      END DO
C     CALCULATE DEVIATORIC LEFT CAUCHY-GREEN DEFORMATION TENSOR
C
      BMAT(1)=DISTGR(1, 1)**2+DISTGR(1, 2)**2+DISTGR(1, 3)**2
      BMAT(2)=DISTGR(2, 1)**2+DISTGR(2, 2)**2+DISTGR(2, 3)**2
      BMAT(3)=DISTGR(3, 3)**2+DISTGR(3, 1)**2+DISTGR(3, 2)**2
      BMAT(4)=DISTGR(1, 1)*DISTGR(2, 1)+DISTGR(1, 2)*DISTGR(2, 2)
     1        +DISTGR(1, 3)*DISTGR(2, 3)
      IF(NSHR.EQ.3) THEN
        BMAT(5)=DISTGR(1, 1)*DISTGR(3, 1)+DISTGR(1, 2)*DISTGR(3, 2)
     1          +DISTGR(1, 3)*DISTGR(3, 3)
        BMAT(6)=DISTGR(2, 1)*DISTGR(3, 1)+DISTGR(2, 2)*DISTGR(3, 2)
     1          +DISTGR(2, 3)*DISTGR(3, 3)
      END IF
C
C     CALCULATE THE STRESS
C
      TRB=(BMAT(1)+BMAT(2)+BMAT(3))/THREE
      EG=TWO*C10/DET
      EK=TWO/D1*(TWO*DET-ONE)
      PR=TWO/D1*(DET-ONE)
      DO K1=1,NDI
        STRESS(K1)=EG*(BMAT(K1)-TRB)+PR
      END DO
      DO K1=NDI+1,NDI+NSHR
        STRESS(K1)=EG*BMAT(K1)
      END DO
C     CALCULATE THE STIFFNESS
C
      EG23=EG*TWO/THREE
      DDSDDE(1, 1)= EG23*(BMAT(1)+TRB)+EK
      DDSDDE(2, 2)= EG23*(BMAT(2)+TRB)+EK
      DDSDDE(3, 3)= EG23*(BMAT(3)+TRB)+EK
      DDSDDE(1, 2)=-EG23*(BMAT(1)+BMAT(2)-TRB)+EK
      DDSDDE(1, 3)=-EG23*(BMAT(1)+BMAT(3)-TRB)+EK
      DDSDDE(2, 3)=-EG23*(BMAT(2)+BMAT(3)-TRB)+EK
      DDSDDE(1, 4)= EG23*BMAT(4)/TWO
      DDSDDE(2, 4)= EG23*BMAT(4)/TWO
      DDSDDE(3, 4)=-EG23*BMAT(4)
```

```
54          DDSDDE(4, 4)= EG*(BMAT(1)+BMAT(2))/TWO
            IF(NSHR.EQ.3) THEN
56            DDSDDE(1, 5)= EG23*BMAT(5)/TWO
              DDSDDE(2, 5)=-EG23*BMAT(5)
58            DDSDDE(3, 5)= EG23*BMAT(5)/TWO
              DDSDDE(1, 6)=-EG23*BMAT(6)
60            DDSDDE(2, 6)= EG23*BMAT(6)/TWO
              DDSDDE(3, 6)= EG23*BMAT(6)/TWO
62            DDSDDE(5, 5)= EG*(BMAT(1)+BMAT(3))/TWO
              DDSDDE(6, 6)= EG*(BMAT(2)+BMAT(3))/TWO
64            DDSDDE(4,5)= EG*BMAT(6)/TWO
              DDSDDE(4,6)= EG*BMAT(5)/TWO
66            DDSDDE(5,6)= EG*BMAT(4)/TWO
            END IF
68          DO K1=1, NTENS
              DO K2=1, K1-1
70              DDSDDE(K1, K2)=DDSDDE(K2, K1)
              END DO
72          END DO

74          TEMP = 0
            DO I=1,3
76              TEMP = TEMP + STRESS(I)
            ENDDO
78          PRESSURES(NOEL,NPT) = -(1.D0/3.D0)*TEMP
```

At this point, the hydrostatic pressure at the current integration point of the current element is calculated as the $p = -\frac{I_3}{3}$ where I_3 is the first stress invariant calculated using the Cauchy stress tensor.

This point concludes the calculations made for the elements representing the cytoplasm.

```
2           ELSEIF (CMNAME.EQ.'MEMBRANE') THEN

4           E = props(1)
            nu = props(2)
6           AStress = 1e-4
```

This portion of the code is used to calculate the cortical stress of the cell as the response of the elements representing the cellular membrane. As explained in chapter 7, the membrane is described as a simple linear elastic body with the addition of an active component represented in this code by AStress.

```
            lambda = E*nu/((1.0d0+nu)*(1.0d0-2.0d0*nu))
2           mu = E/(2.0d0*(1.0d0+nu))
```

```
4       DO I = 1, NTENS
          DO j = 1, NTENS
6           DDSDDE(I,J) = 0.0d0
          END DO
8       END DO

10      DO I = 1, NDI
          DO J = 1, NDI
12          DDSDDE(I, J) = lambda
          END DO
14        DDSDDE(I,I) = lambda + 2.0d0*mu
        END DO
16
        DO I = NDI+1, NTENS
18        DDSDDE(I,I) = mu
        END DO
20
        DO I = 1, NTENS
22        DO J = 1, NTENS
            STRESS(I) = STRESS(I) + DDSDDE(I,J) * DSTRAN(J)
24        END DO
        END DO
26      TEMP = 0

28      IF (KINC.EQ.ONE.AND.KSTEP.EQ.ONE) THEN
DO I = 2, 3
30  STRESS(I) = STRESS(I) + AStress
END DO
32      ENDIF

34      DO I = 2, 3
            TEMP = TEMP + STRESS(I)
36      END DO

38      CORTSIGMA(NOEL,NPT) = TEMP/2.0

40      ENDIF
        RETURN
```

At this point, the average cortical stress at the current integration point of the current element is computed as the average stress along directions 2 and 3. The model uses a custom orientation for the membrane elements so that these two directions are always correctly aligned. Similarly to what has been done for the pressure values, the cortical stress values are stored in the CORTSIGMA array to be later used by other subroutines. Notice that the value of AStress is added to the stress vector only during the first increment of the first step.

B.2 UVARM

The UVARM subroutine is a simple subroutine used to access the volume of each integration point of each element in order to calculate the reference volume REF_VOL (during the first increment of the first step) and to obtain the updated current volume saved in the IVOL matrix. The subroutine is automatically called only for the integration points of elements for which the material definition includes the specification of user-defined output variables. In this model, only the cytoplasm has user-defined output variables defined.

```
      SUBROUTINE UVARM(UVAR,DIRECT,T,TIME,DTIME,CMNAME,ORNAME,
     1 NUVARM,NOEL,NPT,LAYER,KSPT,KSTEP,KINC,NDI,NSHR,COORD,
     2 JMAC,JMATYP,MATLAYO,LACCFLA)

      INCLUDE 'ABA_PARAM.INC'

      CHARACTER*80 CMNAME,ORNAME
      CHARACTER*3 FLGRAY(15)
      DIMENSION UVAR(NUVARM),DIRECT(3,3),T(3,3),TIME(2)
      DIMENSION ARRAY(15),JARRAY(15),JMAC(*),JMATYP(*),COORD(*)

      PARAMETER(ELEMSIZE=99000, INTEGPTS=8)
      REAL IVOL(ELEMSIZE,INTEGPTS), CURR_VOL, REF_VOL, Wms
      INTEGER ZERO, ONE

      COMMON/IVOL_GLOBAL/IVOL
      COMMON/VOLUMES/REF_VOL, CURR_VOL

      ZERO = 0
      ONE = 1

      IF (KINC.EQ.ZERO.AND.KSTEP.EQ.ONE) THEN

         CALL GETVRM('IVOL',ARRAY,JARRAY,FLGRAY,JRCD,JMAC,JMATYP,
     1    MATLAYO,LACCFLA)
         IVOL(NOEL,NPT) = ARRAY(1)

         REF_VOL = SUM(IVOL, MASK = IVOL .GT. 0.0)
         CURR_VOL = REF_VOL
         UVAR(1) = CURR_VOL
         UVAR(2) = REF_VOL
      ELSE
         CALL GETVRM('IVOL',ARRAY,JARRAY,FLGRAY,JRCD,JMAC,JMATYP,
     1    MATLAYO,LACCFLA)
         IVOL(NOEL,NPT) = ARRAY(1)
      ENDIF

      RETURN
      END
```

B.3 UEXTERNALDB

The UEXTERNALDB is a subroutine usually employed to communicate with external databases during the execution of the analysis. In this case the subroutine is used to collect the local variables and calculate the solution of the ODEs governing the growth of the cell and ion flux. This subroutine uses a variable called LOP to identify at which portion of the code it is called. When LOP=0 it means that the subroutine is called at the beginning of the simulation while if LOP=1 the subroutine is called at the beginning of an increment.

```
      SUBROUTINE UEXTERNALDB(LOP,LRESTART,TIME,DTIME,KSTEP,KINC)
2
      INCLUDE 'ABA_PARAM.INC'
4
      PARAMETER(ELEMSIZE=99000, INTEGPTS=8)
6     REAL  REF_VOL, CURR_VOL, VOLPAR, TOTSIGMA, FWms(1)
      REAL YSTART(2), X1, X2, dYdX(2), FINALVOL, Bio(1),
8    1      TOTPRESS, PRESSURES(ELEMSIZE,INTEGPTS), R(1), T(1),
     2      IONS, INCARRAY(999000, 5), CORTSIGMA(ELEMSIZE,INTEGPTS),
10   3      OPext(1), Tc(1), JWat, J2, J3, Wa, P0crit, Lpm(1), TT,
     4      IVOL(ELEMSIZE,INTEGPTS), RealVol, H1, HMIN, TOL
12    DIMENSION TIME(2), VOLPAR(7)
      COMMON/IVOL_GLOBAL/IVOL
14    COMMON/VOLUMES/REF_VOL, CURR_VOL
      COMMON/INCREMENT/ FINALVOL, INCARRAY, INCLINE, TOTLINE
16    COMMON/PRESSURE/ PRESSURES, CORTSIGMA
      COMMON/BIOMASS/ IONS
18    INTEGER TWO, ONE, INCLINE, TOTLINE, THREE
```

All the previous common blocks are called during this subroutine as well as a common block called BIOMASS which stores the amount of ions currently inside the cell so that the value is not reset at each increment.

```
      TWO = 2
2     ONE = 1
      ZERO = 0
4     THREE = 3

6     X1 = TIME(2)
      X2 = X1 + DTIME
8     TOL = 1e-3
      H1 = DTIME/10
10    HMIN = 0.0
```

Two strategies have been used in order to solve the system of ODEs governing the model. One is a fifth-order Runge-Kutta solver and the other one is a simpler method based on

the Monte-Carlo approach. If the Runge-Kutta solver is used then the variables listed represent the following:

- X1 is the initial time at which the calculations occur;
- X2 is the final time for the current increment;
- TOL is the tolerance for the output of the Runge-Kutta method;
- H1 represents the length of each step that the Runge-Kutta method uses for solving the ODEs;
- HMIN represents the minimum step allowed for solving the ODEs.

If the Monte-Carlo approach is used then only the X1 and X2 variables are need to solve the ODEs.

```
Wa = 2.25e-17
P0crit = 40000
Lpm(1) = 0.007
R(1) = 8314.46
T(1) = 309.15
```

This other set of variables are part of the model described in chapter 7.

```
TT = TIME(1)

IF (LOP.EQ.ZERO) THEN
    DO I = 1,ELEMSIZE
        DO J = 1,INTEGPTS
            PRESSURES(I,J)=0
            CORTSIGMA(I,J)=0
        ENDDO
    ENDDO
ENDIF
```

If the code is called at the beginning of the simulation, then the values of pressure and stress in the PRESSURES and CORTSIGMA subroutines are initialized to 0.

```
IF (LOP.EQ.ONE .AND. CURR_VOL.GT.ZERO) THEN

    TOTSIGMA = SUM(CORTSIGMA)/1088.0
    TOTPRESS = SUM(PRESSURES)/1896.0
    IF (INCLINE.LT.ONE) THEN

        INCLINE = 1
        TOTLINE = 0
```

```
            REF_VOL = 36.0*REF_VOL
            CURR_VOL = 36.0*CURR_VOL
            IONS = 0.5*REF_VOL/(R(1)*T(1))

            INCARRAY(INCLINE,1) = KINC
            INCARRAY(INCLINE,2) = IONS
            INCARRAY(INCLINE,3) = CURR_VOL
            INCARRAY(INCLINE,4) = TOTPRESS
            INCARRAY(INCLINE,5) = TOTSIGMA
        ENDIF
```

If the subroutine is called at the beginning of a step after having initialized the reference volume (and the current volume since it is equal to the reference volume at the beginning of the simulation) then the code proceeds to calculate the following global variables:

- TOTSIGMA average stress of the cortical membrane;
- TOTPRESS the average pressure inside the elements composing the cytoplasm;
- CURR_VOL is the current volume of the cell. Since the model uses a radial symmetry constraint to simulate only 10 degrees of a sphere, this value has to be multiplied by 36 to obtain the total volume;
- REF_VOL is the initial volume of the cell. Similarly to the CURR_VOL it is scaled to represent the spherical cell;
- IONS are initialized to a value that sets $\Delta\Pi = 0$.

Notice that the scaling of the reference volume, current volume and initialization of the number of ions happens only the first time this portion of code is called thanks to the INCLINE variable.

```
        IF (INCLINE.GT.ONE .AND. KINC.EQ.INCARRAY(INCLINE,1)) THEN

            IONS = INCARRAY(INCLINE_ONE,2)
            CURR_VOL = INCARRAY(INCLINE_ONE,3)
            TOTPRESS = INCARRAY(INCLINE_ONE,4)
            TOTSIGMA = INCARRAY(INCLINE_ONE,5)

            CALL LineDelete(TOTLINE)
            TOTLINE = TOTLINE - 1
        ENDIF
```

This portion of the code is used to check if the current increment is been called for a second time due to failing to converge in the previous attempt. If that's the case then the system variables are loaded back to their previous value in order to not propagate errors.

```
2           IF (KINC.GT.ONE .OR. KSTEP.GT.case then the variaONE) THEN

4           Tc = 5000
            CALL MecanoSensing(FWms, TOTSIGMA)
6           CALL OsmPressWave(OPext,KSTEP,Tc, TT)
            CALL Biosinth(TT,Tc,Bio)
8           Wms = FWms(1)

10          YSTART(1) = IONS
            YSTART(2) = CURR_VOL
12
            VOLPAR(1) = TOTPRESS
14          VOLPAR(2) = CURR_VOL
            VOLPAR(3) = IONS
16          VOLPAR(4) = Wms
            VOLPAR(5) = OPext(1)
18          VOLPAR(6) = Bio(1)
            VOLPAR(7) = KINC
20
            call odeint(ystart,2,X1,X2,TOL,H1,HMIN,nok,nbad,VOLPAR)
22
            FINALVOL = YSTART(2)
24          IONS = YSTART(1)
            CURR_VOL = YSTART(2)
```

At this point, the subroutine proceeds to calculate the current value of ω_{ms}, Π_{ext} and n_{imp} and calls the subroutine ODEINT to solve the ODEs. The output values (target volume FINALVOL and number of ions IONS) are saved for the next increment. Notice that the current volume is now updated to be automatically equal to the target volume. This has been done by observing how accurately the UMAT forces the cell to grow to the target volume but can be changed if necessary.

```
2           OSMPRESS = R(1)*(IONS)*T(1)/CURR_VOL - VOLPAR(5)
            ELSE
4               OPext(1) = 0.5
                CURR_VOL = REF_VOL
6               OSMPRESS = R(1)*(IONS)*T(1)/CURR_VOL - OPext(1)
            ENDIF
8
            JWat = Lpm(1)*(OSMPRESS-TOTPRESS)
10          J2 = Wa*(P0crit-OSMPRESS)
            J3 = Wms*OSMPRESS
12
C           Writing increment results to file
14          IF (KINC.EQ.ZERO.OR.MOD(KINC,10).EQ.5.0) THEN
            open(106,file='/Myfolder/AxOsm7/Data1.dat',status='old', access=
    'append')
```

```
16          open(107,file='/Myfolder/AxOsm7/Data2.dat',status='old', access=
    'append')
            open(108,file='/Myfolder/Data3.dat',status='old', access='append
    ')
18          write(106,*) TIME(2)+DTIME, IONS, CURR_VOL, TOTPRESS
            write(107,*) OSMPRESS, KINC, TOTSIGMA, Wms
20          write(108,*) OPext(1), JWat, J2, J3
            close(106)
22          close(107)
            close(108)
24          TOTLINE = TOTLINE + 1
            ENDIF
26
      IF (INCLINE.EQ.ONE .OR. KINC.NE.INCARRAY(INCLINE,1)) THEN
28
            INCLINE = INCLINE + ONE
30
                INCARRAY(INCLINE,1) = KINC
32              INCARRAY(INCLINE,2) = IONS
                INCARRAY(INCLINE,3) = CURR_VOL
34              INCARRAY(INCLINE,4) = TOTPRESS
                INCARRAY(INCLINE,5) = TOTSIGMA
36    ENDIF
      ENDIF
38
      RETURN
40
      END
42
```

At the end of the subroutine, some variables of interest are printed to the output files and the INCARRAY array is updated to store the new values and the pointer to the last line is updated to reflect that.

B.4 Subroutines for solving ODEs

As explained earlier, two different approaches have been used to solve the ODEs. While the Runge-Kutta solver is generally better suited for this problem, the Monte-Carlo approach gives intuitive solutions that are good enough for reaching the steady state and understanding the model's behaviour.

In the following, both codes are presented but not thoroughly described since their code is intuitive and generally well-known in the literature.

B.4.1 DERIVS subroutine

The DERIVS subroutine simply holds the ODEs governing the model and calculates their value at the given time. It is used for both solvers.

```
      SUBROUTINE derivs(x, y, dydx, Xparams)

      INCLUDE 'ABA_PARAM.INC'

      intent(in) x, y, XPARAMS
      intent(out) dydx
      REAL x, y, dydx(2), XPARAMS(6), Pc(1), Vc(1), Nc(1), Rc(1), Ac(1),
     1    Wl(1), Wa(1), P0ions(1), P0crit(1), Nt(1), Lpm(1), P0out(1),
     2    P0intot(1), R(1), T(1), Pi(1), beta(1), TotN(1), Wms(1), Bio(1)

      Pc(1) = XPARAMS(1)
      Vc(1) = XPARAMS(2)
      Nc(1) = XPARAMS(3)
      Wms(1) = XPARAMS(4)
      P0out = XPARAMS(5)
      Bio(1) = XPARAMS(6)
      KINC = XPARAMS(7)
      Pi(1)=3.14159265359
      Rc(1) = ( (3*Vc(1))/(4*Pi(1)) )**(1.D0/3.D0)
      Ac(1) = 4*Pi(1)*(Rc(1)**2)
      Wl(1) = 1.5e-9
      Wa(1) = 2.25e-17
      R(1) = 8314.46
      T(1) = 309.15
      TotN(1) = Nc(1)
      P0ions(1) = Nc(1)*R(1)*T(1)/Vc(1)
      P0intot(1) = TotN(1)*R(1)*T(1)/Vc(1)
      beta(1) = 1e14
      P0crit(1) = 40000

      Lpm(1) = 0.007

      dydx(1) = -Ac(1)*( (Wl(1)+Wa(1)+Wms(1))*(P0ions(1)-P0out(1))
     1 - Wa(1)*P0crit(1))
      dydx(2) = -Ac(1)*Lpm(1)*(Pc(1)-(P0intot(1)-P0out(1)))

      END SUBROUTINE derivs
```

B.4.2 Runge Kutta solver

The Runge-Kutta solver is divided into two subroutines: the first one is the solver driver and the second part handles the calculations.

```
      SUBROUTINE odeint(ystart,nvar,x1,x2,eps,h1,hmin,nok,nbad
     1  ,Xparams)
```

```
4
      INTEGER nbad,nok,nvar,KMAXX,MAXSTP,NMAX
6     REAL eps,h1,hmin,x1,x2,ystart(nvar),TINY
      DIMENSION Xparams(10)
8
      Parameter (MAXSTP=10000,NMAX=50,KMAXX=200,TINY=1.e-30)
10
      INTEGER i,kmax,kount,nstp
12    REAL dxsav,h,hdid,hnext,x,xsav,dydx(NMAX),xp(KMAXX),y(NMAX),
     1 yp(NMAX,KMAXX),yscal(NMAX)
14

16    x=x1
      h=sign(h1,x2-x1)
18    nok=0
      nbad=0
20    kount=0

22    DO i=1,nvar
        y(i)=ystart(i)
24    ENDDO

26    IF (kmax.gt.0) xsav=x-2.*dxsav

28    DO nstp=1,MAXSTP
        CALL derivs(x,y,dydx,Xparams)
30
        DO i=1,nvar
32        yscal(i)=abs(y(i))+abs(h*dydx(i))+TINY
        ENDDO
34
        IF(kmax.gt.0)then
36        IF(abs(x-xsav).gt.abs(dxsav)) then
            IF(kount.lt.kmax-1)then
38            kount=kount+1
              xp(kount)=x
40
              DO i=1,nvar
42              yp(i,kount)=y(i)
              ENDDO
44
              xsav=x
46          ENDIF
          ENDIF
48      ENDIF

50      IF((x+h-x2)*(x+h-x1).gt.0.) h=x2-x

52      CALL rkqs(y,dydx,nvar,x,h,eps,yscal,hdid,hnext,Xparams)

54      IF(hdid.eq.h)then
```

```
            nok=nok+1
56          ELSE
            nbad=nbad+1
58          ENDIF

60          IF((x-x2)*(x2-x1).ge.0.)then      !

62            DO i=1,nvar
                ystart(i)=y(i)
64            ENDDO

66            IF(kmax.ne.0)then
                kount=kount+1
68              xp(kount)=x

70              DO i=1,nvar
                  yp(i,kount)=y(i)
72              ENDDO

74            ENDIF
              RETURN
76          ENDIF

78          IF(abs(hnext).lt.hmin) then
            pause 'stepsize smaller than min odeint'
80          CALL EXIT(1)
          ENDIF
82          h=hnext

84        ENDDO

86        pause 'too many steps in odeint'
        CALL EXIT(1)
88
          RETURN
90        END SUBROUTINE odeint

92  c
```

The rkqs subroutine is responsible for calculating the step evaluation of the ODEs solutions.

```
2         SUBROUTINE rkqs(y,dydx,n,x,htry,eps,yscal,hdid,hnext,Xparams)
          INTEGER n,NMAX
4         REAL eps,hdid,hnext,htry,x,dydx(n),y(n),yscal(n)
          REAL yout(n)
6         DIMENSION Xparams(10)
          Parameter (NMAX=50)
8
```

```
      INTEGER i
      REAL errmax,h,htemp,xnew,yerr(n),ytemp(n),SAFETY,PGROW,
     1 PSHRNK,ERRCON
      REAL ak2(n),ak3(n),ak4(n),ak5(n),ak6(n),
     1 A2,A3,A4,A5,A6,B21,B31,B32,B41,B42,B43,B51,
     1 B52,B53,B54,B61,B62,B63,B64,B65,C1,C3,C4,C6,DC1,DC3,
     1 DC4,DC5,DC6
      Parameter (SAFETY=0.9,PGROW=-.2,PSHRNK=-.25,ERRCON=1.89e-4)
      Parameter (A2=.2,A3=.3,A4=.6,A5=1.,A6=.875,B21=.2,B31=3./40.,
     1 B32=9./40.,B41=.3,B42=-.9,B43=1.2,B51=-11./54.,B52=2.5,
     1 B53=-70./27.,B54=35./27.,B61=1631./55296.,B62=175./512.,
     1 B63=575./13824.,B64=44275./110592.,B65=253./4096.,
     1 C1=37./378.,C3=250./621.,C4=125./594.,C6=512./1771.,
     1 DC1=C1-2825./27648.,DC3=C3-18575./48384.,
     1 DC4=C4-13525./55296.,DC5=-277./14336.,DC6=C6-.25)

      h=htry

1     DO i=1,n
          ytemp(i)=y(i)+B21*h*dydx(i)
      ENDDO

      CALL derivs(x+A2*h,ytemp,ak2, Xparams)

      DO i=1,n
          ytemp(i)=y(i)+h*(B31*dydx(i)+B32*ak2(i))
      ENDDO

      CALL derivs(x+A3*h,ytemp,ak3, Xparams)

      DO i=1,n
          ytemp(i)=y(i)+h*(B41*dydx(i)+B42*ak2(i)+B43*ak3(i))
      ENDDO

      CALL derivs(x+A4*h,ytemp,ak4, Xparams)

      DO i=1,n
          ytemp(i)=y(i)+h*(B51*dydx(i)+B52*ak2(i)+B53*ak3(i)+
     1 B54*ak4(i))
      ENDDO

      CALL derivs(x+A5*h,ytemp,ak5, Xparams)

      DO i=1,n
          ytemp(i)=y(i)+h*(B61*dydx(i)+B62*ak2(i)+B63*ak3(i)+
     1 B64*ak4(i)+B65*ak5(i))
      ENDDO

      CALL derivs(x+A6*h,ytemp,ak6, Xparams)

      DO i=1,n
```

```
60          yout(i)=y(i)+h*(C1*dydx(i)+C3*ak3(i)+C4*ak4(i)+
        1  C6*ak6(i))
62        ENDDO

64        DO i=1,n
            yerr(i)=h*(DC1*dydx(i)+DC3*ak3(i)+DC4*ak4(i)+DC5*ak5(i)
66      1  +DC6*ak6(i))
          ENDDO
68
          errmax=0.
70
          DO i=1,n
72          errmax=max(errmax,abs(yerr(i)/yscal(i)))
          ENDDO
74
          errmax=errmax/eps
76        IF(errmax.gt.1.)then
            htemp=SAFETY*h*(errmax**PSHRNK)
78          h=sign(max(abs(htemp),0.1*abs(h)),h)
            xnew=x+h
80          IF(xnew.eq.x) then
           pause 'stepsize underflow in rkqs'
82        CALL EXIT(1)
           ENDIF
84          goto 1
          ELSE
86          IF(errmax.gt.ERRCON)then
              hnext=SAFETY*h*(errmax**PGROW)
88          ELSE
              hnext=5.*h
90          ENDIF
            hdid=h
92          x=x+h

94          DO i=1,n
              y(i)=yout(i)
96          ENDDO

98          RETURN
          ENDIF
100
          END SUBROUTINE rkqs
```

B.4.3 Monte Carlo approach

The Monte-Carlo approach is significantly simpler and more intuitive but still adequate for solving the steady state problem. This method still uses a subroutine called ODEINT and the previously described function DERIVS.

```
      SUBROUTINE odeint(ystart,nvar,x1,x2,Xparams)

      INTEGER nvar
      REAL x1,x2,ystart(nvar), xint, xm
      DIMENSION Xparams(10)
      REAL dydx(nvar),y(nvar)

          CALL derivs(x, y, dydx, Xparams)

          xint = x2-x1
          xm = x1 + xint/2

          ystart(1) = ystart(1) + (xint*dydx(1))
          ystart(2) = ystart(2) + (xint*dydx(2))

      END SUBROUTINE odeint

```

B.4.4 General purpose subroutines

In this section are reported some additional subroutines needed for the correct execution of the code.

The LineDelete subroutine simply deletes the last line of the data files if the previous increment failed to converge in order to have the correct data in the output files.

The MecanoSensing subroutine calculates the current ω_{ms} value depending on the current cortical stress σ.

The OsmPressWave gives the external osmotic pressure Π_{ext} and can be adapted to return a constant value or a time-dependent curve depending on the type of simulation at hand.

Finally, the Biosinth subroutine simply calculates the current amount of impermeable biomass n_{imp} at the current time to simulate cell growth if the simulation requires it.

```
      SUBROUTINE LineDelete(lineToRemove)

      REAL TIME, IONS, CURR_VOL, TOTPRESS, OSMPRESS, KINC, CORTSIGMA,
     1     Wms
      INTEGER lineToRemove
      INTEGER inputFile1, TempFile3, lineCounter, inputFile2

      TempFile1 = 108
      TempFile2 = 109
      TempFile3 = 110
      TempFile4 = 111
      TempFile5 = 112
```

```
      inputFile1 = 113
14    inputFile2 = 114
      inputFile3 = 115
16    inputFile4 = 116
      inputFile5 = 117
18

20    open(unit=inputFile1,file='/home/emanuele2013/cell_mech/
      ␣␣␣␣␣1CG/AxOsm7/Data1.dat',status='old', action='READ')
22    open(unit=inputFile2,file='/home/emanuele2013/cell_mech/
      ␣␣␣␣␣1CG/AxOsm7/Data2.dat',status='old', action='READ')
24    open(unit=inputFile3,file='/home/emanuele2013/cell_mech/
      ␣␣␣␣␣1CG/AxOsm7/Data3.dat',status='old', action='READ')
26    open(unit=inputFile4,file='/home/emanuele2013/cell_mech/
      ␣␣␣␣␣1CG/AxOsm7/Data4.dat',status='old', action='READ')
28    open(unit=inputFile5,file='/home/emanuele2013/cell_mech/
      ␣␣␣␣␣1CG/AxOsm7/Data5.dat',status='old', action='READ')
30
      open(unit=TempFile1,file='/home/emanuele2013/cell_mech/
32    ␣␣␣␣␣1CG/AxOsm7/Temp1.dat',status='old', action='WRITE')
      open(unit=TempFile2,file='/home/emanuele2013/cell_mech/
34    ␣␣␣␣␣1CG/AxOsm7/Temp2.dat',status='old', action='WRITE')
      open(unit=TempFile3,file='/home/emanuele2013/cell_mech/
36    ␣␣␣␣␣1CG/AxOsm7/Temp3.dat',status='old', action='WRITE')
      open(unit=TempFile4,file='/home/emanuele2013/cell_mech/
38    ␣␣␣␣␣1CG/AxOsm7/Temp4.dat',status='old', action='WRITE')
      open(unit=TempFile5,file='/home/emanuele2013/cell_mech/
40    ␣␣␣␣␣1CG/AxOsm7/Temp5.dat',status='old', action='WRITE')
      lineCounter = 0
42
      DO
44        READ(inputFile1, *, END=10) TIME, IONS, CURR_VOL, TOTPRESS
          READ(inputFile2, *, END=10) OSMPRESS, KINC, CORTSIGMA, Wms
46        READ(inputFile3, *, END=10) OPext, JWat, J1, J2
          READ(inputFile4, *, END=10) dy1, dy2, Bio
48        READ(inputFile5, *, END=10) xg

50        lineCounter = lineCounter + 1

52        IF (lineCounter .NE. lineToRemove) THEN

54            WRITE(TempFile1, *) TIME, IONS, CURR_VOL, TOTPRESS
              WRITE(TempFile2, *) OSMPRESS, KINC, CORTSIGMA, Wms
56            WRITE(TempFile3, *) OPext, JWat, J1, J2
              WRITE(TempFile4, *) dy1, dy2, Bio
58            WRITE(TempFile5, *) xg

60        ELSE

62        END IF
          END DO
```

```
64
    10 CONTINUE
66
       CLOSE(inputFile1)
68     CLOSE(inputFile2)
       CLOSE(inputFile3)
70     CLOSE(inputFile4)
       CLOSE(inputFile5)
72     CLOSE(TempFile1)
       CLOSE(TempFile2)
74     CLOSE(TempFile3)
       CLOSE(TempFile4)
76     CLOSE(TempFile5)

78     open(unit=inputFile1,file='/home/emanuele2013/cell_mech/
    ␣␣␣␣␣1CG/AxOsm7/Data1.dat',status='old', action='WRITE')
80     open(unit=inputFile2,file='/home/emanuele2013/cell_mech/
    ␣␣␣␣␣1CG/AxOsm7/Data2.dat',status='old', action='WRITE')
82     open(unit=inputFile3,file='/home/emanuele2013/cell_mech/
    ␣␣␣␣␣1CG/AxOsm7/Data3.dat',status='old', action='WRITE')
84     open(unit=inputFile4,file='/home/emanuele2013/cell_mech/
    ␣␣␣␣␣1CG/AxOsm7/Data4.dat',status='old', action='WRITE')
86     open(unit=inputFile5,file='/home/emanuele2013/cell_mech/
    ␣␣␣␣␣1CG/AxOsm7/Data5.dat',status='old', action='WRITE')
88     open(unit=TempFile1,file='/home/emanuele2013/cell_mech/
    ␣␣␣␣␣1CG/AxOsm7/Temp1.dat',status='old', action='READ')
90     open(unit=TempFile2,file='/home/emanuele2013/cell_mech/
    ␣␣␣␣␣1CG/AxOsm7/Temp2.dat',status='old', action='READ')
92     open(unit=TempFile3,file='/home/emanuele2013/cell_mech/
    ␣␣␣␣␣1CG/AxOsm7/Temp3.dat',status='old', action='READ')
94     open(unit=TempFile4,file='/home/emanuele2013/cell_mech/
    ␣␣␣␣␣1CG/AxOsm7/Temp4.dat',status='old', action='READ')
96     open(unit=TempFile5,file='/home/emanuele2013/cell_mech/
    ␣␣␣␣␣1CG/AxOsm7/Temp5.dat',status='old', action='READ')
98     DO
           READ(TempFile1, *, END = 11) TIME, IONS, CURR_VOL, TOTPRESS
100        READ(TempFile2, *, END = 11) OSMPRESS, KINC, CORTSIGMA, Wms
           READ(TempFile3, *, END = 11) OPext, JWat, J1, J2
102        READ(TempFile4, *, END = 11) dy1, dy2, Bio
           READ(TempFile5, *, END = 11) xg
104        WRITE(inputFile1, *) TIME, IONS, CURR_VOL, TOTPRESS
           WRITE(inputFile2, *) OSMPRESS, KINC, CORTSIGMA, Wms
106        WRITE(inputFile3, *) OPext, JWat, J1, J2
           WRITE(inputFile4, *) dy1, dy2, Bio
108        WRITE(inputFile5, *) xg
       END DO
110
    11 CONTINUE
112
       CLOSE(inputFile1)
114    CLOSE(inputFile2)
```

```
      CLOSE(inputFile3)
116   CLOSE(inputFile4)
      CLOSE(inputFile5)
118   CLOSE(TempFile1)
      CLOSE(TempFile2)
120   CLOSE(TempFile3)
    CLOSE(TempFile4)
122   CLOSE(TempFile5)

124   END SUBROUTINE LineDelete


126


128   SUBROUTINE MecanoSensing(Wms, TOTSIGMA)

130   REAL Wms, SigmaC, SigmaS, TOTSIGMA, Beta

132   SigmaC = 7.5e-5
      SigmaS = 6e-4
134   Beta = 2e-5
      IF (TOTSIGMA.LE.SigmaC) THEN
136       Wms = 0
      ELSE IF (TOTSIGMA.GE.SIGMAC .AND. TOTSIGMA.LE.SIGMAS) THEN
138       Wms = Beta*(TOTSIGMA-SIGMAC)
      ELSE IF (TOTSIGMA.GE.SIGMAS) THEN
140       Wms = Beta*(SIGMAS-SIGMAC)
      END IF
142
      END SUBROUTINE MecanoSensing
144


146
      SUBROUTINE OsmPressWave(OPext,K,TChall,tt)
148
      REAL L, M, H, s, q
150   REAL OPext, TChall, tt
      INTEGER K
152   INTEGER ONE, TWO, THREE

154   ONE = 1.0
      TWO = 2.0
156   THREE = 3.0

158   L = 0.3
      H = 0.5
160   M = 0.4

162       IF (K.EQ.ONE) THEN
              OPext = H
164       ELSEIF (K.EQ.TWO) THEN
              IF (tt.LT.TChall/2) THEN
```

```
166                 s = (L-H)*2/TChall
                    q = H
168                 OPext = s*tt + q
                ELSE
170                 OPext = L
                ENDIF
172         ELSEIF (K.EQ.THREE) THEN
                IF (tt.LT.TChall/2) THEN
174                 s = (M-L)*2/TChall
                    q = L
176                 OPext = s*tt + q
                ELSE
178                 OPext = M
                ENDIF
180         ENDIF

182     END SUBROUTINE OsmPressWave


184
        SUBROUTINE Biosinth(TT,TChall,Bio)
186
        REAL BioTarg, K , T
188     REAL Bio, TChall, tt

190     BioTarg = 0
        IF (TT.LT.TChall) THEN
192         Bio = 0
        ELSE
194         K = BioTarg/TChall
            T = TT - TChall
196         Bio = K*T
        END IF
198
        END SUBROUTINE Biosinth
```

References

Akkiraju, H., & Nohe, A. (2015). Role of chondrocytes in cartilage formation, progression of osteoarthritis and cartilage regeneration. *Journal of developmental biology*, *3*(4), 177–192.

Alcaide-Ruggiero, L., Molina-Hernández, V., Granados, M. M., & Domínguez, J. M. (2021). Main and minor types of collagens in the articular cartilage: the role of collagens in repair tissue evaluation in chondral defects. *International Journal of Molecular Sciences*, *22*(24), 13329.

Alexopoulos, L. G., Haider, M. A., Vail, T. P., & Guilak, F. (2003). Alterations in the mechanical properties of the human chondrocyte pericellular matrix with osteoarthritis. *J. Biomech. Eng.*, *125*(3), 323–333.

Alexopoulos, L. G., Setton, L. A., & Guilak, F. (2005). The biomechanical role of the chondrocyte pericellular matrix in articular cartilage. *Acta biomaterialia*, *1*(3), 317–325.

Alexopoulos, L. G., Williams, G. M., Upton, M. L., Setton, L. A., & Guilak, F. (2005). Osteoarthritic changes in the biphasic mechanical properties of the chondrocyte pericellular matrix in articular cartilage. *Journal of biomechanics*, *38*(3), 509–517.

Alibert, C., Goud, B., & Manneville, J.-B. (2017). Are cancer cells really softer than normal cells? *Biology of the Cell*, *109*(5), 167–189.

Allen, D. M., & Mao, J. J. (2004). Heterogeneous nanostructural and nanoelastic properties of pericellular and interterritorial matrices of chondrocytes by atomic force microscopy. *Journal of structural biology*, *145*(3), 196–204.

Apodaca, G. (2002). Modulation of membrane traffic by mechanical stimuli. *American Journal of Physiology-Renal Physiology*, *282*(2), F179–F190.

Arduino, A., Pettenuzzo, S., Berardo, A., Salomoni, V. A., Majorana, C., & Carniel, E. L. (2022). A continuum-tensegrity computational model for chondrocyte biomechanics in afm indentation and micropipette aspiration. *Annals of Biomedical Engineering*, *50*(12), 1911–1922.

Ateshian, G. A., Chahine, N. O., Basalo, I. M., & Hung, C. T. (2004). The correspondence between equilibrium biphasic and triphasic material properties in mixture models of articular cartilage. *Journal of biomechanics*, *37*(3), 391–400.

Baaijens, F. P., Trickey, W. R., Laursen, T. A., & Guilak, F. (2005). Large deformation finite element analysis of micropipette aspiration to determine the mechanical properties of the chondrocyte. *Annals of biomedical engineering*, *33*, 494–501.

Bader, D., Ohashi, T., Knight, M., Lee, D., & Sato, M. (2002). Deformation properties of articular chondrocytes: a critique of three separate techniques. *Biorheology*, *39*(1-2), 69–78.

Banerjee, A., Khan, M. P., Barui, A., Datta, P., Chowdhury, A. R., & Bhowmik, K. (2022). Finite element analysis of the influence of cyclic strain on cells anchored to substrates with varying properties. *Medical & Biological Engineering*

& Computing, *60*, 171–187.

Bansod, Y. D., & Bursa, J. (2015). Continuum-based modelling approaches for cell mechanics. *International Journal of Bioengineering and Life Sciences*, *9*(9), 969–980.

Bansod, Y. D., Matsumoto, T., Nagayama, K., & Bursa, J. (2018). A finite element bendo-tensegrity model of eukaryotic cell. *Journal of biomechanical engineering*, *140*(10), 101001.

Barreto, S., Clausen, C. H., Perrault, C. M., Fletcher, D. A., & Lacroix, D. (2013). A multi-structural single cell model of force-induced interactions of cytoskeletal components. *Biomaterials*, *34*(26), 6119–6126.

Barreto, S., Perrault, C. M., & Lacroix, D. (2014). Structural finite element analysis to explain cell mechanics variability. *Journal of the Mechanical Behavior of biomedical materials*, *38*, 219–231.

Battistelli, M., Favero, M., Burini, D., Trisolino, G., Dallari, D., De Franceschi, L., ... others (2019). Morphological and ultrastructural analysis of normal, injured and osteoarthritic human knee menisci. *European Journal of Histochemistry: EJH*, *63*(1).

Bausch, A. R., Ziemann, F., Boulbitch, A. A., Jacobson, K., & Sackmann, E. (1998). Local measurements of viscoelastic parameters of adherent cell surfaces by magnetic bead microrheometry. *Biophysical journal*, *75*(4), 2038–2049.

Belluzzi, E., El Hadi, H., Granzotto, M., Rossato, M., Ramonda, R., Macchi, V., ... Favero, M. (2017). Systemic and local adipose tissue in knee osteoarthritis. *Journal of Cellular Physiology*, *232*(8), 1971–1978.

Belluzzi, E., Olivotto, E., Toso, G., Cigolotti, A., Pozzuoli, A., Biz, C., ... others (2019). Conditioned media from human osteoarthritic synovium induces inflammation in a synoviocyte cell line. *Connective Tissue Research*, *60*(2), 136–145.

Belluzzi, E., Stocco, E., Pozzuoli, A., Granzotto, M., Porzionato, A., Vettor, R., ... others (2019). Contribution of infrapatellar fat pad and synovial membrane to knee osteoarthritis pain. *BioMed research international*, *2019*.

Belluzzi, E., Todros, S., Pozzuoli, A., Ruggieri, P., Carniel, E. L., & Berardo, A. (2023). Human cartilage biomechanics: Experimental and theoretical approaches towards the identification of mechanical properties in healthy and osteoarthritic conditions. *Processes*, *11*(4), 1014.

Benninghoff, A. (1925). Form und bau der gelenkknorpel in ihren beziehungen zur funktion: Zweiter teil: Der aufbau des gelenkknorpels in seinen beziehungen zur funktion. *Zeitschrift für Zellforschung und mikroskopische Anatomie*, *2*(5), 783–862.

Berardo, A., & Pugno, N. M. (2020). A model for hierarchical anisotropic friction, adhesion and wear. *Tribology International*, *152*, 106549.

Bhosale, A. M., & Richardson, J. B. (2008). Articular cartilage: structure, injuries and review of management. *British medical bulletin*, *87*(1), 77–95.

Bob Burkhardt. (2004a). *Tensegrity 3-prism.* Retrieved from `https://commons`

.wikimedia.org/wiki/File:Tensegrity_3-Prism.png ([Online; accessed 14-06-23])

Bob Burkhardt. (2004b). *Tensegrity tetrahedron.* Retrieved from https://commons.wikimedia.org/wiki/File:Tensegrity_Tetrahedron.png ([Online; accessed 14-06-23])

Bursa, J., Lebis, R., & Holata, J. (2012). Tensegrity finite element models of mechanical tests of individual cells. *Technology and Health Care*, *20*(2), 135–150.

Butcher, D. T., Alliston, T., & Weaver, V. M. (2009). A tense situation: forcing tumour progression. *Nature Reviews Cancer*, *9*(2), 108–122.

Caille, N., Thoumine, O., Tardy, Y., & Meister, J.-J. (2002). Contribution of the nucleus to the mechanical properties of endothelial cells. *Journal of biomechanics*, *35*(2), 177–187.

Carter, D. R., Beaupré, G. S., Giori, N. J., & Helms, J. A. (1998). Mechanobiology of skeletal regeneration. *Clinical Orthopaedics and Related Research (1976-2007)*, *355*, S41–S55.

Chahine, N. O., Blanchette, C., Thomas, C. B., Lu, J., Haudenschild, D., & Loots, G. G. (2013). Effect of age and cytoskeletal elements on the indentation-dependent mechanical properties of chondrocytes. *PloS one*, *8*(4), e61651.

Chen, C., Tambe, D. T., Deng, L., & Yang, L. (2013). Biomechanical properties and mechanobiology of the articular chondrocyte. *American Journal of Physiology-Cell Physiology*, *305*(12), C1202–C1208.

Chen, D., Shen, J., Zhao, W., Wang, T., Han, L., Hamilton, J. L., & Im, H.-J. (2017). Osteoarthritis: toward a comprehensive understanding of pathological mechanism. *Bone research*, *5*(1), 1–13.

Chen, J., & Lu, G. (2012). Finite element modelling of nanoindentation based methods for mechanical properties of cells. *Journal of biomechanics*, *45*(16), 2810–2816.

Chery, D. R., Han, B., Li, Q., Zhou, Y., Heo, S.-J., Kwok, B., ... others (2020). Early changes in cartilage pericellular matrix micromechanobiology portend the onset of post-traumatic osteoarthritis. *Acta biomaterialia*, *111*, 267–278.

Chicurel, M. E., Chen, C. S., & Ingber, D. E. (1998). Cellular control lies in the balance of forces. *Current opinion in cell biology*, *10*(2), 232–239.

Darling, E., Zauscher, S., & Guilak, F. (2006). Viscoelastic properties of zonal articular chondrocytes measured by atomic force microscopy. *Osteoarthritis and cartilage*, *14*(6), 571–579.

Darling, E. M., Topel, M., Zauscher, S., Vail, T. P., & Guilak, F. (2008). Viscoelastic properties of human mesenchymally-derived stem cells and primary osteoblasts, chondrocytes, and adipocytes. *Journal of biomechanics*, *41*(2), 454–464.

Darling, E. M., Wilusz, R. E., Bolognesi, M. P., Zauscher, S., & Guilak, F. (2010). Spatial mapping of the biomechanical properties of the pericellular matrix of articular cartilage measured in situ via atomic force microscopy. *Biophysical journal*, *98*(12), 2848–2856.

Darling, E. M., Zauscher, S., Block, J. A., & Guilak, F. (2007). A thin-layer model for

viscoelastic, stress-relaxation testing of cells using atomic force microscopy: do cell properties reflect metastatic potential? *Biophysical journal*, *92*(5), 1784–1791.

Davidson, M. W. (2000). *The cell nucleus.* Florida State University. Retrieved from `https://micro.magnet.fsu.edu/cells/nucleus/nucleus.html`

Desai, A., & Mitchison, T. J. (1997). Microtubule polymerization dynamics. *Annual review of cell and developmental biology*, *13*(1), 83–117.

Dimitrov, A., Quesnoit, M., Moutel, S., Cantaloube, I., Pous, C., & Perez, F. (2008). Detection of gtp-tubulin conformation in vivo reveals a role for gtp remnants in microtubule rescues. *science*, *322*(5906), 1353–1356.

Discher, D. E., Janmey, P., & Wang, Y.-l. (2005). Tissue cells feel and respond to the stiffness of their substrate. *Science*, *310*(5751), 1139–1143.

Donell, S. (2019). Subchondral bone remodelling in osteoarthritis. *EFORT Open Reviews*, *4*(6), 221–229.

Dowling, E. P., Ronan, W., Ofek, G., Deshpande, V. S., McMeeking, R. M., Athanasiou, K. A., & McGarry, J. P. (2012). The effect of remodelling and contractility of the actin cytoskeleton on the shear resistance of single cells: a computational and experimental investigation. *Journal of The Royal Society Interface*, *9*(77), 3469–3479.

Du, G., Li, L., Zhang, X., Liu, J., Hao, J., Zhu, J., ... Zhang, Q. (2020). Roles of trpv4 and piezo channels in stretch-evoked ca2+ response in chondrocytes. *Experimental Biology and Medicine*, *245*(3), 180–189.

Efremov, Y. M., Wang, W.-H., Hardy, S. D., Geahlen, R. L., & Raman, A. (2017). Measuring nanoscale viscoelastic parameters of cells directly from afm force-displacement curves. *Scientific reports*, *7*(1), 1541.

Emmi, A., Stocco, E., Boscolo-Berto, R., Contran, M., Belluzzi, E., Favero, M., ... others (2022). Infrapatellar fat pad-synovial membrane anatomo-fuctional unit: microscopic basis for piezo1/2 mechanosensors involvement in osteoarthritis pain. *Frontiers in Cell and Developmental Biology*, *10*, 886604.

Englund, M. (2023). Osteoarthritis, part of life or a curable disease? a bird's-eye view. *Journal of Internal Medicine*.

Englund, M., Guermazi, A., & Lohmander, S. L. (2009). The role of the meniscus in knee osteoarthritis: a cause or consequence? *Radiologic Clinics*, *47*(4), 703–712.

Evans, E., & Yeung, A. (1989). Apparent viscosity and cortical tension of blood granulocytes determined by micropipet aspiration. *Biophysical journal*, *56*(1), 151–160.

Favero, M., Belluzzi, E., Ortolan, A., Lorenzin, M., Oliviero, F., Doria, A., ... Ramonda, R. (2022). Erosive hand osteoarthritis: latest findings and outlook. *Nature Reviews Rheumatology*, *18*(3), 171–183.

Favero, M., Belluzzi, E., Trisolino, G., Goldring, M. B., Goldring, S. R., Cigolotti, A., ... others (2019). Inflammatory molecules produced by meniscus and synovium in early and end-stage osteoarthritis: a coculture study. *Journal of cellular physiology*, *2*(16072), 11176–11187.

Fedorchak, G. R., Kaminski, A., & Lammerding, J. (2014). Cellular mechanosensing: getting to the nucleus of it all. *Progress in biophysics and molecular biology*, *115*(2-3), 76–92.

Florea, C., Jakorinne, A., Lammi, M., Davidescu, A., & Korhonen, R. K. (2014). Determination of mechanical properties of chondrocytes in articular cartilage using atomic force microscopy. *Solid State Phenomena*, *216*, 134–139.

Florea, C., Tanska, P., Mononen, M. E., Qu, C., Lammi, M. J., Laasanen, M. S., & Korhonen, R. K. (2017). A combined experimental atomic force microscopy-based nanoindentation and computational modeling approach to unravel the key contributors to the time-dependent mechanical behavior of single cells. *Biomechanics and modeling in mechanobiology*, *16*, 297–311.

Fontanella, C. G., Belluzzi, E., Pozzuoli, A., Favero, M., Ruggieri, P., Macchi, V., & Carniel, E. L. (2022). Mechanical behavior of infrapatellar fat pad of patients affected by osteoarthritis. *Journal of Biomechanics*, *131*, 110931.

Fraldi, M., Palumbo, S., Carotenuto, A. R., Cutolo, A., Deseri, L., & Pugno, N. (2019). Buckling soft tensegrities: Fickle elasticity and configurational switching in living cells. *Journal of the Mechanics and Physics of Solids*, *124*, 299–324.

Freeman, P., Natarajan, R., Kimura, J., & Andriacchi, T. (1994). Chondrocyte cells respond mechanically to compressive loads. *Journal of Orthopaedic Research*, *12*(3), 311–320.

Gao, J., Sun, X., Moore, L. C., White, T. W., Brink, P. R., & Mathias, R. T. (2011). Lens intracellular hydrostatic pressure is generated by the circulation of sodium and modulated by gap junction coupling. *Journal of General Physiology*, *137*(6), 507–520.

Garcia, P. D., & Garcia, R. (2018). Determination of the viscoelastic properties of a single cell cultured on a rigid support by force microscopy. *Nanoscale*, *10*(42), 19799–19809.

Garcia, P. D., Guerrero, C. R., & Garcia, R. (2020). Nanorheology of living cells measured by afm-based force–distance curves. *Nanoscale*, *12*(16), 9133–9143.

Gavara, N., & Chadwick, R. S. (2012). Determination of the elastic moduli of thin samples and adherent cells using conical atomic force microscope tips. *Nature nanotechnology*, *7*(11), 733–736.

Gilbert, S. J., & Blain, E. J. (2018). Cartilage mechanobiology: How chondrocytes respond to mechanical load. In *Mechanobiology in health and disease* (pp. 99–126). Elsevier.

Gittes, F., Mickey, B., Nettleton, J., & Howard, J. (1993). Flexural rigidity of microtubules and actin filaments measured from thermal fluctuations in shape. *The Journal of cell biology*, *120*(4), 923–934.

Gladilin, E., Micoulet, A., Hosseini, B., Rohr, K., Spatz, J., & Eils, R. (2007). 3d finite element analysis of uniaxial cell stretching: from image to insight. *Physical biology*, *4*(2), 104.

GM., C. (2000). *The cell: A molecular approach.* (2nd ed.). Sunderland, MA: Sinauer

Associates. Retrieved from https://www.ncbi.nlm.nih.gov/books/NBK9908/

Goldring, M. B. (2012). *Articular cartilage degradation in osteoarthritis.* SAGE Publications Sage CA: Los Angeles, CA.

Goldring, M. B., & Marcu, K. B. (2009). Cartilage homeostasis in health and rheumatic diseases. *Arthritis research & therapy*, *11*(3), 1–16.

González-Bermúdez, B., Guinea, G. V., & Plaza, G. R. (2019). Advances in micropipette aspiration: applications in cell biomechanics, models, and extended studies. *Biophysical Journal*, *116*(4), 587–594.

Goodman, S. R. (2007). *Medical cell biology* (3rd ed.). Academic Press.

Graff, R. D., Kelley, S. S., & Lee, G. M. (2003). Role of pericellular matrix in development of a mechanically functional neocartilage. *Biotechnology and bioengineering*, *82*(4), 457–464.

Griffin, T. M., & Guilak, F. (2005). The role of mechanical loading in the onset and progression of osteoarthritis. *Exercise and sport sciences reviews*, *33*(4), 195–200.

Grodzinsky, A. J., Levenston, M. E., Jin, M., & Frank, E. H. (2000). Cartilage tissue remodelling in response to mechanical forces. *Annual review of biomedical engineering*, *2*(1), 691–713.

Guilak, F. (2000). The deformation behavior and viscoelastic properties of chondrocytes in articular cartilage. *Biorheology*, *37*(1-2), 27–44.

Guilak, F., Alexopoulos, L. G., Haider, M. A., Ting-Beall, H. P., & Setton, L. A. (2005). Zonal uniformity in mechanical properties of the chondrocyte pericellular matrix: micropipette aspiration of canine chondrons isolated by cartilage homogenization. *Annals of biomedical engineering*, *33*, 1312–1318.

Guilak, F., Alexopoulos, L. G., Upton, M. L., Youn, I., Choi, J. B., Cao, L., ... Haider, M. A. (2006). The pericellular matrix as a transducer of biomechanical and biochemical signals in articular cartilage. *Annals of the New York Academy of Sciences*, *1068*(1), 498–512.

Guilak, F., & Mow, V. C. (2000). The mechanical environment of the chondrocyte: a biphasic finite element model of cell–matrix interactions in articular cartilage. *Journal of biomechanics*, *33*(12), 1663–1673.

Guilak, F., Nims, R. J., Dicks, A., Wu, C.-L., & Meulenbelt, I. (2018). Osteoarthritis as a disease of the cartilage pericellular matrix. *Matrix Biology*, *71*, 40–50.

Guilak, F., Ratcliffe, A., & Mow, V. C. (1995). Chondrocyte deformation and local tissue strain in articular cartilage: a confocal microscopy study. *Journal of Orthopaedic Research*, *13*(3), 410–421.

Guilak, F., Tedrow, J. R., & Burgkart, R. (2000). Viscoelastic properties of the cell nucleus. *Biochemical and biophysical research communications*, *269*(3), 781–786.

Han, S.-K., Madden, R., Abusara, Z., & Herzog, W. (2012). In situ chondrocyte viscoelasticity. *Journal of biomechanics*, *45*(14), 2450–2456.

Hao, Y., Cheng, S., Tanaka, Y., Hosokawa, Y., Yalikun, Y., & Li, M. (2020). Mechanical properties of single cells: Measurement methods and applications. *Biotechnology Advances*, *45*, 107648.

Herrmann, H., Kreplak, L., & Aebi, U. (2004). Isolation, characterization, and in vitro assembly of intermediate filaments. In *Methods in cell biology* (Vol. 78, pp. 3–24). Elsevier.

Hing, W., Sherwin, A., Ross, J., & Poole, C. (2002). The influence of the pericellular microenvironment on the chondrocyte response to osmotic challenge. *Osteoarthritis and cartilage*, *10*(4), 297–307.

Hogan, B., Babataheri, A., Hwang, Y., Barakat, A. I., & Husson, J. (2015). Characterizing cell adhesion by using micropipette aspiration. *Biophysical journal*, *109*(2), 209–219.

Hohmann, T., & Dehghani, F. (2019). The cytoskeleton—a complex interacting meshwork. *Cells*, *8*(4), 362.

Hsieh, C.-H., Lin, Y.-H., Lin, S., Tsai-Wu, J.-J., Wu, C. H., & Jiang, C.-C. (2008). Surface ultrastructure and mechanical property of human chondrocyte revealed by atomic force microscopy. *Osteoarthritis and cartilage*, *16*(4), 480–488.

Hu, J., Jafari, S., Han, Y., Grodzinsky, A. J., Cai, S., & Guo, M. (2017). Size-and speed-dependent mechanical behavior in living mammalian cytoplasm. *Proceedings of the national Academy of Sciences*, *114*(36), 9529–9534.

Huang, H., Kamm, R. D., & Lee, R. T. (2004). Cell mechanics and mechanotransduction: pathways, probes, and physiology. *American Journal of Physiology-Cell Physiology*, *287*(1), C1–C11.

Ingber, D. (2003). Mechanobiology and diseases of mechanotransduction. *Annals of medicine*, *35*(8), 564–577.

Ingber, D. E. (1997). Tensegrity: the architectural basis of cellular mechanotransduction. *Annual review of physiology*, *59*(1), 575–599.

Ingber, D. E. (2003a). Tensegrity i. cell structure and hierarchical systems biology. *Journal of cell science*, *116*(7), 1157–1173.

Ingber, D. E. (2003b). Tensegrity ii. how structural networks influence cellular information processing networks. *Journal of cell science*, *116*(8), 1397–1408.

Irianto, J., Ramaswamy, G., Serra, R., & Knight, M. M. (2014). Depletion of chondrocyte primary cilia reduces the compressive modulus of articular cartilage. *Journal of biomechanics*, *47*(2), 579–582.

Janmey, P. A., & McCulloch, C. A. (2007). Cell mechanics: integrating cell responses to mechanical stimuli. *Annu. Rev. Biomed. Eng.*, *9*, 1–34.

Jiang, H., Jiang, L., Posner, J. D., & Vogt, B. D. (2008). Atomistic-based continuum constitutive relation for microtubules: elastic modulus prediction. *Computational Mechanics*, *42*, 607–618.

Jiang, H., & Sun, S. X. (2013). Cellular pressure and volume regulation and implications for cell mechanics. *Biophysical journal*, *105*(3), 609–619.

Jones, W. R., Ting-Beall, H. P., Lee, G. M., Kelley, S. S., Hochmuth, R. M., & Guilak, F. (1999). Alterations in the young's modulus and volumetric properties of chondrocytes isolated from normal and osteoarthritic human cartilage. *Journal of biomechanics*, *32*(2), 119–127.

Julkunen, P., Wilson, W., Jurvelin, J. S., & Korhonen, R. K. (2009). Composition of the pericellular matrix modulates the deformation behaviour of chondrocytes in articular cartilage under static loading. *Medical & biological engineering & computing*, *47*, 1281–1290.

Kadzik, R. S., Homa, K. E., & Kovar, D. R. (2020). F-actin cytoskeleton network self-organization through competition and cooperation. *Annual review of cell and developmental biology*, *36*, 35–60.

Kandoth, C., McLellan, M. D., Vandin, F., Ye, K., Niu, B., Lu, C., ... others (2013). Mutational landscape and significance across 12 major cancer types. *Nature*, *502*(7471), 333–339.

Kassebaum, N. J., Arora, M., Barber, R. M., Bhutta, Z. A., Brown, J., Carter, A., ... others (2016). Global, regional, and national disability-adjusted life-years (dalys) for 315 diseases and injuries and healthy life expectancy (hale), 1990–2015: a systematic analysis for the global burden of disease study 2015. *The Lancet*, *388*(10053), 1603–1658.

Kasza, K. E., Rowat, A. C., Liu, J., Angelini, T. E., Brangwynne, C. P., Koenderink, G. H., & Weitz, D. A. (2007). The cell as a material. *Current opinion in cell biology*, *19*(1), 101–107.

Katti, D. R., & Katti, K. S. (2017). Cancer cell mechanics with altered cytoskeletal behavior and substrate effects: A 3d finite element modeling study. *Journal of the mechanical behavior of biomedical materials*, *76*, 125–134.

Kelly, T.-A. N., Wang, C. C.-B., Mauck, R. L., Ateshian, G. A., & Hung, C. T. (2004). Role of cell-associated matrix in the development of free-swelling and dynamically loaded chondrocyte-seeded agarose gels. *Biorheology*, *41*(3-4), 223–237.

Khatau, S. B., Hale, C. M., Stewart-Hutchinson, P., Patel, M. S., Stewart, C. L., Searson, P. C., ... Wirtz, D. (2009). A perinuclear actin cap regulates nuclear shape. *Proceedings of the National Academy of Sciences*, *106*(45), 19017–19022.

Khoshgoftar, M., Torzilli, P. A., & Maher, S. A. (2018). Influence of the pericellular and extracellular matrix structural properties on chondrocyte mechanics. *Journal of Orthopaedic Research®*, *36*(2), 721–729.

Khunsaraki, G. M., Oscuii, H. N., & Voloshin, A. (2020). Study of the mechanical behavior of subcellular organelles using a 3d finite element model of the tensegrity structure. *Applied Sciences*, *11*(1), 249.

Knight, M., Ross, J., Sherwin, A., Lee, D., Bader, D., & Poole, C. (2001). Chondrocyte deformation within mechanically and enzymatically extracted chondrons compressed in agarose. *Biochimica et Biophysica Acta (BBA)-General Subjects*, *1526*(2), 141–146.

Koay, E. J., Shieh, A. C., & Athanasiou, K. A. (2003). Creep indentation of single cells. *J. Biomech. Eng.*, *125*(3), 334–341.

Kovar, D. R., Harris, E. S., Mahaffy, R., Higgs, H. N., & Pollard, T. D. (2006). Control of the assembly of atp-and adp-actin by formins and profilin. *Cell*, *124*(2), 423–435.

Kwapiszewska, K., Szczepannski, K., Kalwarczyk, T., Michalska, B., Patalas-Krawczyk,

P., Szymannski, J., ... Hołyst, R. (2020). Nanoscale viscosity of cytoplasm is conserved in human cell lines. *The Journal of Physical Chemistry Letters*, *11*(16), 6914–6920.

Lee, G., Paul, T., Slabaugh, M., & Kelley, S. (2000). The incidence of enlarged chondrons in normal and osteoarthritic human cartilage and their relative matrix density. *Osteoarthritis and cartilage*, *8*(1), 44–52.

Lee, W., Nims, R. J., Savadipour, A., Zhang, Q., Leddy, H. A., Liu, F., ... Liedtke, W. B. (2021). Inflammatory signaling sensitizes piezo1 mechanotransduction in articular chondrocytes as a pathogenic feed-forward mechanism in osteoarthritis. *Proceedings of the National Academy of Sciences*, *118*(13), e2001611118.

Leipzig, N. D., & Athanasiou, K. A. (2005). Unconfined creep compression of chondrocytes. *Journal of biomechanics*, *38*(1), 77–85.

Lekka, M., Laidler, P., Gil, D., Lekki, J., Stachura, Z., & Hrynkiewicz, A. (1999). Elasticity of normal and cancerous human bladder cells studied by scanning force microscopy. *European Biophysics Journal*, *28*, 312–316.

Libertas Academica. (3 September 2015). *Breast cancer metastasis.* Retrieved from `https://commons.wikimedia.org/wiki/File:Figure_1_from_%27Targeting_Breast_Cancer_Metastasis_%2820911418040%29.jpg` ([Online; accessed 19-06-23])

Liu, C., Wang, B., Xiao, L., Li, Y., Xu, L., Zhao, Z., & Zhang, L. (2018). Protective effects of the pericellular matrix of chondrocyte on articular cartilage against the development of osteoarthritis.

Liu, H., Hu, J., Zheng, Q., Feng, X., Zhan, F., Wang, X., ... Hua, F. (2022). Piezo1 channels as force sensors in mechanical force-related chronic inflammation. *Frontiers in Immunology*, *13*, 816149.

Liu, S., Tao, R., Wang, M., Tian, J., Genin, G. M., Lu, T. J., & Xu, F. (2019). Regulation of cell behavior by hydrostatic pressure. *Applied Mechanics Reviews*, *71*(4), 040803.

Liu, Y., Mollaeian, K., & Ren, J. (2019). Finite element modeling of living cells for afm indentation-based biomechanical characterization. *Micron*, *116*, 108–115.

Loeser, R. F. (2013). Aging processes and the development of osteoarthritis. *Current opinion in rheumatology*, *25*(1), 108.

Loeser, R. F. (2017). The role of aging in the development of osteoarthritis. *Transactions of the American Clinical and Climatological Association*, *128*, 44.

Loeser, R. F., Goldring, S. R., Scanzello, C. R., & Goldring, M. B. (2012). Osteoarthritis: a disease of the joint as an organ. *Arthritis and rheumatism*, *64*(6), 1697.

Long, H., Liu, Q., Yin, H., Wang, K., Diao, N., Zhang, Y., ... Guo, A. (2022). Prevalence trends of site-specific osteoarthritis from 1990 to 2019: findings from the global burden of disease study 2019. *Arthritis & Rheumatology*, *74*(7), 1172–1183.

Lorenzo, P., Bayliss, M. T., & Heinegård, D. (2004). Altered patterns and synthesis of extracellular matrix macromolecules in early osteoarthritis. *Matrix Biology*,

23(6), 381–391.

Luby-Phelps, K. (1994). Physical properties of cytoplasm. *Current opinion in cell biology*, *6*(1), 3–9.

Lykov, K., Nematbakhsh, Y., Shang, M., Lim, C. T., & Pivkin, I. V. (2017). Probing eukaryotic cell mechanics via mesoscopic simulations. *PLoS Computational Biology*, *13*(9), e1005726.

M. Steger et al. (2015). *Schematic representation of the nucelus-cytoskeleton-ecm linkage.* Retrieved from `https://www.ncbi.nlm.nih.gov/books/NBK321728/` ([From the book: Optically Induced Nanostructures: Biomedical and Technical Applications; Chapter 2. Online; accessed 10-2-23])

Maître, J.-L., Berthoumieux, H., Krens, S. F. G., Salbreux, G., Jülicher, F., Paluch, E., & Heisenberg, C.-P. (2012). Adhesion functions in cell sorting by mechanically coupling the cortices of adhering cells. *science*, *338*(6104), 253–256.

Maldonado, M., Nam, J., et al. (2013). The role of changes in extracellular matrix of cartilage in the presence of inflammation on the pathology of osteoarthritis. *BioMed research international*, *2013*.

Martel-Pelletier, J., Barr, A. J., Cicuttini, F. M., Conaghan, P. G., Cooper, C., Goldring, M. B., ... Pelletier, J. P. (2016). Osteoarthritis. *Nature reviews. Disease primers*, *2*(7).

Martínez-Moreno, D., Jiménez, G., Gálvez-Martín, P., Rus, G., & Marchal, J. (2019). Cartilage biomechanics: a key factor for osteoarthritis regenerative medicine. *Biochimica et Biophysica Acta (BBA)-Molecular Basis of Disease*, *1865*(6), 1067–1075.

Masson, A. O., & Krawetz, R. J. (2020). Understanding cartilage protection in oa and injury: a spectrum of possibilities. *BMC Musculoskeletal Disorders*, *21*(1), 1–11.

McEvoy, E., Deshpande, V. S., & McGarry, P. (2017). Free energy analysis of cell spreading. *Journal of the mechanical behavior of biomedical materials*, *74*, 283–295.

McEvoy, E., Han, Y. L., Guo, M., & Shenoy, V. B. (2020). Gap junctions amplify spatial variations in cell volume in proliferating tumor spheroids. *Nature communications*, *11*(1), 1–11.

McGarry, J., Prendergast, P., et al. (2004). A three-dimensional finite element model of an adherent eukaryotic cell. *Eur Cell Mater*, *7*, 27–33.

McGlashan, S., Cluett, E., Jensen, C., & Poole, C. (2008). Primary cilia in osteoarthritic chondrocytes: from chondrons to clusters. *Developmental dynamics: an official publication of the American Association of Anatomists*, *237*(8), 2013–2020.

McGlashan, S. R., Jensen, C. G., & Poole, C. A. (2006). Localization of extracellular matrix receptors on the chondrocyte primary cilium. *Journal of Histochemistry & Cytochemistry*, *54*(9), 1005–1014.

McLeod, M. A., Wilusz, R. E., & Guilak, F. (2013). Depth-dependent anisotropy of the micromechanical properties of the extracellular and pericellular matrices of articular cartilage evaluated via atomic force microscopy. *Journal of biomechanics*,

46(3), 586–592.

Melanie Barzik. (2017). *Fluorecent image of the cell microtubules network.* Retrieved from `https://www.flickr.com/photos/nihgov/42111492701` ([Credit: Melanie Barzik, Ph.D., National Institute on Deafness and Other Communication Disorders, NIH. Online; accessed 6-3-23])

Miettinen, T. P., Ly, K. S., Lam, A., & Manalis, S. R. (2022). Single-cell monitoring of dry mass and dry mass density reveals exocytosis of cellular dry contents in mitosis. *Elife*, *11*, e76664.

Mijailovich, S. M., Kojic, M., Zivkovic, M., Fabry, B., & Fredberg, J. J. (2002). A finite element model of cell deformation during magnetic bead twisting. *Journal of Applied Physiology*, *93*(4), 1429–1436.

Mohammadi, H., & Sahai, E. (2018). Mechanisms and impact of altered tumour mechanics. *Nature cell biology*, *20*(7), 766–774.

Morgenroth, D. C., Gellhorn, A. C., & Suri, P. (2012). Osteoarthritis in the disabled population: a mechanical perspective. *PM&R*, *4*(5), S20–S27.

Ng, L., Hung, H.-H., Sprunt, A., Chubinskaya, S., Ortiz, C., & Grodzinsky, A. (2007). Nanomechanical properties of individual chondrocytes and their developing growth factor-stimulated pericellular matrix. *Journal of biomechanics*, *40*(5), 1011–1023.

Nguyen, B. V., Wang, Q., Kuiper, N. J., El Haj, A. J., Thomas, C. R., & Zhang, Z. (2009). Strain-dependent viscoelastic behaviour and rupture force of single chondrocytes and chondrons under compression. *Biotechnology letters*, *31*, 803–809.

Nguyen, B. V., Wang, Q. G., Kuiper, N. J., El Haj, A. J., Thomas, C. R., & Zhang, Z. (2010). Biomechanical properties of single chondrocytes and chondrons determined by micromanipulation and finite-element modelling. *Journal of The Royal Society Interface*, *7*(53), 1723–1733.

Nguyen, T. D., & Gu, Y. (2014). Determination of strain-rate-dependent mechanical behavior of living and fixed osteocytes and chondrocytes using atomic force microscopy and inverse finite element analysis. *Journal of biomechanical engineering*, *136*(10), 101004.

Nicolson, G. L., & de Mattos, G. F. (2023). The fluid–mosaic model of cell membranes: A brief introduction, historical features, some general principles, and its adaptation to current information. *Biochimica et Biophysica Acta (BBA)-Biomembranes*, 184135.

O'Connor, C., Adams, J. U., & Fairman, J. E. (2010). *Essentials of cell biology.* Cambridge, MA: NPG Education. Retrieved from `https://www.nature.com/scitable/ebooks/essentials-of-cell-biology-14749010/118240354/`

Ofek, G., Natoli, R. M., & Athanasiou, K. A. (2009). In situ mechanical properties of the chondrocyte cytoplasm and nucleus. *Journal of biomechanics*, *42*(7), 873–877.

Ofek, G., Wiltz, D. C., & Athanasiou, K. A. (2009). Contribution of the cytoskeleton to the compressive properties and recovery behavior of single cells. *Biophysical journal*, *97*(7), 1873–1882.

Ohashi, T., Hagiwara, M., Bader, D., & Knight, M. (2006). Intracellular mechanics and mechanotransduction associated with chondrocyte deformation during pipette aspiration. *Biorheology*, *43*(3-4), 201–214.

Olivotto, E., Belluzzi, E., Pozzuoli, A., Cigolotti, A., Scioni, M., Goldring, S. R., ... others (2022). Do synovial inflammation and meniscal degeneration impact clinical outcomes of patients undergoing arthroscopic partial meniscectomy? a histological study. *International Journal of Molecular Sciences*, *23*(7), 3903.

OpenStax. (18 May 2016a). *Eukaryote and its subcomponents.* Retrieved from `https://cnx.org/contents/FPtK1zmh@8.25:fEI3C8Ot@10/Preface` ([Online; accessed 06-12-22])

OpenStax. (18 May 2016b). *Ligan-gated channels of the cell membrane.* Retrieved from `https://cnx.org/contents/FPtK1zmh@8.25:fEI3C8Ot@10/Preface` ([Online; accessed 07-12-22])

OpenStax. (18 May 2016c). *Mecano-sensitive channels of the cell membrane.* Retrieved from `https://cnx.org/contents/FPtK1zmh@8.25:fEI3C8Ot@10/Preface` ([Online; accessed 07-12-22])

OpenStax. (18 May 2016d). *Schematic representation of the cell membrane.* Retrieved from `https://cnx.org/contents/FPtK1zmh@8.25:fEI3C8Ot@10/Preface` ([Online; accessed 11-4-23])

OpenStax. (18 May 2016e). *Schematic representation of the cell nucleus.* Retrieved from `https://cnx.org/contents/FPtK1zmh@8.25:fEI3C8Ot@10/Preface` ([Online; accessed 19-5-23])

Palazzo, C., Nguyen, C., Lefevre-Colau, M.-M., Rannou, F., & Poiraudeau, S. (2016). Risk factors and burden of osteoarthritis. *Annals of physical and rehabilitation medicine*, *59*(3), 134–138.

Panciera, T., Citron, A., Di Biagio, D., Battilana, G., Gandin, A., Giulitti, S., ... others (2020). Reprogramming normal cells into tumour precursors requires ecm stiffness and oncogene-mediated changes of cell mechanical properties. *Nature materials*, *19*(7), 797–806.

Peters, H. C., Otto, T. J., Enders, J. T., Jin, W., Moed, B. R., & Zhang, Z. (2011). The protective role of the pericellular matrix in chondrocyte apoptosis. *Tissue Engineering Part A*, *17*(15-16), 2017–2024.

Pettenuzzo, S., Arduino, A., Belluzzi, E., Pozzuoli, A., Fontanella, C. G., Ruggieri, P., ... Berardo, A. (2023). Biomechanics of chondrocytes and chondrons in healthy conditions and osteoarthritis: A review of the mechanical characterisations at the microscale. *Biomedicines*, *11*(7), 1942.

Phillip, J. M., Aifuwa, I., Walston, J., & Wirtz, D. (2015). The mechanobiology of aging. *Annual review of biomedical engineering*, *17*, 113–141.

Pollard, T. D., Blanchoin, L., & Mullins, R. D. (2000). Molecular mechanisms controlling actin filament dynamics in nonmuscle cells. *Annual review of biophysics and biomolecular structure*, *29*(1), 545–576.

Poole, A. R., Kojima, T., Yasuda, T., Mwale, F., Kobayashi, M., & Laverty, S. (2001).

Composition and structure of articular cartilage: a template for tissue repair. *Clinical Orthopaedics and Related Research®*, *391*, S26–S33.

Poole, C. A., Matsuoka, A., & Schofield, J. R. (1991). Chondrons from articular cartilage. iii. morphologic changes in the cellular microenvironment of chondrons isolated from osteoarthritic cartilage. *Arthritis & Rheumatism: Official Journal of the American College of Rheumatology*, *34*(1), 22–35.

Pravincumar, P., Bader, D. L., & Knight, M. M. (2012). Viscoelastic cell mechanics and actin remodelling are dependent on the rate of applied pressure.

Rajagopal, V., Holmes, W. R., & Lee, P. V. S. (2018). Computational modeling of single-cell mechanics and cytoskeletal mechanobiology. *Wiley Interdisciplinary Reviews: Systems Biology and Medicine*, *10*(2), e1407.

Ren, J., Li, Y., Hu, S., Liu, Y., Tsao, S. W., Lau, D., ... Lam, R. H. (2020). Nondestructive quantification of single-cell nuclear and cytoplasmic mechanical properties based on large whole-cell deformation. *Lab on a Chip*, *20*(22), 4175–4185.

Rico, F., Roca-Cusachs, P., Gavara, N., Farré, R., Rotger, M., & Navajas, D. (2005). Probing mechanical properties of living cells by atomic force microscopy with blunted pyramidal cantilever tips. *Physical Review E*, *72*(2), 021914.

Roach, H., Aigner, T., & Kouri, J. (2004). Chondroptosis: a variant of apoptotic cell death in chondrocytes? *Apoptosis*, *9*, 265–277.

Rodriguez, M. L., McGarry, P. J., & Sniadecki, N. J. (2013). Review on cell mechanics: experimental and modeling approaches. *Applied Mechanics Reviews*, *65*(6), 060801.

Ronan, W., Deshpande, V. S., McMeeking, R. M., & McGarry, J. P. (2012). Numerical investigation of the active role of the actin cytoskeleton in the compression resistance of cells. *Journal of the Mechanical Behavior of Biomedical Materials*, *14*, 143–157.

Ruhlen, R., & Marberry, K. (2014). The chondrocyte primary cilium. *Osteoarthritis and cartilage*, *22*(8), 1071–1076.

Salucci, S., Falcieri, E., & Battistelli, M. (2022). Chondrocyte death involvement in osteoarthritis. *Cell and Tissue Research*, *389*(2), 159–170.

Sanchez, A. D., & Feldman, J. L. (2017). Microtubule-organizing centers: from the centrosome to non-centrosomal sites. *Current opinion in cell biology*, *44*, 93–101.

Sanchez-Lopez, E., Coras, R., Torres, A., Lane, N. E., & Guma, M. (2022). Synovial inflammation in osteoarthritis progression. *Nature Reviews Rheumatology*, *18*(5), 258–275.

Sato, M., Theret, D., Wheeler, L., Ohshima, N., & Nerem, R. (1990). Application of the micropipette technique to the measurement of cultured porcine aortic endothelial cell viscoelastic properties.

Savadipour, A., Palmer, D., Ely, E. V., Collins, K. H., Garcia-Castorena, J. M., Harissa, Z., ... others (2023). The role of piezo ion channels in the musculoskeletal system. *American Journal of Physiology-Cell Physiology*, *324*(3), C728–C740.

Schreiner, S. M., Koo, P. K., Zhao, Y., Mochrie, S. G., & King, M. C. (2015). The tethering of chromatin to the nuclear envelope supports nuclear mechanics. *Nature communications*, *6*(1), 7159.

Shieh, A. C., & Athanasiou, K. A. (2006). Biomechanics of single zonal chondrocytes. *Journal of biomechanics*, *39*(9), 1595–1602.

Shin, D., & Athanasiou, K. (1999). Cytoindentation for obtaining cell biomechanical properties. *Journal of Orthopaedic Research*, *17*(6), 880–890.

Singer, S. J., & Nicolson, G. L. (1972). The fluid mosaic model of the structure of cell membranes: Cell membranes are viewed as two-dimensional solutions of oriented globular proteins and lipids. *Science*, *175*(4023), 720–731.

Singh, P., Marcu, K. B., Goldring, M. B., & Otero, M. (2019). Phenotypic instability of chondrocytes in osteoarthritis: on a path to hypertrophy. *Annals of the New York Academy of Sciences*, *1442*(1), 17–34.

Sliogeryte, K., Thorpe, S. D., Wang, Z., Thompson, C. L., Gavara, N., & Knight, M. M. (2016). Differential effects of lifeact-gfp and actin-gfp on cell mechanics assessed using micropipette aspiration. *Journal of Biomechanics*, *49*(2), 310–317.

Smith, P. G., Deng, L., Fredberg, J. J., & Maksym, G. N. (2003). Mechanical strain increases cell stiffness through cytoskeletal filament reorganization. *American Journal of Physiology-Lung Cellular and Molecular Physiology*, *285*(2), L456–L463.

Song, Y., Soto, J., Chen, B., Yang, L., & Li, S. (2020). Cell engineering: biophysical regulation of the nucleus. *Biomaterials*, *234*, 119743.

Sophia Fox, A. J., Bedi, A., & Rodeo, S. A. (2009). The basic science of articular cartilage: structure, composition, and function. *Sports health*, *1*(6), 461–468.

Statham, P., Jones, E., Jennings, L. M., & Fermor, H. L. (2022). Reproducing the biomechanical environment of the chondrocyte for cartilage tissue engineering. *Tissue Engineering Part B: Reviews*, *28*(2), 405–420.

Steinecker-Frohnwieser, B., Lohberger, B., Toegel, S., Windhager, R., Glanz, V., Kratschmann, C., ... Weigl, L. (2023). Activation of the mechanosensitive ion channels piezo1 and trpv4 in primary human healthy and osteoarthritic chondrocytes exhibits ion channel crosstalk and modulates gene expression. *International Journal of Molecular Sciences*, *24*(9), 7868.

Stoecklein, N. H., & Klein, C. A. (2010). Genetic disparity between primary tumours, disseminated tumour cells, and manifest metastasis. *International journal of cancer*, *126*(3), 589–598.

Temple-Wong, M. M., Bae, W. C., Chen, M. Q., Bugbee, W. D., Amiel, D., Coutts, R. D., ... Sah, R. L. (2009). Biomechanical, structural, and biochemical indices of degenerative and osteoarthritic deterioration of adult human articular cartilage of the femoral condyle. *Osteoarthritis and Cartilage*, *17*(11), 1469–1476.

Theret, D. P., Levesque, M., Sato, M., Nerem, R., & Wheeler, L. (1988). The application of a homogeneous half-space model in the analysis of endothelial cell micropipette measurements.

Torzilli, P. A., & Allen, S. N. (2022). Effect of articular surface compression on cartilage extracellular matrix deformation. *Journal of Biomechanical Engineering*, *144*(9), 091007.

Trickey, W. R., Baaijens, F. P., Laursen, T. A., Alexopoulos, L. G., & Guilak, F. (2006). Determination of the poisson's ratio of the cell: recovery properties of chondrocytes after release from complete micropipette aspiration. *Journal of biomechanics*, *39*(1), 78–87.

Trickey, W. R., Lee, G. M., & Guilak, F. (2000). Viscoelastic properties of chondrocytes from normal and osteoarthritic human cartilage. *Journal of Orthopaedic Research*, *18*(6), 891–898.

Trickey, W. R., Vail, T. P., & Guilak, F. (2004). The role of the cytoskeleton in the viscoelastic properties of human articular chondrocytes. *Journal of Orthopaedic Research*, *22*(1), 131–139.

Van Oosterwyck, H., Geris, L., & Aznar, J. M. G. (2015). Cell mechanics and mechanobiology. *Biomechanics, edited by M. Doblare, and J. Merodio. Eolss Publishers/UNESCO*, 271–300.

Vargas-Pinto, R., Gong, H., Vahabikashi, A., & Johnson, M. (2013). The effect of the endothelial cell cortex on atomic force microscopy measurements. *Biophysical journal*, *105*(2), 300–309.

Vigliotti, A., Ronan, W., Baaijens, F., & Deshpande, V. (2016). A thermodynamically motivated model for stress-fiber reorganization. *Biomechanics and modeling in mechanobiology*, *15*, 761–789.

Vincent, K. R., Conrad, B. P., Fregly, B. J., & Vincent, H. K. (2012). The pathophysiology of osteoarthritis: a mechanical perspective on the knee joint. *PM&R*, *4*(5), S3–S9.

Vincent, T. L., McClurg, O., & Troeberg, L. (2022). The extracellular matrix of articular cartilage controls the bioavailability of pericellular matrix-bound growth factors to drive tissue homeostasis and repair. *International Journal of Molecular Sciences*, *23*(11), 6003.

Vogel, V., & Sheetz, M. (2006). Local force and geometry sensing regulate cell functions. *Nature reviews Molecular cell biology*, *7*(4), 265–275.

Wang, L., & Chen, W. (2019). Modelling cell origami via a tensegrity model of the cytoskeleton in adherent cells. *Applied Bionics and biomechanics*, *2019*.

Wang, L., Wang, L., Xu, L., Chen, W., et al. (2019). Finite element modelling of single cell based on atomic force microscope indentation method. *Computational and Mathematical Methods in Medicine*, *2019*.

Wang, N., Butler, J. P., & E., D. (1993). Mechanotransduction across the cell surface and through the cytoskeleton. *Science*, *260*(5111), 1124-1127. Retrieved from `https://www.science.org/doi/abs/10.1126/science.7684161` doi: 10.1126/science.7684161

Williantarra, I., Leung, S., Choi, Y. S., Chhana, A., & McGlashan, S. R. (2022). Chondrocyte-specific response to stiffness-mediated primary cilia formation and

centriole positioning. *American Journal of Physiology-Cell Physiology*, *323*(1), C236–C247.

Wilusz, R. E., & Guilak, F. (2014). High resistance of the mechanical properties of the chondrocyte pericellular matrix to proteoglycan digestion by chondroitinase, aggrecanase, or hyaluronidase. *Journal of the mechanical behavior of biomedical materials*, *38*, 183–197.

Wilusz, R. E., Zauscher, S., & Guilak, F. (2013). Micromechanical mapping of early osteoarthritic changes in the pericellular matrix of human articular cartilage. *Osteoarthritis and cartilage*, *21*(12), 1895–1903.

Wozniak, M. J., Kawazoe, N., Tateishi, T., & Chen, G. (2009). Monitoring of mechanical properties of serially passaged bovine articular chondrocytes by atomic force microscopy. *Micron*, *40*(8), 870–875.

Xiao, Z.-f., Su, G.-y., Hou, Y., Chen, S.-d., & Lin, D.-k. (2018). Cartilage degradation in osteoarthritis: A process of osteochondral remodeling resembles the endochondral ossification in growth plate? *Medical Hypotheses*, *121*, 183–187.

Xiaowei Zhuang. (2012). *Fluorecent image of the cell actin network.* Retrieved from `https://images.nigms.nih.gov/pages/DetailPage.aspx?imageid2=3749` ([Credit: Xiaowei Zhuang, HHMI, Harvard University, and Nature Publishing Group. Online; accessed 1-3-23])

Youn, I., Choi, J., Cao, L., Setton, L., & Guilak, F. (2006). Zonal variations in the three-dimensional morphology of the chondron measured in situ using confocal microscopy. *Osteoarthritis and cartilage*, *14*(9), 889–897.

Young, C., & Kobayashi, T. (2023). Limited roles of piezo mechanosensing channels in articular cartilage development and osteoarthritis progression. *Osteoarthritis and Cartilage*, *31*(6), 775–779.

Yuan, X., & Yang, S. (2016). Primary cilia and intraflagellar transport proteins in bone and cartilage. *Journal of dental research*, *95*(12), 1341–1349.

Zhang, G., Long, M., Wu, Z.-Z., & Yu, W.-Q. (2002). Mechanical properties of hepatocellular carcinoma cells. *World journal of gastroenterology*, *8*(2), 243.

Zhang, M., Meng, N., Wang, X., Chen, W., & Zhang, Q. (2022). Trpv4 and piezo channels mediate the mechanosensing of chondrocytes to the biomechanical microenvironment. *Membranes*, *12*(2), 237.

Zhou, E., Lim, C., & Quek, S. (2005). Finite element simulation of the micropipette aspiration of a living cell undergoing large viscoelastic deformation. *Mechanics of Advanced Materials and Structures*, *12*(6), 501–512.

Zhu, C., Bao, G., & Wang, N. (2000). Cell mechanics: mechanical response, cell adhesion, and molecular deformation. *Annual review of biomedical engineering*, *2*(1), 189–226.

Zhuang, H., Ren, X., Zhang, Y., Jiang, F., & Zhou, P. (2023). Trimethylamine-n-oxide sensitizes chondrocytes to mechanical loading through the upregulation of piezo1. *Food and Chemical Toxicology*, *175*, 113726.